NASA/TP—2013–217488

Summary of the 2012 Inductive Pulsed Plasma Thruster Development and Testing Program

K.A. Polzin, A.K. Martin, R.H. Eskridge, A.C. Kimberlin, B.M. Addona, A.P. Devineni, and N.R. Dugal-Whitehead
Marshall Space Flight Center, Huntsville, Alabama

A.K. Hallock
Yetispace, Inc., Huntsville, Alabama

August 2013

The NASA STI Program…in Profile

Since its founding, NASA has been dedicated to the advancement of aeronautics and space science. The NASA Scientific and Technical Information (STI) Program Office plays a key part in helping NASA maintain this important role.

The NASA STI Program Office is operated by Langley Research Center, the lead center for NASA's scientific and technical information. The NASA STI Program Office provides access to the NASA STI Database, the largest collection of aeronautical and space science STI in the world. The Program Office is also NASA's institutional mechanism for disseminating the results of its research and development activities. These results are published by NASA in the NASA STI Report Series, which includes the following report types:

- TECHNICAL PUBLICATION. Reports of completed research or a major significant phase of research that present the results of NASA programs and include extensive data or theoretical analysis. Includes compilations of significant scientific and technical data and information deemed to be of continuing reference value. NASA's counterpart of peer-reviewed formal professional papers but has less stringent limitations on manuscript length and extent of graphic presentations.

- TECHNICAL MEMORANDUM. Scientific and technical findings that are preliminary or of specialized interest, e.g., quick release reports, working papers, and bibliographies that contain minimal annotation. Does not contain extensive analysis.

- CONTRACTOR REPORT. Scientific and technical findings by NASA-sponsored contractors and grantees.

- CONFERENCE PUBLICATION. Collected papers from scientific and technical conferences, symposia, seminars, or other meetings sponsored or cosponsored by NASA.

- SPECIAL PUBLICATION. Scientific, technical, or historical information from NASA programs, projects, and mission, often concerned with subjects having substantial public interest.

- TECHNICAL TRANSLATION. English-language translations of foreign scientific and technical material pertinent to NASA's mission.

Specialized services that complement the STI Program Office's diverse offerings include creating custom thesauri, building customized databases, organizing and publishing research results…even providing videos.

For more information about the NASA STI Program Office, see the following:

- Access the NASA STI program home page at <http://www.sti.nasa.gov>

- E-mail your question via the Internet to <help@sti.nasa.gov>

- Fax your question to the NASA STI Help Desk at 443–757–5803

- Phone the NASA STI Help Desk at 443–757–5802

- Write to:
  NASA STI Help Desk
  NASA Center for AeroSpace Information
  7115 Standard Drive
  Hanover, MD 21076–1320

NASA/TP—2013–217488

Summary of the 2012 Inductive Pulsed Plasma Thruster Development and Testing Program

K.A. Polzin, A.K. Martin, R.H. Eskridge, A.C. Kimberlin, B.M. Addona,
A.P. Devineni, and N.R. Dugal-Whitehead
Marshall Space Flight Center, Huntsville, Alabama

A.K. Hallock
Yetispace, Inc., Huntsville, Alabama

National Aeronautics and
Space Administration

Marshall Space Flight Center • Huntsville, Alabama 35812

August 2013

Acknowledgments

This work benefited from the support and contributions of many individuals. We would like to acknowledge continued Marshall Space Flight Center (MSFC) Propulsion Systems Department management support of this work from Jim Martin, Patrick McRight, Tom Williams, Mary Beth Koelbl, and Tom Brown. We would additionally like to thank Jim Richard and Karen Cunningham for supporting the effort reported upon in this Technical Publication.

This work benefited from many technical discussions with J. Boise Pearson and Michael LaPointe of MSFC and Gregory Emsellem of The Elwing Company. We thank Andy Finchum for the use of a Shimadzu camera to obtain high-speed images. We also thank William Emrich of MSFC and John Gerling of Gerling Applied Engineering, Inc., for providing valuable support of our efforts to use a microwave-driven plasma in our experiment. We further wish to thank Jim Browning, Don Plumlee, Peter Bumbarger, and Mallory Yates of Boise State University for bringing their inductively coupled plasma sources to MSFC for joint testing.

This research was enabled by the continuing efforts and contributions of the MSFC technical support staff at the Propulsion Research and Development Laboratory: Tommy Reid, Doug Galloway, Keith Chavers, David Wilkie, Roger Harper, Stan McDonald, and Mark Black. We would be remiss if we did not acknowledge and thank the NASA interns working at MSFC that contributed to bringing this work to fruition: Kevin Perdue, Alexandra Toftul, Andrea Wong, Kevin Bonds, and Mark Becnel.

This work was funded through the In-Space Propulsion Project of the Game-Changing Development (GCD) Program of NASA's Office of the Chief Technologist. The GCD principle investigator was Chuck Taylor (NASA Langley Research Center) and the project manager was Tim Smith (NASA Glenn Research Center).

TRADEMARKS

Available from:

NASA Center for AeroSpace Information
7115 Standard Drive
Hanover, MD 21076–1320
443–757–5802

This report is also available in electronic form at
<https://www2.sti.nasa.gov/login/wt/>

TABLE OF CONTENTS

TABLE OF CONTENTS (Continued)

LIST OF FIGURES

LIST OF FIGURES (Continued)

LIST OF FIGURES (Continued)

LIST OF FIGURES (Continued)

LIST OF FIGURES (Continued)

LIST OF TABLES

LIST OF ACRONYMS, ABBREVIATIONS, AND SYMBOLS

CCS	capacitor charging supply/supplies
CRES	corrosion resistant steel
CTP	conical theta-pinch
ECR	electron-cyclotron resonance
E-stop	emergency stop
FARAD	Faraday Accelerator with Radio-Frequency Assisted Discharge
FIB	fiber optic interface board
FRD	fast recovery diode
HV	High-Voltage
IPPT	inductive pulsed plasma thruster
LGDT	linear gap displacement transducer
LRC	inductive-resistive-capacitive
M	Mach number
MOSFET	metal-oxide semiconductor field-effect transistor
MSFC	Marshall Space Flight Center
N_2	nitrogen
PGV	pulsed gas valve
PIT	pulsed inductive thruster
POF	plastic optical fiber
PPU	power processing unit

PSPICE	Personal Simulation Program with Integrated Circuit Emphasis
RTV	room temperature vulcanizing
SPICE	Simulation Program with Integrated Circuit Emphasis
TP	Technical Publication
VAHPER	Variable Amplitude Hanging Pendulum with Extended Range

NOMENCLATURE

a	sound speed of gas
b	curve fit parameter
C	bank capacitance
C_{load}	capacitive load
F_i	force in the i-th direction
I	current
I_1	current in the driving circuit
I_2	current flowing in the plasma
I_{bit}	measured impulse bit
I_{sp}	specific impulse
I_{tot}	total current
i	dimensional index
k	Boltzmann's constant
k_0	coupling coefficient
L	inductance
L_0	initial inductance
L_C	acceleration coil inductance
L_{eff}	effective inductance
L_{iso}	series isolation inductance
L_{tot}	total inductance

NOMENCLATURE (Continued)

L^*	inductance ratio
L'	inductance per unit length
L_r'	radial inductance per unit length
L_z'	axial inductance per unit length
$\dot{L}$	dynamic impedance
$\dot{L}_r$	dynamic impedance, radial direction
$\dot{L}_z$	dynamic impedance, axial direction
l	cone axial length
l_{coil}	length of the coil
M	mutual inductance
m_{Ar}	mass of an argon atom
m_{bit}	mass bit; total propellant mass
m_i	mass of an ion
$\dot{m}$	mass flow rate
N	fit parameter
n	number density
P_1	pressure upstream of the shock
P_2	gas-dynamic pressure force
P_{jet}	jet power
p	number of parameters; pressure rise per pulse
R_e	external resistance

NOMENCLATURE (Continued)

R_{iso}	series isolation resistance
R_p	plasma resistance
$R_{prot\ 1}$	power supply output power resistors of 10 Ω
$R_{prot\ 2}$	power supply output power resistors of 1 Ω
r	radius
r_{coil}	minor radius of the coil
r_{in}	inner radius
r_{out}	outer radius
$\overline{r}$	average radial position
$\overline{r_{coil}}$	average radial position of the coil
T	temperature
T_1	temperature of gas upstream of the shock
t	time
t_{char}	characteristic length of time
u	shock velocity
V	chamber volume
V_0	initial charge voltage
V_{bank}	scaled bank voltage
$V_{FO\ Rx}$	voltage at the receiver/demodulator
$V_{HV,inhibit}$	power supply high-voltage inhibit voltage
v	velocity

NOMENCLATURE (Continued)

v_r	radial velocity
v_z	axial current sheet velocity
W_B	total magnetic energy
z	axial displacement
z_0	axial decoupling distance
α	dynamic impedance ratio
Γ	gas throughput
γ	ratio of specific heat
η	efficiency
η_t	thrust efficiency
θ	half-cone angle
λ	magnitude of the gas-dynamic pressure in opposing radially inward current sheet motion
ν	statistical weighting factor
Ξ	measure of the growth rate of the gas-dynamic pressure as the current sheet shock front undergoes radial acceleration
ϕ	dynamic impedance ratio for radial current sheet motion
χ	curve-fitting statistical term
ψ_1	critical resistance ratio
ψ_2	critical resistance ratio

TECHNICAL PUBLICATION

SUMMARY OF THE 2012 INDUCTIVE PULSED PLASMA THRUSTER DEVELOPMENT AND TESTING PROGRAM

1. INTRODUCTION

In fiscal year 2012, Marshall Space Flight Center (MSFC) conducted a program to incrementally develop and advance technologies that would be needed to eventually employ an inductive pulsed plasma thruster (IPPT) for in-space propulsion. This work was conducted under NASA's Office of the Chief Technologist, within the Game Changing Development Program, as part of the In-Space Propulsion Project.

The IPPT is an electrodeless space propulsion device where a capacitor is charged to an initial voltage and then discharged, producing a high-current pulse through a coil. The field produced by this pulse ionizes propellant, inductively driving current in a plasma located near the face of the coil. Once the plasma is formed, it can be accelerated and expelled at a high exhaust velocity by the electromagnetic Lorentz body force arising from the interaction of the induced plasma current and the magnetic field produced by the current in the coil.

Thrusters of this type possess many demonstrated and potential benefits that make them worthy of continued investigation. The electrodeless nature of these thrusters eliminates the lifetime and contamination issues associated with electrode erosion in conventional electric thrusters. Also, a wider variety of propellants are accessible when compatibility with metallic electrodes are no longer an issue. IPPTs have been successfully operated using propellants like ammonia, hydrazine, and carbon dioxide, and there is no fundamental reason why they would not operate on other in situ propellants like water. It is well known that pulsed accelerators can maintain constant specific impulse (I_{sp}) and thrust efficiency (η_t) over a wide range of input power levels by adjusting the pulse rate to hold the discharge energy per pulse constant. It has also been demonstrated that an IPPT can operate in a regime where η_t is relatively constant over a wide range of I_{sp} values (3,000 to 8,000 s). Finally, thrusters in this class have operated in single-pulse mode at high energy per pulse, and by increasing the pulse rate, they offer the potential to process very high levels of power using a single thruster.

This Technical Publication (TP) describes IPPT research conducted at MSFC during 2012. The tasks undertaken were performed to begin the process of addressing several critical IPPT development issues. Specifically, the following tasks were performed and are documented in this TP:

- Fabrication and performance measurements on a conical theta-pinch (CTP) device to address potential techniques to improve propellant utilization over flat-plate planar coil designs.

- Assembly of a capacitor charging system capable of supporting fast charging operations to permit repetition-rate operation of pulsed thrusters.

- Fabrication of a small-scale, flat-plate planar coil IPPT as a testbed for evaluation of lower energy, off-the-shelf, solid-state switch technologies.

- Design, fabrication, and initial testing of a prototype long-lifetime pulsed gas valve (PGV) like that needed to support a mission that might employ an IPPT system for propulsion.

- Initial subscale research and development of a high-voltage IPPT power processing unit (PPU) that could potentially be integrated into a thruster system and provide for repetitive capacitor bank recharging.

2. CONICAL THETA-PINCH THRUSTER RESEARCH

There has been significant previous research on IPPTs designed around a planar coil (flat-plate) geometry.[1] The most notable of these was the pulsed inductive thruster (PIT).[2] During the early investigations on the PIT geometry,[3] testing with smaller scale planar coil thrusters revealed differences in propellant utilization efficiency between the cases where propellant was injected using a pulsed gas system and where the coil was situated within an ambient backfill environment with no pulsed gas injection employed. In these experiments, the latter cases outperformed the former. It was believed, based upon current density measurements, that the nonuniform propellant distribution in the pulsed gas injection cases resulted in poorer overall coupling between the coil and the plasma. In more recent low-energy (<100 J/pulse) experiments, an ambient backfill environment was employed and a separate preionization source was used to generate a seed-plasma before the application of the current pulse through the coil. In these tests, a plasma sheet was only produced by the current pulse through the coil when a sufficiently strong magnetic field was applied to divert the preionized plasma from the natural diffusion path along the centerline to a path over the coil face.[4,5]

An approach was proposed to alter the coil geometry such that it more closely aligns with the natural path followed by the injected propellant, potentially making the propellant distribution uniform and more easily preionizable. This strategy was the motivation for the experimental work on the CTP IPPT geometry detailed in the present section of this TP. Modeling of the acceleration process in CTP geometry thrusters was performed to gain additional insights into the scaling of performance in these types of thrusters. Results of this modeling effort are discussed at the end of this section, where they are reconciled with the experimental measurements.

2.1 Conical Theta-Pinch Description

The CTP thruster consists of a thruster coil, capacitor bank and switch, gas injection system, and preionization system. Each of these is discussed in turn in this section, with particular attention paid to documenting not only the final design iteration, but all methods attempted and the issues encountered during the development effort.

2.1.1 Coils

Three CTP inductive coils were constructed for performance testing (see example with labeled geometry in fig. 1). Two of the coils have length (l_{coil}) of 10 cm (4 in) and a minor radius (r_{coil}) of 4 cm (1.6 in). The half-cone angles (θ) for these coils are 20° and 38°. The third coil has l_{coil} of 5 cm (2 in), r_{coil} of 4 cm (1.6 in), and θ of 60°. In all three cases, the inductance of the coil is 240 (±20) nH as measured using an Agilent 4285A precision inductance-capacitance-resistance meter. The 38° coil in figure 1 is shown prior to being encased in room temperature vulcanizing silicone (RTV), which serves to insulate the coil surface from the ionized propellant. This insulating layer was covered with aerosol boron nitride spray to prevent ablation of the RTV surface.

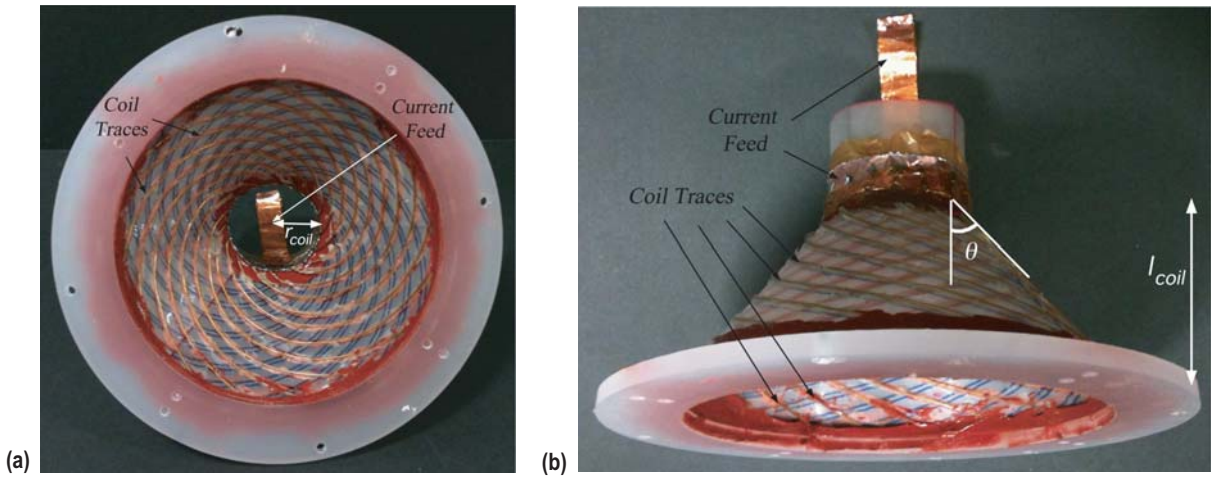

Figure 1. 38° CTP inductive coil showing (a) front view along the axis and (b) top view.

The conducting traces comprising each coil were assembled in two layers. In all, the coil is formed from 16 separate Kapton®-insulated 22-gauge wires. Each wire completes a half-turn spiral going from the back end of the cone (smaller radius position) to the front and another half-turn spiral in the same azimuthal direction returning to the back end of the cone on the other side of the insulating sheet. The insulating sheet is comprised of two layers of 0.25-mm- (0.01-in-) thick Mylar® that provides the physical structure for the cone. When superimposed, the current passing through the windings creates a nearly azimuthal net current in the coil. The windings are electrically connected in parallel to common current feed and return locations at the back of the cone. Each common connection consists of 2.5-cm- (1-in-) wide, 12-gauge-equivalent, flat copper speaker wire with an axial gap at one azimuthal location to interrupt any induced azimuthal eddy currents.

2.1.2 Capacitor Bank and Switch

The capacitor bank consisted of four 10 μF capacitors rated to 7.5 kV. These capacitors are vacuum-compatible, oil-filled metal cans with a series inductance of not more than 20 nH. The terminations are side-by-side terminals of No. 8 threaded rod, insulated from the capacitor body using ceramic standoffs. The capacitors were connected in parallel, decreasing the inductance they presented to the driving circuit and increasing the total capacitance to 40 μF. Stripline constructed from 2.5-cm- (1-in-) wide, 12-gauge-equivalent, flat copper speaker wire was used to connect the capacitor to a high-current switch and then to connect from the switch to the thruster.

Two different switching mechanisms were employed. In configuration 1, a simple mechanical switch (shown in fig. 2(a)) is used to discharge the capacitor bank. The switch was designed to minimize inductance, adding less than 50 nH to the driving circuit. In configuration 1, the switch and capacitor bank were located external to the vacuum vessel, and stripline was used to feed the current pulse to the thruster. The mechanical switch was actuated manually.

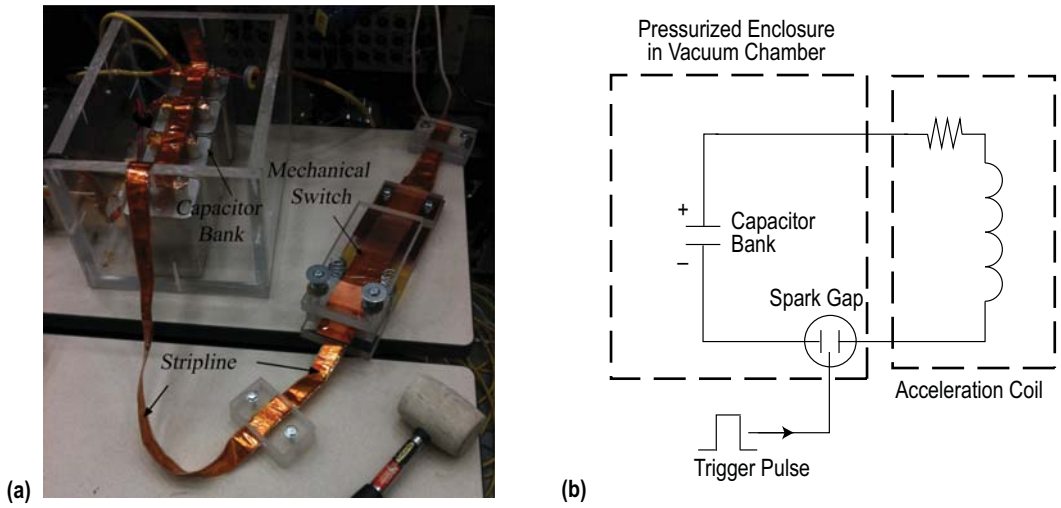

Figure 2. Photograph of (a) the configuration 1 capacitor bank and mechanical switch and (b) electrical circuit schematic for the configuration 2 thruster.

In configuration 2 (shown schematically in fig. 2(b)), the energy in the capacitor bank was discharged through a Perkin Elmer-triggered spark gap switch. The capacitor bank and switch were placed inside an atmospherically pressurized enclosure that was mounted on the thrust stand directly behind the thruster. This was done to minimize the stray inductance that was incurred in configuration 1 by the mechanical switch and the stripline used to connect the externally mounted hardware to the thruster inside the vacuum vessel.

2.1.3 Gas Injection

Gas flow was controlled using an MKS metal-sealed type 1479A flow controller with a maximum flow rate of 10,000 sccm. Research-grade argon and xenon propellants were used for all work reported in this TP. A steady-state gas flow was employed in the CTP since the thruster was not designed to include a fast pulse valve. For configuration 1 testing, propellant was injected at a single point through a conducting tube located along the centerline of the thruster at the upstream end of the coil. Once injected, the gas diffuses axially downstream into the vacuum vessel, leading to a lower pressure at the downstream end of the coil as compared to the upstream end. In configuration 2 testing, four insulating tubes were connected to a downstream manifold and aligned on the surface of the cone azimuthally equidistant from each other. Several holes were cut into the tubes at different axial locations to permit gas to flow into the thruster in the azimuthal direction. The change in propellant injection in configuration 2 was motivated by the desire to inject the gas as close to the coil face as possible, instead of relying on natural diffusion of the propellant from a single upstream point located on the axis to accomplish this goal.

2.1.4 Preionization Techniques

In some inductive accelerators like the PIT, the capacitor bank must first be charged to a high voltage and then discharged very rapidly through the inductive coil to ionize the propellant.[2,6]

Preionization can be employed in an IPPT to increase the conductivity of the propellant, making it easier for the current pulse through the coil to electromagnetically couple with and completely break down the gas and induce a current sheet.[7] While it adds an additional subsystem to the thruster, an advantage of this technique is that the requirement of high voltage and the commensurate requirement of a high-current rise rate in the coil can be partly ameliorated by preionization, making it possible to use present off-the-shelf, state-of-the-art switches and capacitors for the main discharge pulse circuit. The use of preionization in conjunction with pulsed inductive plasma systems appears often in the literature, with applications ranging from spacecraft propulsion to fusion plasmas. Preionization has been successfully employed in these applications by striking a glow discharge between two electrodes,[8–10] sending a separate lower energy pulse through the same inductive coil used for plasma acceleration,[11–13] and using radio frequency waves to generate plasma.[4,5,14]

The system ultimately employed for preionizing the gas in the CTP was a glow discharge-based system. The discharge was produced between two electrodes that were placed at the upstream (narrow radius) and downstream (larger radius) ends of the coil, as shown in figure 3. The downstream electrodes were composed of copper and were segmented so as to avoid presenting a continuous azimuthal conductive path that could drain energy from the discharge through the coil by permitting the flow of azimuthal-induced eddy currents. The upstream electrode was a 6-in-long section of 0.635-mm (0.25-in) stainless steel tubing located on the thruster centerline. As mentioned in the previous section, propellant was injected through this tube into the thruster during configuration 1 testing. Prior to the initiation of a high-current pulse, the glow discharge was created using a fiber optic signal to enable a Glassman FJ-series 120 W high-voltage, low-current DC power supply set to 3–4 kV. An unfiltered 16 s exposure of the preionizer operating on 150 mg/s of argon is shown in figure 4.

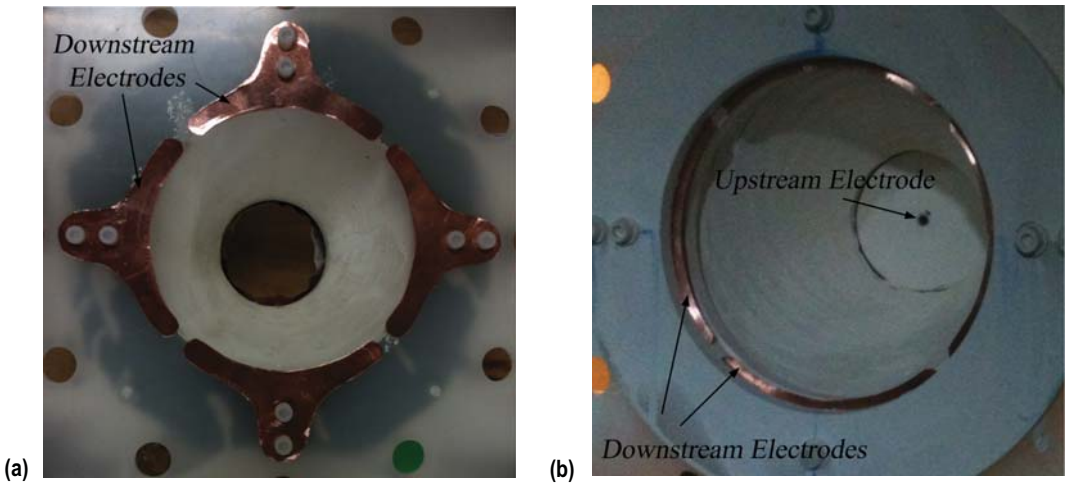

Figure 3. Photograph of (a) the downstream electrodes in the CTP thruster and (b) both electrodes installed in the CTP with the downstream electrode cover attached.

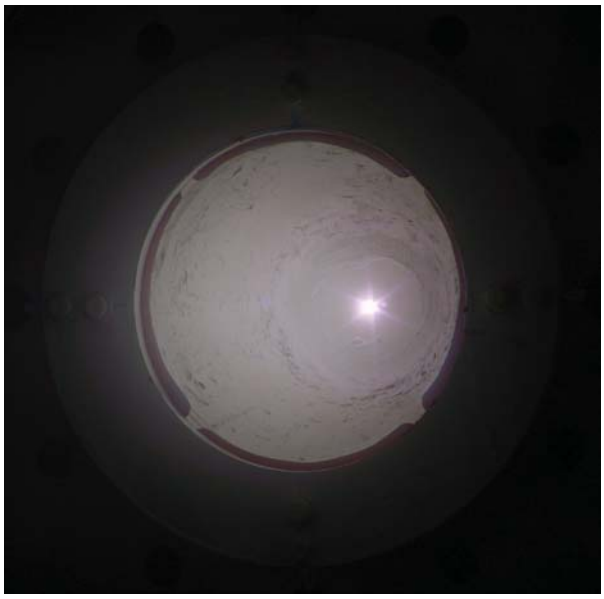

Figure 4. Preionized plasma produced in the CTP thruster by a glow discharge.

It should be noted here that in configuration 1, preionization was required to permit the formation of an inductively coupled plasma during the primary current pulse. Without the use of preionization, no plasma would form and no measureable impulse bit would be observed when the capacitor bank was discharged. In configuration 2, the preionization subsystem did not appear to be required for the thruster to operate, and there was no apparent effect (within the error bars) on the measured impulse bit when testing was conducted without preionization.

An electrodeless preionization technique explored during the course of testing involved the use of 2.45 GHz microwaves[15,16] at power levels up to almost 3 kW of forward power (with about 1 kW of reflected power in the best-tuned configuration). For that testing, neodymium disk magnets were installed in the thruster to produce a magnetic field at the coil face that would be approximately 875 G, which is commensurate with the field value required to produce an electron-cyclotron resonance (ECR) discharge. Magnetic field modeling results showing the field strength in the thruster are presented in figure 5. A photograph of the resulting microwave-driven, continuous-wave ECR discharge is presented in figure 6. This technique proved difficult to use for two reasons. First, to permit thrust measurements on a hanging pendulum thrust stand, the waves had to be launched into the thruster from the back end by an antenna not in contact with any part of the thruster. Second, the thruster itself is not a resonant cavity for microwaves, so in most cases, the microwave energy beamed into the thruster from the antenna would pass right through the thruster channel without producing a discharge. Finally, the microwaves interacted with metal in the thruster, which presents many discontinuities to the field, causing arcs between current-carrying coils and damaging the insulation in sections of the thruster. For the purposes of expediency, this concept was abandoned during the project in favor of the simpler glow discharge method.

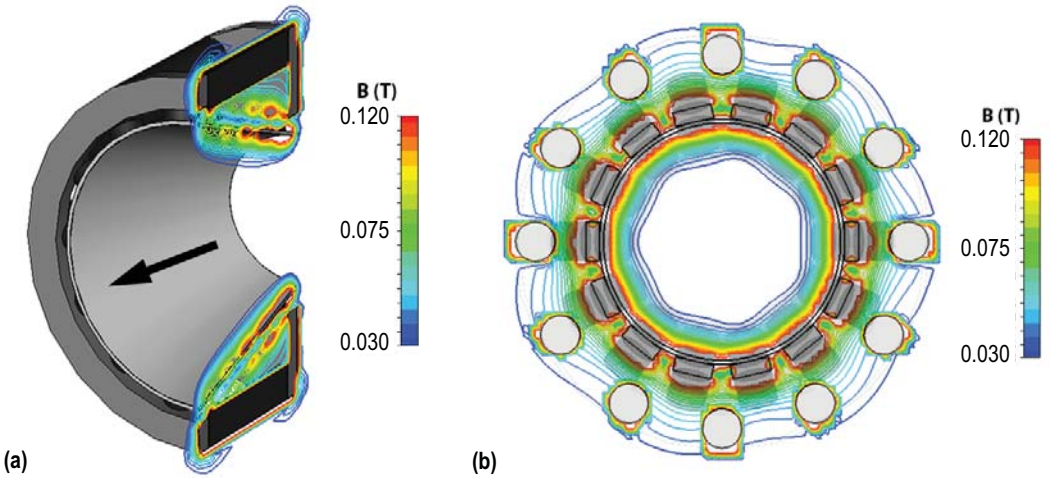

Figure 5. Finite element magnetic field modeling results for the CTP thruster, with the ECR zones shown in yellow, green, and light blue. The thruster axis is represented by the black arrow and the structure is shown in black and white: (a) Perspective view and (b) front-looking aft view along thruster axis.

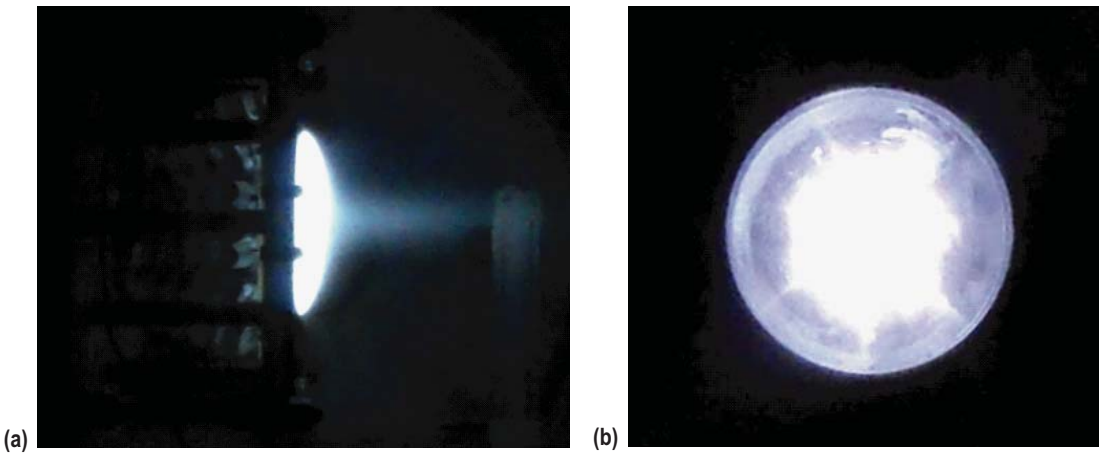

Figure 6. Microwave-driven ECR discharge produced in the CTP: (a) Side view and (b) front-looking aft view along thruster axis.

While never fully integrated into a thruster, a second electrodeless preionization concept explored was the miniature inductively coupled plasma source.[17] This source operated in the 500 to 1,000 MHz range at input power levels from a few watts up to 50 W. The low power requirements and capability to integrate the inductive antenna into a future design make this source a promising candidate for future thruster iterations.

2.2 Experimental Facility and Diagnostics

2.2.1 Vacuum Facility

The vacuum facility is a 7.6-m- (25-ft-) long, 2.7-m- (9-ft-) diameter, stainless steel cylindrical vacuum chamber. The chamber can be evacuated to a base pressure (gauge calibrated on nitrogen (N_2)) of 7.6×10^{-5} Pa (5.7×10^{-7} torr), maintained by either two 32-in, cold-trapped diffusion pumps with a combined unobstructed pumping speed of 65,000 L/s, or two 2,400 L/s turbopumps used in combination with two 9,500 L/s flange-mounted GHe cryopumps (all pumping speeds on N_2). The diffusion pump cold traps are cooled using a recirculating Polycold® chiller.

2.2.2 Thrust Stand

The hanging pendulum-type Variable Amplitude Hanging Pendulum with Extended Range (VAHPER) thrust stand, shown in figure 7, is used to perform thrust measurements in the TP. In general, as a thruster is operating, the VAHPER stand directly measures thrust by monitoring the level of displacement of the pendulum arm from an equilibrium point as a function of time. Displacement of the thrust stand arm is measured using a noncontact, light-based linear gap displacement transducer (LGDT). The thrust is obtained from the displacement data using a calibration of the thrust stand arm displacement acquired as a function of the application of known forces. The stand is capable of supporting thrusters with masses up to 125 kg that produce between 100 μN and 1 N of steady-state thrust. More information about the thrust stand in its steady-state configuration can be found in reference 18. An image of the thruster on the thrust stand is shown in figure 8.

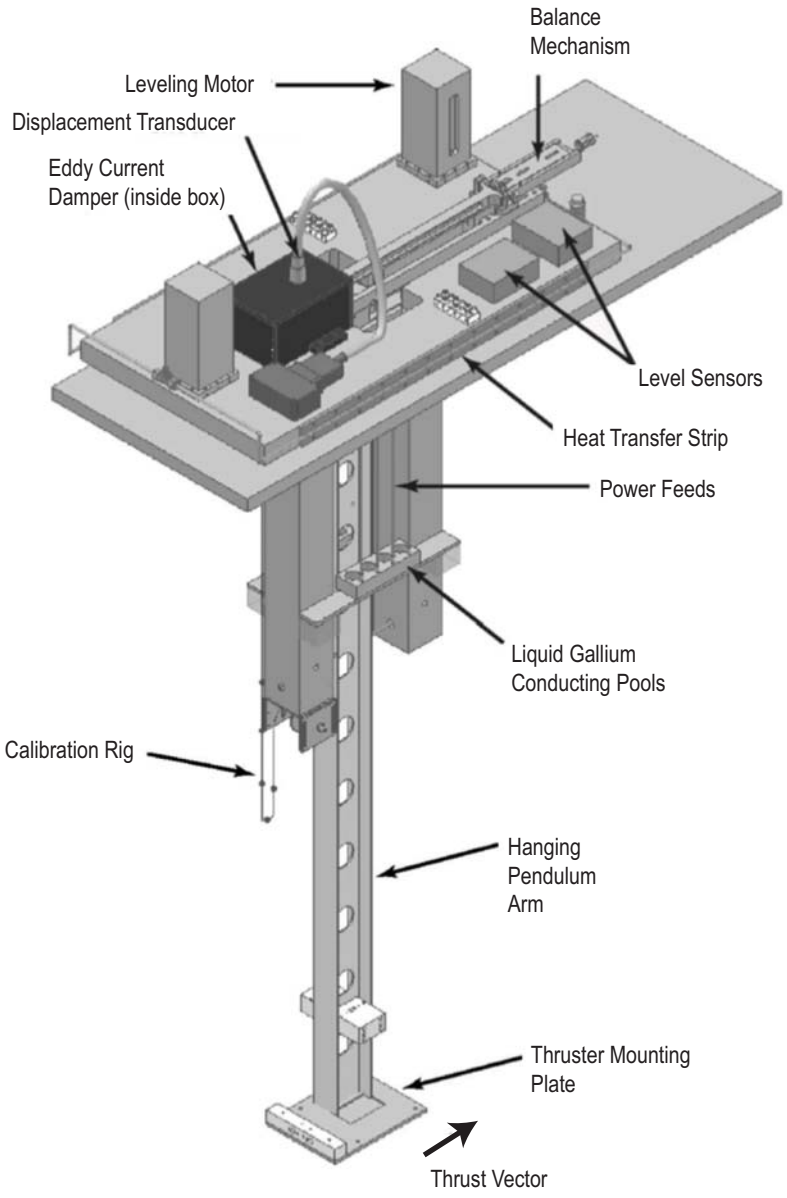

Figure 7. VAHPER thrust stand schematic.

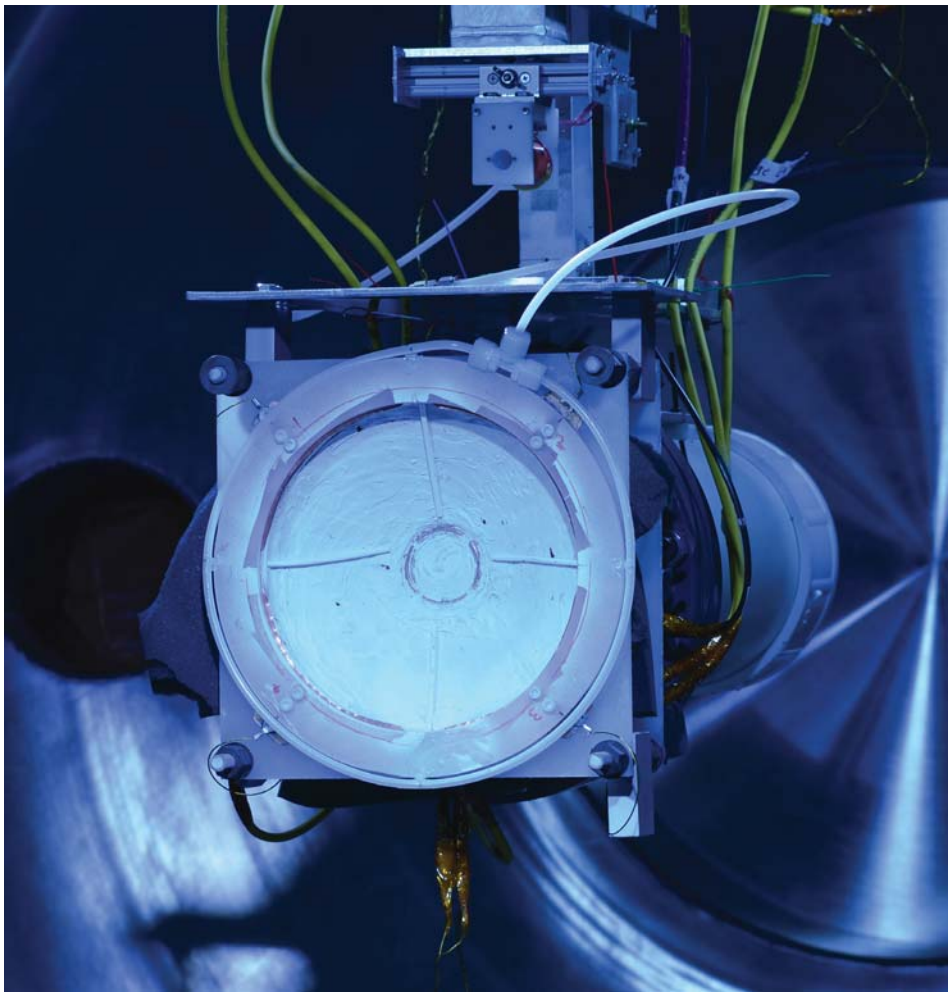

Figure 8. 60° IPPT mounted on the thrust stand.

The stand was recently modified through the addition of a pulsed thruster calibration system,[19] shown in figure 9. This system applies an impulsive (on the timescale of thrust stand motion) force to the thrust stand arm by passing a current pulse through a solenoid mounted to a fixed point located external to the moving thrust stand arm. The magnetic field produced by the current in the solenoid acts against a permanent rare earth magnet on the thrust stand arm, repelling it. This force is transmitted to the thrust stand arm through a piezoelectric force transducer, providing a direct measurement of the applied force as a function of time, which can be integrated with respect to time to provide a measure of the impulse bit. Under pulsed testing, the stand executes a damped sinusoidal oscillation, and through calibration, all the coefficients associated with that motion can be experimentally determined, permitting the determination of the unknown thruster-produced impulse bit through the measure of the thrust stand arm displacement history. This calibration setup can also be used in the case where the thruster is to be pulsed multiple times where the pulse period is less than the oscillatory period of the pendulum arm. Pulsing the calibration apparatus multiple times on timescales much shorter than the thrust stand oscillatory period permits the mimicking of the effect a repetitively pulsed thruster has on the thrust stand, allowing the determination of the average displacement as a function of average thrust. The force transducer measurements are captured using

a Lecroy 8-bit, 1 GHz LC564DL oscilloscope, while the LGDT measurements are recorded using a Lecroy 8-bit, 500 MHz LC554DL oscilloscope.

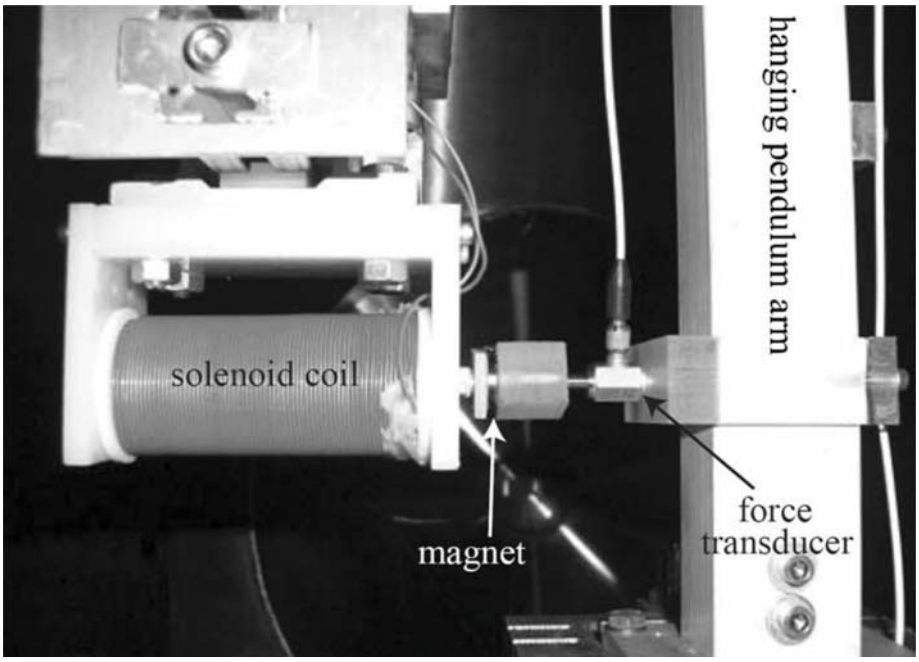

Figure 9. Thrust stand pulsed calibration apparatus.

2.2.3 Terminal Measurements

The discharge current in the CTP thruster was measured using an air core Rogowski coil. A current feed from the capacitor bank was passed through the coil to yield the measured signal. The coil output was calibrated against a Pearson current transducer.

The voltage on the capacitor bank was measured using a Tektronix® P6015A frequency-compensated, 1,000:1 high-voltage probe. Differential voltage measurements between the two common stripline connections at the upstream end of the thruster were performed using a Tektronix P5205 frequency-compensated, high-voltage differential probe. The latter measurements, specifically aimed at measuring the fraction of the voltage that appeared across the coil terminals, were performed at atmospheric pressure and for lower capacitor charge voltages relative to actual CTP thruster operating conditions. All high-speed data are captured using a Lecroy 8-bit, 1 GHz LC564DL oscilloscope.

2.2.4 Imaging Tools

Time-integrated photographs of the CTP thruster were captured using a Kodak Z812 IS SLR digital camera with an ISO setting of 64, a focal ratio of 8, and an exposure time of 1 s. The images are acquired unfiltered, and all image-altering functions of the camera, including white balance and automatic focusing, were disabled. The camera was pointed at the thruster, offset approximately 10° from the thruster centerline, and located 6 m (20 ft) downstream from the thruster exit plane.

Time-resolved imaging of the discharge was performed using a Shimadzu HPV-2 model CCD camera. The camera is capable of recording up to 100 frames in a single pulse with an adjustable frame rate as fast as 1 Mfps. The exposure times are adjustable down to an eighth of the recording interval.

2.3 Presentation of Data and Discussion

The following is a presentation of data obtained during single-pulse operation of the CTP thruster. As the CTP thruster was not equipped with a PGV, all images and performance data presented in this section are for operation with a steady gas flow. Additional data obtained while operating in a repetition-rate mode are presented in section 3.4 of this TP.

2.3.1 Voltage and Current Measurements

Terminal voltage and current measurements for the CTP thruster are presented in figure 10. Configuration 1 capacitor bank voltage waveforms for charge voltages of approximately 3, 4, and 5 kV are given in figure 10(a), with the corresponding coil currents found in figure 10(b). Similar data for configuration 2, obtained for a capacitor bank voltage of 5 kV, are found in figures 10(c) and (d).

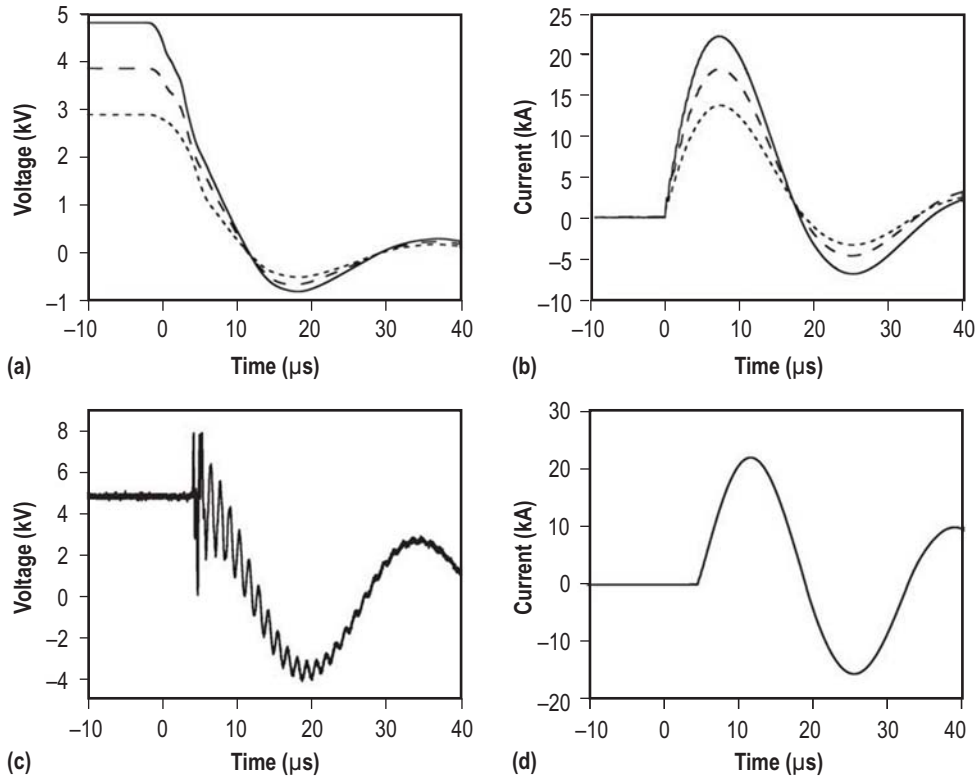

Figure 10. Measured configuration 1 (a) capacitor bank voltage and (b) current for charge voltages of approximately 3, 4, and 5 kV, and configuration 2 (c) capacitor bank voltage and (d) current for charge voltage of 5 kV.

Measurements of the capacitor bank voltage and voltage across the inductive coil (coil terminal voltage) are presented for configurations 1 and 2 in figures 11(a) and (b), respectively. These data show that the closer proximity of the capacitor bank and the coil in configuration 2 significantly reduces the inductive voltage losses in the transmission line, permitting a greater fraction of the overall voltage on the capacitor bank to appear across the coil. One also observes that the impedances between the coil and capacitor bank in configuration 2 are relatively low, with the voltage on the coil much more closely coupled to the capacitor bank voltage than in configuration 1. In configuration 1, not only does more than half of the voltage not appear across the inductive coil load, but the reactance of the transmission line causes the coil voltage to appear partly out of phase relative to the bank voltage.

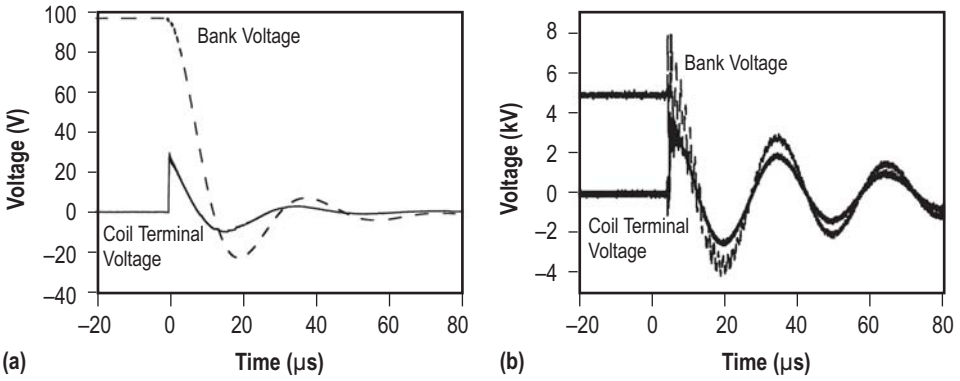

Figure 11. Measured capacitor bank voltage and coil terminal voltage for (a) configuration 1 discharged at 100 V and (b) configuration 2 discharged at 5 kV.

2.3.2 Visual Imaging

Time-integrated images of the 38° CTP thruster operating in configuration 2 on argon and xenon propellants at a discharge voltage of 5 kV are presented in figures 12(a) and (b), respectively. The images show a visually intense discharge within the cone in both cases. The 'halo' seen outside of the discharge channel is believed to be gas outside of the cone being partially ionized through interaction with the magnetic field, which is solenoidal, extending outside of the cone and wrapping around to the back of the thruster. In earlier testing with this geometry, plasma was also formed on the outside surface of the cone. The continuous flow increased the background pressure within the chamber significantly during testing (high 10^{-5} to mid-10^{-4} torr). This permitted the highly oscillating field, acting in the presence of the plasma being formed in the thruster cone to ionize gas outside of the thruster as well. The back side of the thruster cone was filled with foam to interrupt the plasma pathways and provide a mechanism to collisionally quench any plasma currents induced there, but this was not implemented in front of the thruster, and as such, the halo persisted at higher pressures. This feature was not seen on all pulses and was dissipated with reduced flow rate. The authors refrain from encouraging one-to-one comparisons of the intensity and spatial extent of the luminosity here because detailed plasma measurements are not presently available to support such speculation.

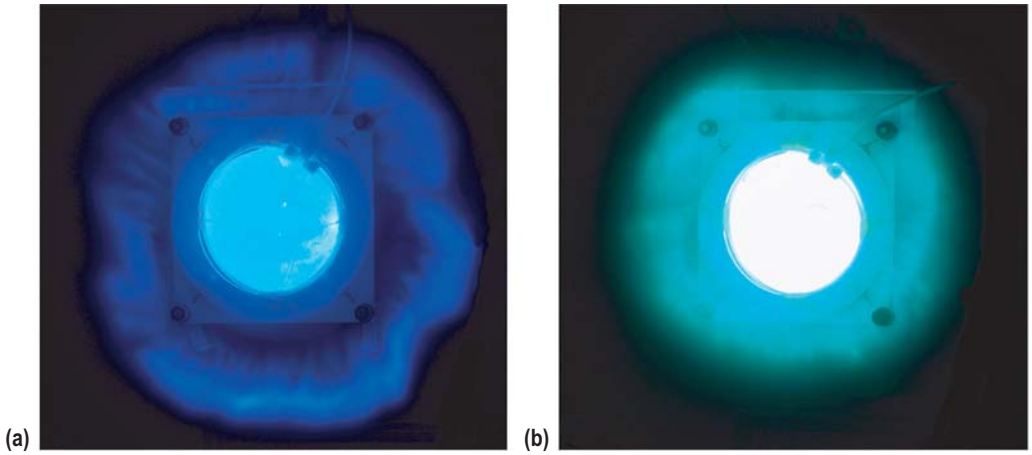

Figure 12. Time-integrated photographs of the 38° CTP thruster operating in configuration 2 at 5 kV capacitor bank charge voltage on (a) argon and (b) xenon propellant.

Time-resolved images of the CTP thruster are presented in figure 13. These images were obtained at a framing rate of 1 MHz, with an exposure time of 250 ns. The images are monochromatic and unfiltered, with the recorded intensities representing all light collected from the discharge during the exposure time. A current waveform, obtained for a discharge at a capacitor bank charge voltage of 4 kV, is included with the frames to provide a temporal orientation showing when these images were obtained during the pulse.

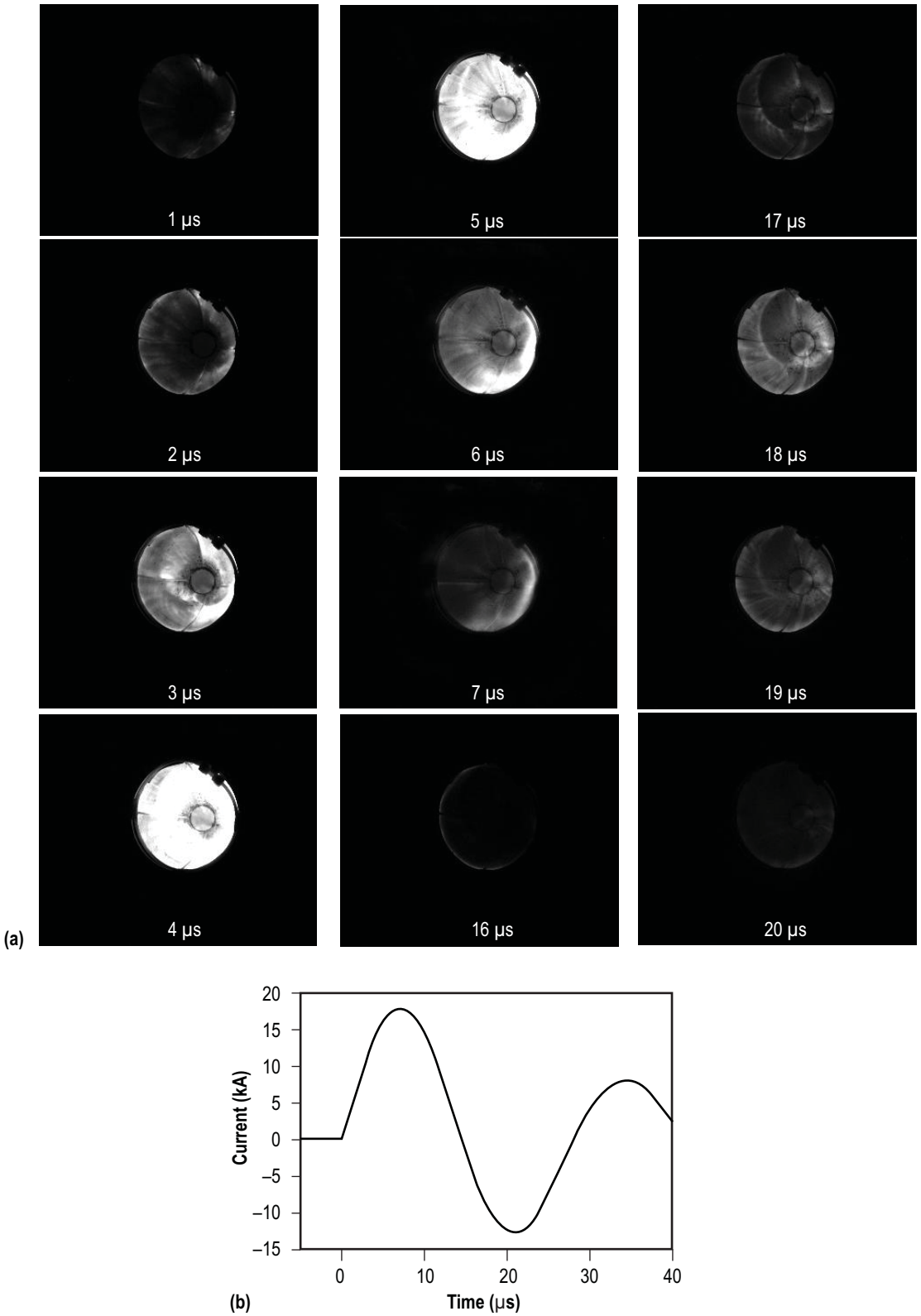

Figure 13. Time-resolved (black and white) images of (a) the 38° CTP thruster obtained with an image gate time of 250 ns for the times indicated in the frames, and (b) the current waveform at 4 kV capacitor charge voltage.

The images presented show the light emitted by the plasma over the first two half-cycles of the discharge. For the record, the glow at the end of the first half-cycle is faint but continues beyond that shown to time (t) = 11 μs. Also not shown is a faint glow that appears in the first few frames of the third half-cycle. The plasma during each half-cycle initiates at the times where the coil current crosses zero, as these represent the times of greatest change in the coil current (greatest dI/dt), and consequently the greatest value of the induced fields in the plasma. The light emission starts near the exit of the thruster at t = 1 μs (first half-cycle) and t = 16 μs (second half-cycle) and expands backwards towards the narrow end of the cone, growing in intensity until peaking a few microseconds into the half-cycle. There are visible nonuniformities in the light emission, but the emission grows to a very intense level (nearly saturating the camera) over the entire interior volume during the first half-cycle of the pulse. During the second half-cycle, the glow is less intense and shorter lived. This could be due either to the lower level of current during the second half-cycle or the reduction in gas near the coil as it may have been partially accelerated away from the coil during the first half-cycle.

2.3.3 Thruster Performance Measurements

Performance measurements on multiple CTP thrusters with different coil angles are presented in figure 14. Impulse bit measurements are presented in figures 14(a) and (b) for operation on argon and xenon, respectively. The maximum measured impulse bit was approximately 1 mN-s for both propellants and was only produced by the thruster with a 38° half-cone angle. When the mass flow rate was increased beyond the range for which data are presented in this TP, the base pressure in the vacuum vessel increased to values at which high-voltage arcing prevented performance measurements. The impulse bit peaks faster for xenon propellant, and the performance is much improved on xenon at 20° relative to argon at the same angle. One can speculate that xenon, being a heavier gas, may remain nearer to the coil for a longer period of time. This would leave a greater mass of propellant within the volume in which electromagnetic coupling between the coil and the plasma is possible, permitting better electrodynamic energy transfer.[16]

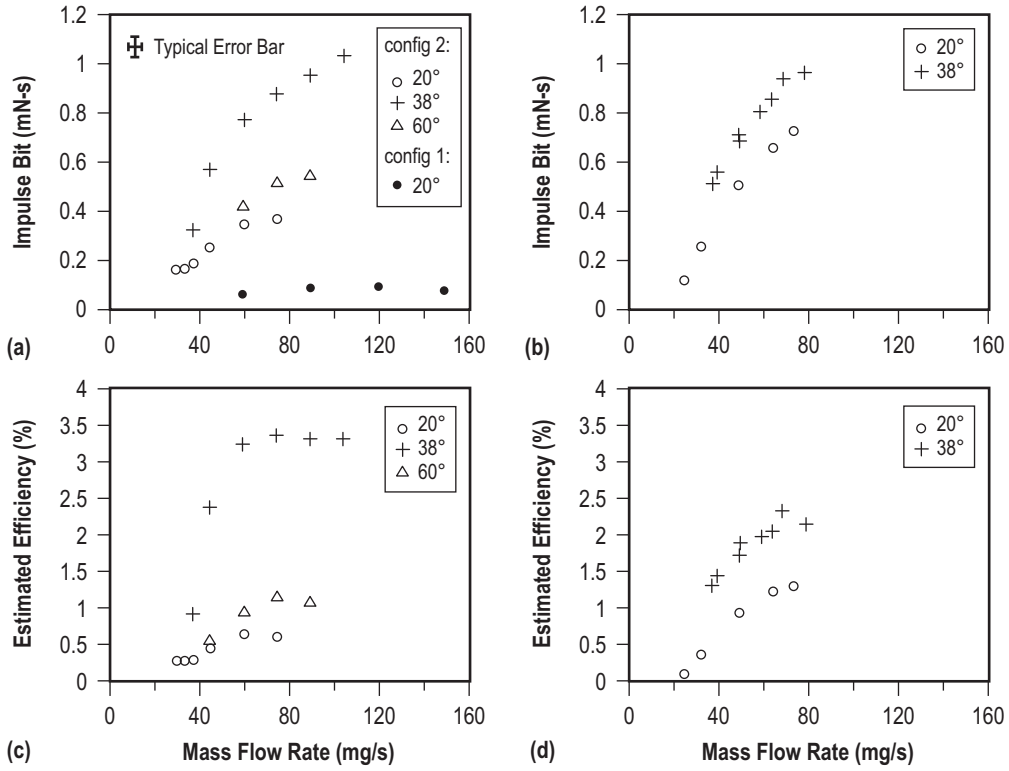

Figure 14. Measured impulse bit (with a typical error bar displayed) of the CTP as a function of steady-state mass flow rate for operation on (a) argon and (b) xenon, as well as estimated efficiency for operation on (c) argon and (d) xenon. All data obtained were for single-pulse operation at a charge voltage of 5 kV (500 J/pulse).

Since a steady-state propellant feed was used, an estimate of the mass bit (m_{bit}) must be made to undertake calculation of an estimated efficiency. A characteristic length for gas injection is taken as the cone axial length (l). A characteristic time for gas injection is estimated as

$$t_{\text{char}} = \frac{l}{a} \quad , \tag{1}$$

where a is the sound speed of the gas (at 25 °C). The mass bit is then further estimated as the amount of gas that would enter the thruster in this characteristic time

$$m_{\text{bit}} = t_{\text{char}} \dot{m} \quad , \tag{2}$$

where $\dot{m}$ is the mass flow rate. This assumption is consistent with operation of a PGV that only permits gas to flow into the thruster over the length of time t_{char}. The efficiency (η) is obtained using the measured impulse bit (I_{bit}), initial charge voltage (V_0), bank capacitance (C), and the estimated mass bit:

$$\eta = \frac{{I_{bit}}^2}{m_{bit} C {V_0}^2} \quad . \tag{3}$$

The estimated efficiency for operation on argon and xenon propellants is given in figures 14(c) and (d). It is observed that when estimated in this manner, the efficiency is only a few percent. Interestingly, the efficiency calculated for operation on xenon at a cone angle of 20° is greater than that on argon at the same angle, but these trends are reversed at 38°.

It should be noted that low-power planar (flat-plate) PITs were highly lossy, producing incompletely formed current sheets (magnetically permeable with comparable magnetic convection and diffusion timescales) with a high degree of spatial variability. They were also tested in a 'static' gas fill configuration, and much of the inductive work was expended in entrainment of the gas, which is a highly inelastic process leading to inherently low efficiencies. For example, a 20-cm, flat-plate thruster only had an efficiency of a few percent in the static fill case.[1] The authors expected similar gas profiles and entrainment losses in the CTP thruster employing continuous gas injection, so the low-efficiency results are unsurprising. By way of comparison, the PIT MkI and MkV, which were far better optimized in an electrodynamic sense and had pulsed propellant injection, only yielded efficiencies in the range of 15% to 30% on argon.

The force vector in PITs is generally directed perpendicular to the coil. Unlike the planar PITs, the force vector applied to the plasma in the CTP thruster has a significant component in the radial direction, which, excluding any energy recovery mechanisms, does not contribute to the impulse bit. This might lead to the conclusion that the greater angle should perform better, but this is not shown in the impulse bit data where the 38° cone performed best.

In the present CTP thruster testing, direct comparison of performance measurements of thrusters with different cone angles is complicated by the energy expended on gas entrainment and the potential containment of gas provided by the smaller angle cones. Comparison of the results presented in this TP with results from previous experimental campaigns is complicated by the stray inductance remaining in the system for configuration 1 and, to a lesser but still significant extent, configuration 2. The data presented herein are not sufficient to deconvolve the acceleration picture beyond what has been speculated in the preceding discussion.

2.4 Conical Theta-Pinch Current Sheet Modeling

Current sheet acceleration modeling was performed to gain understanding of the CTP thruster. There exists a one-dimensional IPPT acceleration model consisting of a set of circuit equations coupled to a one-dimensional momentum equation. The one-dimensional model was adapted for use on devices like the CTP thruster, where two-dimensional plasma acceleration was expected. This work is further discussed in reference 20.

2.4.1 Two-Dimensional Inductive Acceleration Model

An IPPT can be electrically modeled as a circuit,[2,20,21] shown in figure 15(a), where current I_1 is in the driving circuit, while I_2 is the current flowing in the plasma. The two currents are coupled like a transformer through a time-varying mutual inductance (M) between the external circuit and plasma. The circuit is completed with a capacitor bank having a capacitance (C), an initial (parasitic) inductance (L_0), an acceleration coil inductance (L_C), a plasma resistance (R_p), and an external resistance (R_e) in the driving circuit.

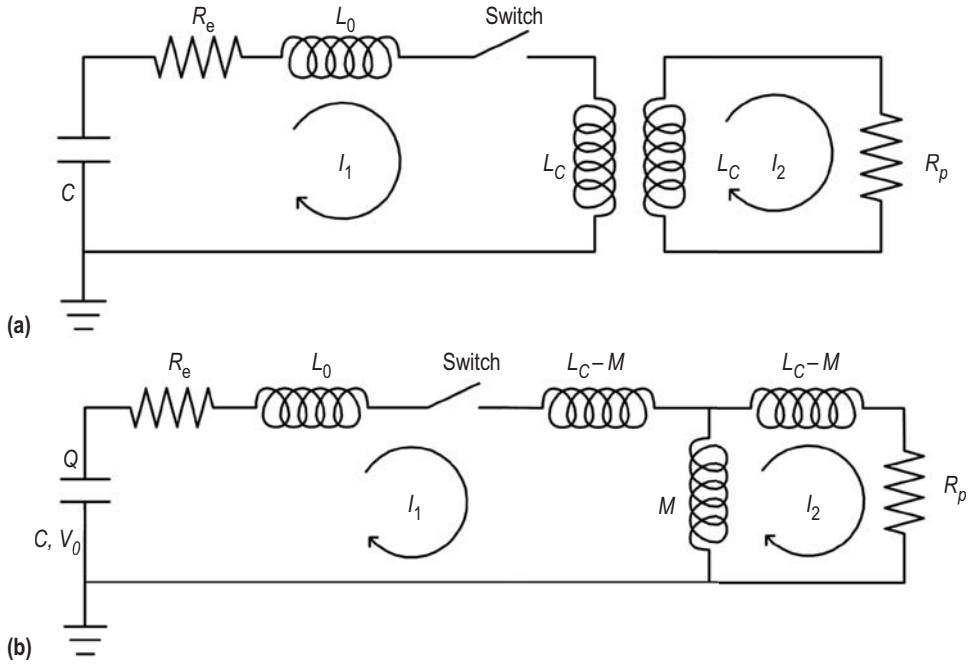

Figure 15. Model of (a) general lumped-element circuit and (b) equivalent circuit of an IPPT.

An equivalent circuit, shown in figure 15(b), can be drawn to permit the application of Kirchoff's law to each loop in the circuit. Rearranging the results and adding a statement for the time rate of change of charge on the capacitor yields

$$\frac{dI_1}{dt} = \frac{L_C V - L_C R_e I_1 - M R_p I_2 + \left(L_C I_2 + M I_1\right) dM/dt}{L_C\left(L_0 + L_C\right) - M^2} \quad , \tag{4}$$

$$\frac{dI_2}{dt} = \frac{M\, dI_1/dt + I_1\, dM/dt - R_p I_2}{L_C} \quad , \tag{5}$$

and

$$\frac{dV}{dt} = -\frac{I_1}{C} \quad , \tag{6}$$

where V is the voltage on the capacitor bank, initially charged to a voltage V_0.

If the resistive elements can be neglected, then the series and parallel lumped inductive elements shown in figure 15(b) combine to yield a total inductance:

$$L_{\text{tot}} = L_0 + L_C - \frac{M^2}{L_C} \quad . \tag{7}$$

The total inductance in the system varies as a function of time only due to the mutual inductance term, which varies as the relative positions of the current sheet and coil change. An expression for the total inductance as a function of current sheet axial and radial position has been empirically determined as

$$L_{\text{tot}}(\overline{r}, z) = L_0 + L_C \left[1 - \exp\left(-z / z_0\right) \left(\frac{\overline{r}}{\overline{r_{\text{coil}}}} \right)^N \right] , \tag{8}$$

where

$\overline{r}$ = average radial position of the current sheet
$\overline{r_{\text{coil}}}$ = average radial position of the coil
z = axial displacement of the current sheet
N = fit parameter found to be close to 2 for all cases studied here
z_0 = axial decoupling distance.

This expression is set equal to the previous expression for total inductance (eq. (7)) and solved to yield the mutual inductance as a function of the axial and radial separation distance between the driving coil and the current sheet:

$$M = L_C \exp\left(-\frac{z}{2z_0} \right) \left(\frac{\overline{r}}{\overline{r_{\text{coil}}}} \right)^{N/2} \quad . \tag{9}$$

The time derivative of equation (9) is

$$\frac{dM}{dt} = \frac{L_C}{\overline{r_{\text{coil}}}^N} \frac{N}{2} \overline{r}^{\left(\frac{N}{2}-1\right)} \frac{d\overline{r}}{dt} \exp\left(-\frac{z}{2z_0} \right) - \frac{L_C}{2z_0} \exp\left(-\frac{z}{2z_0} \right) \frac{dz}{dt} \left(\frac{\overline{r}}{\overline{r_{\text{coil}}}} \right)^{N/2} \quad . \tag{10}$$

If the potential energy of a system is a function of position, then the force in the *i*-th direction can be obtained by calculating the partial derivative of the potential energy with respect to change in the *i*-th coordinate. For an IPPT, the force in the *i*-th direction is given as

$$F_i = \frac{{I_1}^2}{2}\frac{\partial L}{\partial x_i} \quad . \tag{11}$$

In the radial direction, this force is opposed by a gas-dynamic pressure force (P_2) that increases as the current sheet moves toward the thrust axis. If the current sheet is assumed to act as a normal shockwave, then the pressure ratio across the shock is given as

$$\frac{P_2}{P_1} = 1 + \frac{2\gamma}{\gamma + 1}\left(\mathrm{M}^2 - 1\right) \quad , \tag{12}$$

where

P_1 = pressure upstream of the shock
P_2 = pressure of the gas downstream of the shock
γ = ratio of specific heats (taken here to be 5/3).

The local Mach number (M) upstream of the shock is

$$\mathrm{M} = \frac{u}{\sqrt{\gamma k T_1 / m_i}} \quad , \tag{13}$$

where

u = shock velocity in the given direction
k = Boltzmann's constant
T_1 = temperature of the gas upstream of the shock
m_i = mass of an ion.

Assuming that all the mass is initially entrained in the current sheet (no 'snowplowing' or entrainment of gas during the discharge), Newton's second law can be written in the axial and radial directions using equations (11) and (12) as

$$\frac{dv_z}{dt} = \left[\frac{L_C {I_1}^2}{2z_0}\exp\left(-\frac{z}{z_0}\right)\left(\frac{\bar{r}}{\overline{r_{\mathrm{coil}}}}\right)^N\right] / m_{\mathrm{bit}} \tag{14}$$

and

$$\frac{dv_r}{dt} = \left[P_2 2\pi \bar{r} l_{\mathrm{coil}} - \frac{L_C {I_1}^2 N}{2\overline{r_{\mathrm{coil}}}^N}\exp\left(-\frac{z}{z_0}\right)\bar{r}^{N-1}\right] / m_{\mathrm{bit}} \quad , \tag{15}$$

where

m_{bit} = total propellant mass in the current sheet
v_z = axial current sheet velocity
v_r = radial velocity.

The axial z and radial $\overline{r}$ positions are related to the velocities as

$$\frac{dz}{dt} = v_z \tag{16}$$

and

$$\frac{d\overline{r}}{dt} = v_r \quad . \tag{17}$$

The time evolution of the pressure P_2 is given by the time derivative of equation (12):

$$\frac{dP_2}{dt} = \frac{P_1 2\gamma}{\gamma + 1} \frac{m_i}{\gamma k T_1} 2 v_r \frac{dv_r}{dt} \quad , \tag{18}$$

bringing the total number of first-order coupled ordinary differential equations in the system to nine.

Of the nine equations (eqs. (4)–(6), (10), and (14)–(18)), six are connected to the semiempirical relation for coil inductance as a function of current sheet location. No attempt has been made here to model the conversion of radial current sheet motion into axial momentum. In addition, this TP will focus only on thrust efficiency, with no attempt made to model factors that could be a function of the coil geometry, such as propellant utilization efficiency.

2.4.2 Magnetic Field Finite Element Analysis

The inductive coupling between coils and current sheets in various geometries were simulated using finite element analysis to explore the range of validity of equation (8). The finite element modeling was used to compute the inductance as a function of radial and axial displacement of the current sheet from the coil. The coil geometry is shown and labeled in figure 16. The geometry will be designated in this section as a number and a letter (e.g., 5S). In this designation, the number represents the half-cone angle, and the letters 'S,' 'M,' and 'L' refer, respectively, to coils with lengths (l_{coil}) that are short (5 cm), medium (6–8 cm), or long (10 cm). All coils have a minor radius (r_{coil}) of 4 cm. One coil has no letter in its designation because it is a flat-plate with an angle of 90° and $l_{coil} = 0$.

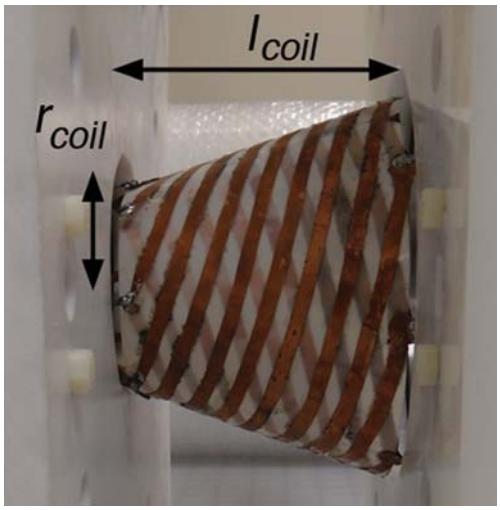

Figure 16. CTP thruster coil geometry.

Using the calculated inductance data, a coil inductance (L_C) and decoupling length (z_0) were obtained by curve fitting equation (8) to the simulated inductance data for constant radial current sheet positions equal to $\overline{r_{coil}}$. Inductance was then calculated using equation (8) over a range of radial and axial current sheet positions, with the results of these calculations shown as solid lines in figures 17–19. The simulation data for these geometries are plotted in the figures, with each different marker style corresponding to data at an individual fixed axial location. In these figures, the agreement between the finite element results and equation (8) is good for half-cone angles from 20° to 55°, as seen in figure 18. The ability of the equation to accurately model the inductance begins to break down outside this range, as observed in figures 17 and 19.

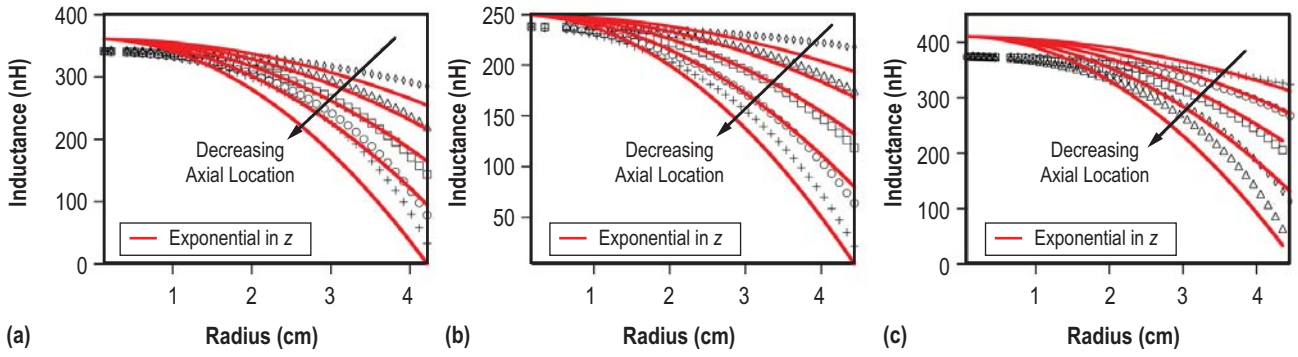

Figure 17. Finite element modeling results (markers) and the semiempirical model of equation (8) (red lines) for inductance as a function of average radial current sheet position: (a) 5S, (b) 5L, and (c) 12S. Each different marker style corresponds to simulation data at an individual, fixed axial location.

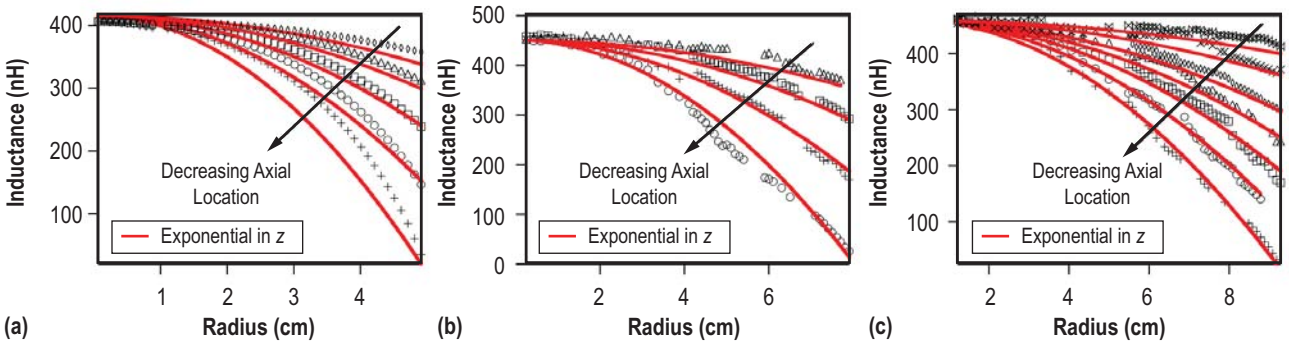

Figure 18. Finite element modeling results (markers) and the semiempirical model of equation (8) (red lines) for inductance as a function of average radial current sheet position: (a) 20S, (b) 38L, and (c) 55M. Each different marker style corresponds to simulation data at an individual, fixed axial location.

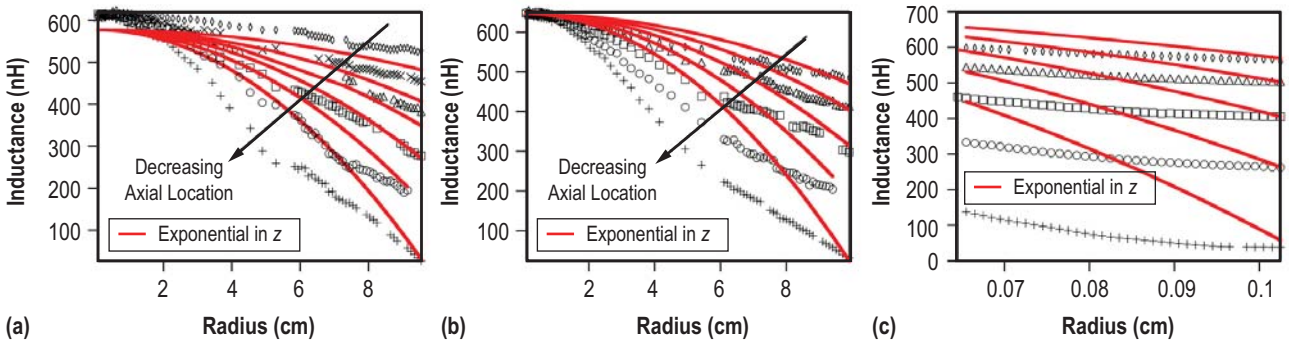

Figure 19. Finite element modeling results (markers) and the semiempirical model of equation (8) (red lines) for inductance as a function of average radial current sheet position: (a) 62M, (b) 70S, and (c) 90° (flat-plate). Each different marker style corresponds to simulation data at an individual, fixed axial location.

For coils with a half-cone angle below 12°, it is the axially varying part of equation (8) that begins to deviate from the modeled inductance. It was found that an error function is better than an exponential at modeling the axial variation of inductance in these situations. A comparison between the two functions is presented in figure 20.

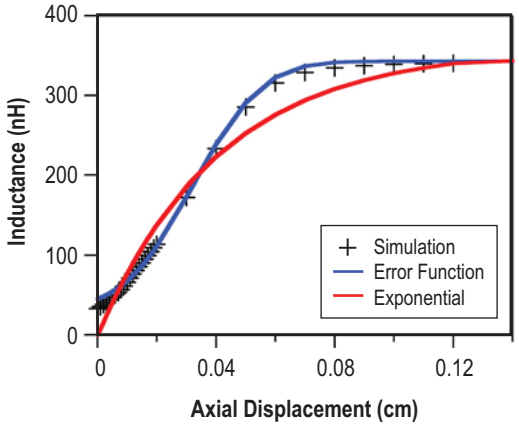

Figure 20. Comparison between an error function (blue) and an exponential function (red) fit to data for the inductance as a function of current sheet axial position (markers) in the case of a 5° cone.

Plots of the inductance function, calculated using an exponential function in z (eq. (8)) and then using an error function in z instead of the exponential, are presented for comparative purposes in figure 21. The data clearly show that the error function does a better job fitting the data while the exponential deviates further from the data points as the angle is decreased. Recently, the error function was successfully used for the axial inductance function in work modeling a coilgun.[22]

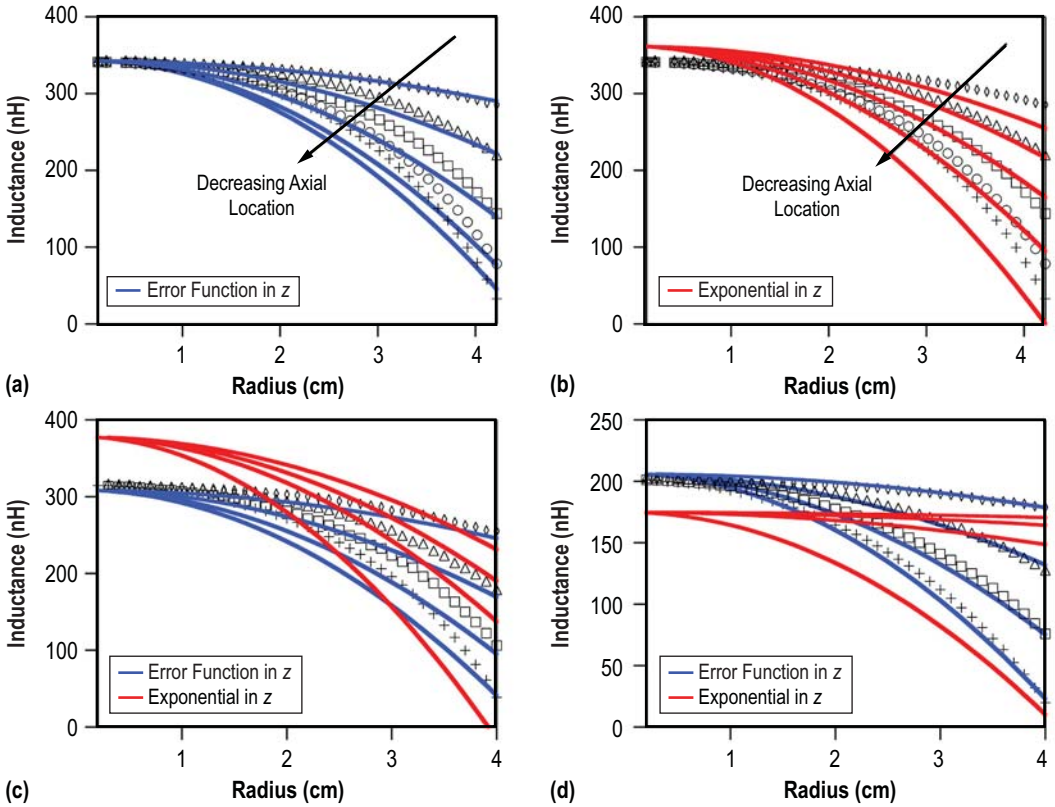

Figure 21. Comparison of the accuracy of two functional fits (exponential in z (red lines), and an error function in z (blue lines)) for the inductance as a function of current sheet axial and radial position, with data given as markers. Each different marker style corresponds to simulation data at an individual, fixed axial location: (a) 5S (error function in z), (b) 5S (exponential in z), (c) 0S, and (d) 0L.

2.4.3 Nondimemsionalization of the Model

The equation set found in section 2.4.1 can be nondimensionalized by making the following substitutions:[21]

$$
\begin{aligned}
I_1^* &= \frac{1}{V_0}\sqrt{\frac{L_C}{C}}I_1 \quad & I_2^* &= \frac{1}{V_0}\sqrt{\frac{L_C}{C}}I_2 \\
V^* &= \frac{V}{V_0} & M^* &= \frac{M}{L_C} \\
v_z^* &= \frac{\sqrt{L_0 C}}{z_0}v_z & z^* &= \frac{z}{z_0} \\
v_r^* &= \frac{\sqrt{L_0 C}}{r_{\text{coil}}}v_r & r^* &= \frac{\bar{r}}{r_{\text{coil}}} \\
t^* &= \frac{t}{\sqrt{L_0 C}} & P^* &= \frac{P}{P_1} \quad .
\end{aligned}
\tag{19}
$$

Applying these substitutions to equations (4)–(6), (10), and (14)–(18) yields the following nondimensional equation set:

$$\frac{dI_1^*}{dt^*} = \left[L^* V^* + \left(M^* I_1^* + I_2^* \right) \frac{dM^*}{dt^*} - \psi_2 L^* I_2^* M^* - \psi_1 L^* I_1^* \right] / \left[\left(L^* + 1 \right) - M^{*2} \right] \ , \tag{20a}$$

$$\frac{dI_2^*}{dt^*} = M^* \frac{dI_1^*}{dt^*} + I_1^* \frac{dM^*}{dt^*} - I_2^* L^* \psi_2 \ , \tag{20b}$$

$$\frac{dV^*}{dt^*} = -I_1^* \ , \tag{20c}$$

$$\frac{dM^*}{dt^*} = \frac{N}{2} r^{*\left(\frac{N}{2}-1\right)} v_r^* \exp\left(-\frac{z^*}{2} \right) - \frac{1}{2} r^{*\frac{N}{2}} v_z^* \exp\left(-\frac{z^*}{2} \right) \ , \tag{20d}$$

$$\frac{dv_r^*}{dt^*} = \lambda P^* r^* - \varphi I_1^{*2} r^{*(N-1)} \exp\left(-z^* \right) \ , \tag{20e}$$

$$\frac{dr^*}{dt^*} = v_r^* \ , \tag{20f}$$

$$\frac{dv_z^*}{dt^*} = \alpha I_1^{*2} r^{*N} \exp\left(-z^* \right) \ , \tag{20g}$$

$$\frac{dz^*}{dt^*} = v_z^* \ , \tag{20h}$$

and

$$\frac{dP^*}{dt^*} = \Xi v_r^* \frac{dv_r^*}{dt^*} \ . \tag{20i}$$

The terms α, L^*, ψ_1, ψ_2, ϕ, λ, and Ξ are the relevant nondimensional scaling parameters of the system and are defined as

$$\alpha = \frac{CV_0{}^2 L_C}{2m_{\text{bit}} z_0{}^2} \qquad L^* = \frac{L_0}{L_C}$$

$$\psi_1 = R_e \sqrt{\frac{C}{L_0}} \qquad \psi_2 = R_p \sqrt{\frac{C}{L_0}}$$

$$\varphi = \frac{CV_0{}^2 L_C}{2m_{\text{bit}} \overline{r_{\text{coil}}}^2} \qquad \lambda = \frac{L_0 C P_1 2\pi l_{\text{coil}}}{2m_{\text{bit}}}$$

$$\Xi = \frac{4\gamma}{\gamma+1} \frac{m_i}{\gamma k T_1} \frac{1}{r_{\text{coil}}{}^2 L_0 C} \ . \tag{21}$$

The parameters ψ_1 and ψ_2 are critical resistance ratios that provide a measure of the effects of current damping in the pulse. The term L^* is a ratio of the initial (also called 'fixed' or inaccessible) inductance in the circuit to the accessible inductance (also known as the inductive 'stroke' or inductance change as the current sheet moves to infinity). This ratio represents a measure of the fraction of input electromagnetic energy that can be transferred to inductive acceleration of the current sheet. The physical interpretations of these three parameters remain unchanged as compared to those of previous studies of IPPTs with flat inductive coil geometries, and more information on them can be found in reference 21.

The term λ appears as a new parameter in this model, and it addresses the magnitude of the gas-dynamic pressure in opposing radially inward current sheet motion. Another new parameter is Ξ, which is a measure of the growth rate of the gas-dynamic pressure as the current sheet shock front undergoes radial acceleration. For the calculations contained in this TP, these parameters are fixed at the following values: $L^* = 0.18$, $\psi_1 = 0.05$, $\psi_2 = 0.01$, $\lambda = 7 \times 10^{-7}$, and $\Xi = 2.3 \times 10^4$.

The parameter α is called the dynamic impedance ratio, and it can be expanded into a product of physically meaningful ratios,[21,23]

$$\alpha = \frac{C^2 V_0{}^2 L_C}{2m_{\text{bit}} z_0{}^2} = \frac{1}{8\pi^2} \frac{CV_0{}^2/2}{m_{\text{bit}} v_z{}^2/2} L^* \left(\frac{2\pi\sqrt{L_0 C}}{L_0 / \dot{L}_z} \right)^2 , \tag{22}$$

where $\dot{L}_z = v_z L_z'$ and $L_z' = L_C / z_0$. The second ratio on the right-hand side represents the inverse of thrust efficiency, and the third term is the previously discussed inductance ratio. The final term represents a ratio between the characteristic ringing time of the driving circuit and the characteristic time over which the current sheet will increase the inductance of the circuit by one unit of L_0 owing to axial motion. The latter is an effective measure of the time that the plasma remains electromagnetically coupled to the driving circuit. Consequently, the parameter α is a measure of the dynamic impedance match between the natural period of the driving circuit and the inertial timescale on which the axially moving current sheet can accept energy from the circuit in the form of further axial current sheet acceleration. It has been shown in the one-dimensional modeling case that there

exists an optimum α for which the thrust efficiency η_t is maximized, corresponding to an IPPT that is dynamically impedance matched.[21] The thrust efficiency can be written in terms of the nondimensional parameters as

$$\eta_t = \frac{v_z^{*2}}{2L^*\alpha} \quad . \tag{23}$$

While α appears in the axial equation of motion and pertains to inductive dynamic impedance matching for an axially translating plasma, the parameter ϕ is new, appearing in the equation of motion for a radial translation. This parameter can be similarly expanded as

$$\varphi = \frac{C^2 V_0^{\,2} L_C}{2 m_{\text{bit}} r_{\text{coil}}^{\,2}} = \frac{1}{8\pi^2} \frac{C V_0^{\,2}/2}{m_{\text{bit}} v_r^{\,2}/2} L^* \left(\frac{2\pi\sqrt{L_0 C}}{L_0 / \dot{L}_r} \right)^2 \quad , \tag{24}$$

where $\dot{L}_r = v_r L_r'$ and $L_r' = L_C / \overline{r_{\text{coil}}}$. The second term no longer represents thrust efficiency, but it is the inverse of the fraction of total input energy converted into radial kinetic energy. The fourth term is the ratio of the characteristic circuit time to the inertial timescale on which the radially moving current sheet can accept energy from the circuit in the form of further radial current sheet acceleration.

2.4.4 Model Results and Discussion

Simulations were first undertaken permitting unrestrained axial acceleration for a fixed radial position. The efficiency as a function of α computed for these simulations is presented in figure 22. For the case where $r = \overline{r_{\text{coil}}}$ throughout the simulation, the result of reference 21 yielding maximum thrust efficiency at a value of α between 1 and 3 is recovered. When the current sheet is arbitrarily moved to closer to the centerline (e.g., moved to a smaller radial distance from $r = 0$) and then held at that radial position throughout the simulation, one observes in figure 22 that the magnitude of achievable η_t is globally decreased, and the maximum value of η_t occurs at a higher value of α.

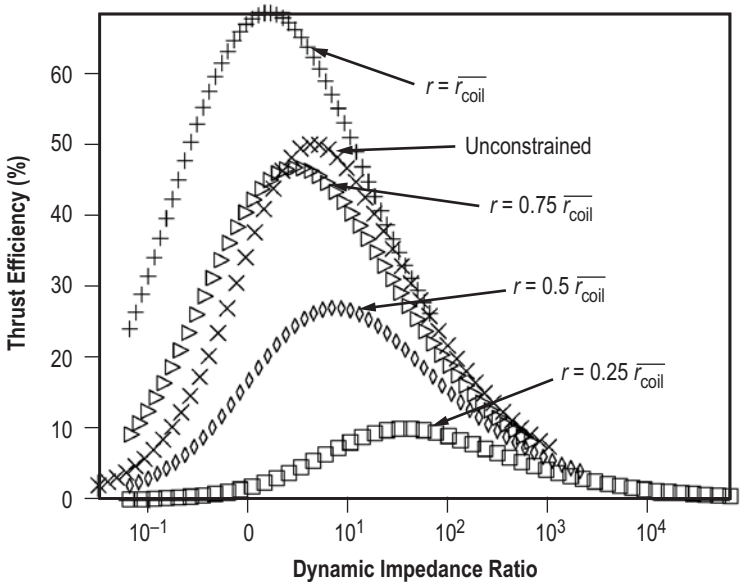

Figure 22. Calculated thrust efficiency as a function of α for different radial current sheet displacements.

A possible explanation for the shift in optimum values of α is that as the current sheet is radially displaced, the inductive coupling to the coil is weakened, and the rate of inductive energy transfer from the acceleration coil to the current sheet is reduced. However, information regarding this weakened coupling as a function of radial translation is not contained in α. Consequently, the effect is to demand a longer circuit timescale to maximize the energy transfer to axial motion of the current sheet, which leads to a greater α for maximum efficiency. However, the maximum energy transfer is globally reduced because no matter how the circuit is adjusted, the potential acceleration of the sheet has been reduced by initially displacing the sheet from the coil.

The efficiency for the case where the radial motion is allowed to evolve according to equation (20e) is also graphed as a function of α in figure 22. One observes that the effect is to lower the efficiency from the peak where the sheet is constrained to a radial position $r = \overline{r_{coil}}$ and to shift the peak to a greater value of α. However, the overall effect is tempered to some extent relative to the cases where the calculation was started at an arbitrary, fixed radial current sheet position by the fact that, even though the sheet is free to move radially inward, it starts at the position $r = 0$, so it is initially well coupled to the coil.

As observed in figure 23, the effect on efficiency is more pronounced and detrimental as the value of ϕ is increased, which is indicative of faster electromagnetic decoupling owing to radial motion. In other words, a large value of ϕ corresponds to a case where the inertial timescale for the plasma to accept energy and convert it into radial kinetic energy is short. However, a change in inductance due to motion in either direction affects the overall electromagnetic coupling, so for a fixed α faster conversion of energy to radial motion (increasing ϕ) deprives the plasma of the time needed to acquire axial kinetic energy and subsequently lowers the ceiling on the axial kinetic energy that can be transferred. It can be concluded that, while maximizing the coupling of energy into axial

motion is beneficial to thrust efficiency, coupling of energy into radial motion has a generally detrimental effect on thrust efficiency (in the context of this model, which has no radial-to-axial momentum transfer mechanism). This would indicate a decreasing η_t for increasing values of ϕ, as observed in the contour plot of efficiencies presented in figure 24. One also observes that as ϕ is increased, the peak efficiency occurs at a higher value of α, which is expected based on the results in figure 22 because the plasma accelerating more rapidly spends less time close to $r = \overline{r_{\text{coil}}}$.

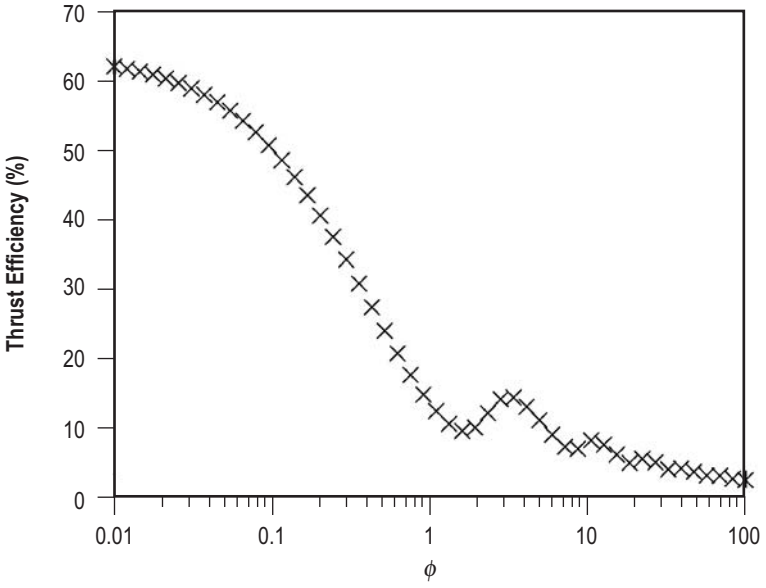

Figure 23. Calculated thrust efficiency as a function of ϕ for radial motion governed by equation (20e) with $\alpha = 0.6$.

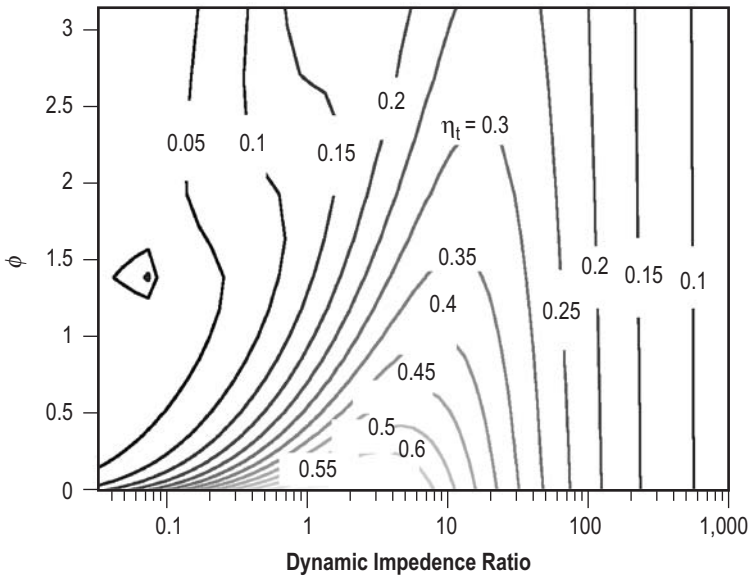

Figure 24. Calculated thrust efficiency contours as a function of α and ϕ.

2.5 Summary Remarks

In this section, measurements on several CTP IPPTs were presented, showing measured impulse bits and estimated efficiencies for several different cone angles and continuous mass flow rates. The data show a peak value of impulse bit and efficiency for the 38° cone angle. Modeling of IPPTs where radial motion is permitted seems to indicate that any radial motion is detrimental to thrust efficiency; however, caution must be exercised when applying these results to the data. First, there is no mechanism in the model to permit radial-to-axial momentum transfer, so any energy initially shunted into radial motion is essentially lost in the model. Second, the authors employed a normal shock relation to evolve the pressure as a function of time, but this may not be the proper model to use for this process. Third, and likely most important, the model was constructed assuming that all mass is initially in the current sheet, with no mass entrainment included. The snowplowing and entrainment of gas by the current sheet, and even the containment of the neutral gas within the cone volume, are not well quantified and captured within the model, but previous work has shown that mass entrainment can have a very large effect on calculated performance.[21] Also, the inductance function, while working well for some cone angles, is not globally applicable to IPPTs with widely varying geometries. Finally, while the model accounts for momentum transfer in both the axial and radial directions, it does not include a self-consistent predictive model for the overall energy in the system as other recent works by Polzin et al.[24] have contained (K.A. Polzin et al.: "Inductive Pulsed Plasma Thruster Model with Time-Evolution of Energy and State Properties," *J. Appl. Phys.*, to be published). Thus, while the modeling performed herein is insightful, it certainly has areas that would benefit from additional future refinement.

3. REPETITION-RATE TEST APPARATUS

Continuous, repetition-rated testing of an IPPT requires a high-voltage, high-power capacitor charge system. Such a system was assembled and used to accomplish repetition-rated operation of a CTP IPPT. This system, shown in figure 25, is located adjacent to the 2.75-m- (9-ft-) diameter electric propulsion vacuum testing facility at MSFC. An electrical schematic of the system is shown in figure 26, with the major components of the system described and testing results presented within this section.

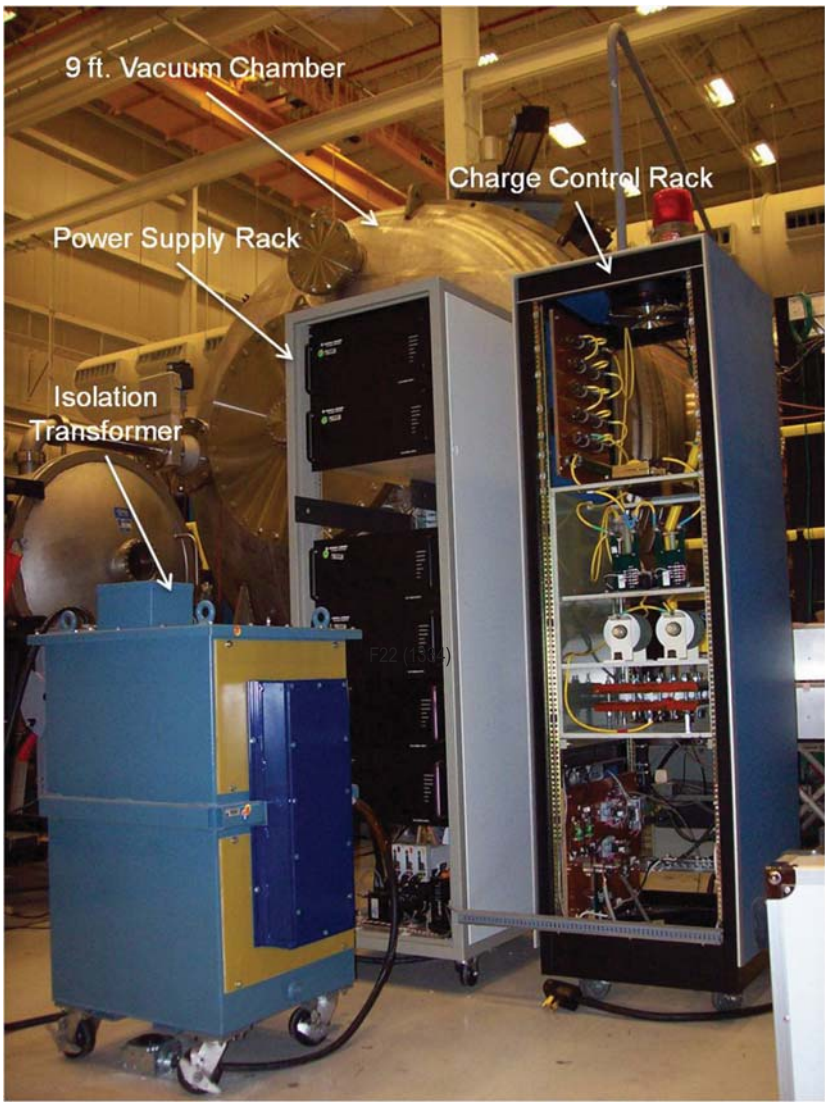

Figure 25. High-voltage, high-power capacitor charge system located next to the 2.75-m- (9-ft-) diameter electric propulsion vacuum testing facility at MSFC.

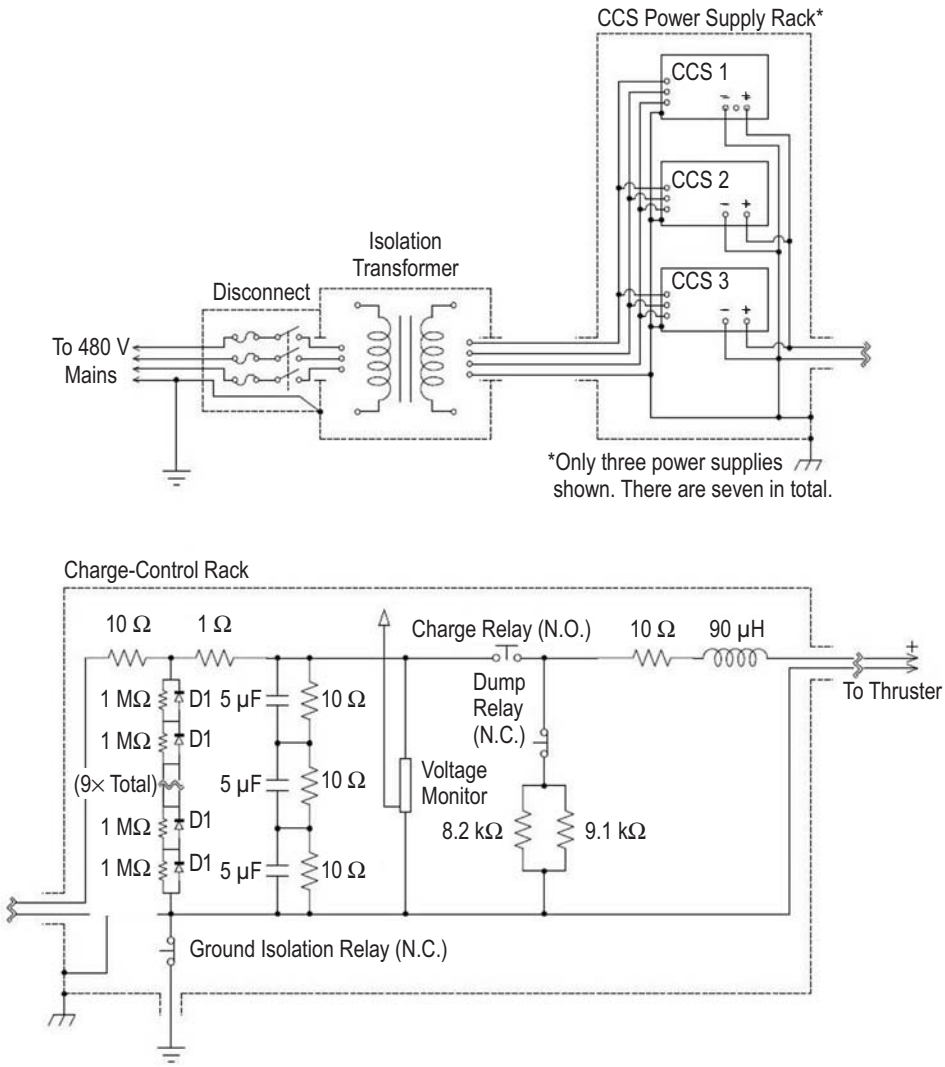

Figure 26. Fast-charge system circuit schematics (control components not shown): (a) CCS power supply rack and (b) charge-control rack.

3.1 Power Supply Rack

A custom high-voltage power supply to rapidly recharge capacitor banks was procured from General Atomics Electronic Systems in 2004. It consists of a bank of seven individual capacitor charging supply (CCS) series, high charge-rate power supplies (also made by General Atomics) installed in a single rack. The rack accepts 480 V/3∅ input power and has 120 VAC power (internally provided from the 480-V power by a step-down transformer), a fiber optic interface board (FIB) for remote control, and an interlock loop which shuts down the system if the back panel is opened.

3.1.1 Capacitor Charging Supply

The CCS series (formerly designated CCDS) power supply, with specifications given in reference 25, is designed for rapid, efficient charging of capacitor banks. The CCS uses a series resonant

inverter circuit topology, yielding efficiencies in excess of 85% with an average power factor 0.85. The supply incorporates fast overvoltage protection to prevent damage to the supply from an open-circuit load condition. They also have a fast-inhibit function, which rapidly disables the high-voltage output for 100–200 μs after the load discharges. This feature makes them ideally suited to powering repetitively pulsed thrusters. The fast-inhibit may also be initiated by an externally supplied command if the standard disable time is not suitable for the application.

Each supply in the rack has a maximum output voltage of 40 kV and is capable of delivering an average of 16 kJ/s DC power when charging to the maximum voltage. The average power throughput decreases linearly with the voltage setpoint, so at a charge voltage of 4 kV, the output power is 1.6 kJ/s. For a 40 μF bank, this corresponds to roughly 320 J/pulse, which leads to a bank recharge time of approximately 0.2 s. The output current at a given voltage setpoint is constant, and is equal to roughly 0.8 A in this example. The equations governing the supply output and used in the calculation of this example are summarized in reference 26.

Control of the supply is performed remotely through a 25-pin connector on the back panel, labeled J901. The primary control signals are a 'High-Voltage (HV) On' command (4–24 V active high), an 'HV Inhibit' command (4–24 V active low), and an analog voltage adjust (0–10 V full-scale). (The factory default for the 'HV Inhibit' command is 'active inhibit high,' meaning that a logical 'high' signal ($4\ \text{V} < V_{\text{HV,inhibit}} < 24\ \text{V}$) applied to the relevant pin of the J901 connector will shut off the high-voltage output while a logical 'low' ($V_{\text{HV,inhibit}} < 4\ \text{V}$) must be applied to enable the high-voltage output. The CCS at MSFC, however, are supplied with 'option 92,' also called 'active high enable,' which is the opposite of the default setting. Consequently, a logical high enables the high-voltage output while a logical low inhibits it. As the HV Inhibit function shuts off the CCS output the fastest (within 33 μs), it is recommended that this be the first control used to disable the high-voltage output, followed in order of increasing delay by removing the HV On signal, opening the interlocks, and, as a last resort in emergency situations only, the removal of line power to the supplies.) For voltage isolation and noise immunity, control signals and output voltage feedback (analog inputs and outputs) are communicated through an isolation amplifier while the logic signals (digital inputs/outputs) communicate through optocouplers. Each supply is also provided with an interlock, which is enabled by an external closure.

The required input voltage for the system is 480 V/3∅, wired in a four-wire delta configuration, with the maximum input power for each supply equal to 25 kVA. Each supply in the rack is protected with its own circuit breaker, which can be switched to the 'off' position to isolate those supplies which are not in use. The output polarity of the supplies is positive relative to the return (negative terminal), and the return is connected to the chassis ground. Each chassis is connected to the (local) chassis ground of the rack. The output power is conducted to the charge-control rack (described below) through an RG-8 cable, with the center conductor being positive and the braid at the potential of the local chassis ground. To charge a capacitor bank at a high rate, but at a lower voltage than the maximum, several supplies can be ganged in parallel. Any number of the seven supplies may be so connected using the provided jumper cables (RG-8 high-voltage coaxial cable).

3.1.2 Fiber Optic Interface Board

The FIB is located in the power supply rack and accepts 120 VAC power generated from the 480-V power feeding the rack. The FIB mediates two-way communication between the power supply rack and an external test control system, using serial commands to communicate with a companion board that interfaces with the control system through a serial-to-fiber-to-serial link. The FIB converts serial command data to the analog voltage and logical inputs required to control the CCS and converts analog and logical feedback from the CCS into serial data for transmission to the external control and monitoring system. The serial command protocols used by the FIB are described in reference 27. The FIB also has two fiber optic receivers for receipt of the HV On and HV Inhibit commands. These are logical signals that are received by the FIB, buffered, and then passed to the individual CCS. Each supply communicates with the FIB through its own individual cable.

3.2 Isolation Transformer

The power supply rack is presently powered through a 25-kVA, 3∅ isolation transformer (Del Electronics, model AD6391, serial No. 153096), which provides up to 60 kV of transient voltage isolation between the primary and secondary windings. A fused disconnect was installed on the transformer for manual shutdown of the system. The disconnect employs 30-A time-delayed fuses so as to accommodate the initial in-rush current when the disconnect switch is closed. The connection from the outlet to the transformer and from the transformer to the power supply rack is completed using SO-8 cable.

The isolation transformer permits floating of the entire charge system if it is desired to operate the thruster isolated from the facility ground. Use of the isolation transformer, however, limits the available input power to the supply to 25 kVA and consequently limits the CCS output power to 16 kW. For higher power operation, it would be necessary to either acquire a higher power isolation transformer or to directly power the supply rack without using the intermediate isolation transformer, the latter option eliminating the possibility of floating the charge system.

3.3 Charge-Control Rack

For safe and reliable capacitor charging, a charge-control and interface system is needed to connect and disconnect the power supply to the load on demand. This system must protect the power supply during a series of discharges where the load and supply are electrically connected, and it must also permit the safe removal of the energy stored in the capacitors in the event that normal discharge operation is not possible or desired. The components for these functions are housed in a separate rack shown in figures 25 and 27. This rack is located adjacent to the power supply rack. An electrical circuit schematic of the electrical connections between the power supply and the thruster (minus mechanical isolation switches) used for simulation purposes is presented in figure 28. The components of this system are described in this section.

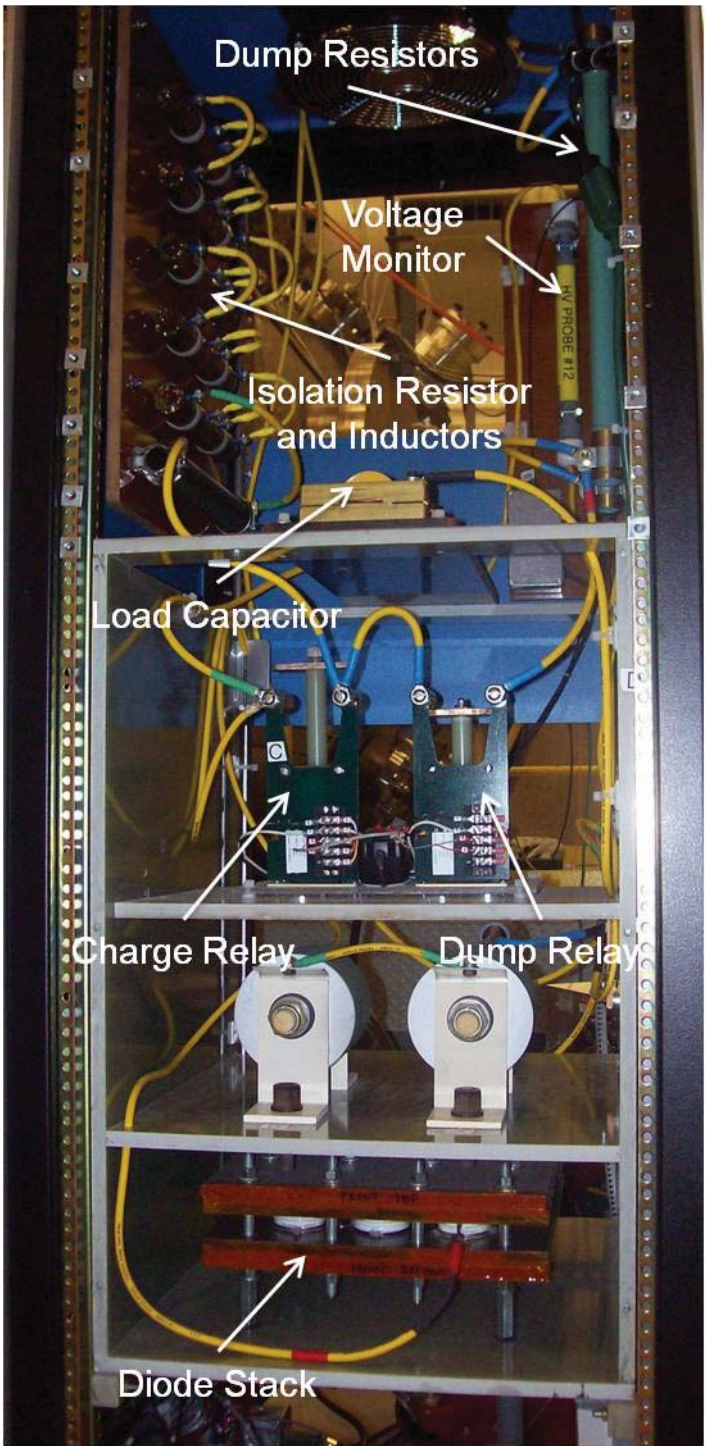

Figure 27. Charge-control rack.

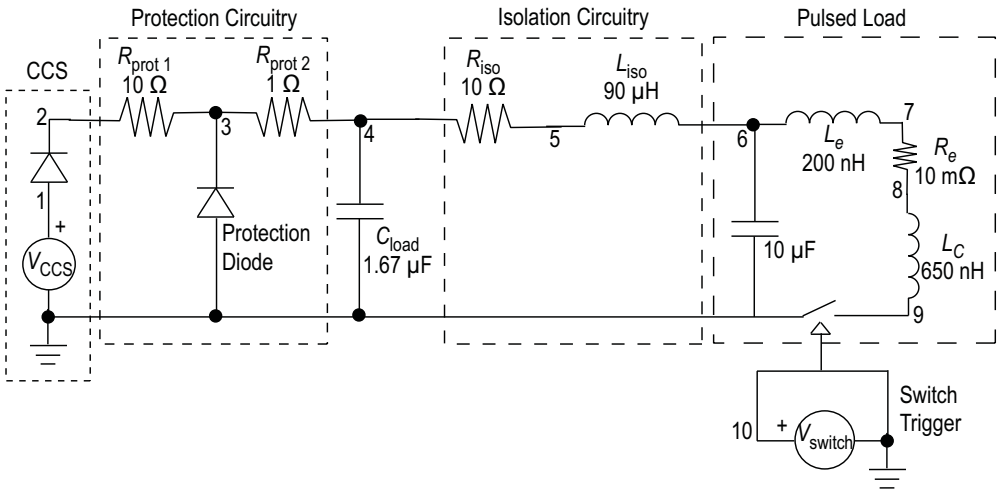

Figure 28. SPICE circuit used in the simulation of the charging system (with node numbers indicated). The switch is programmed to pulse every 50 ms.

3.3.1 Protection Circuitry

To safeguard the power supply from voltage reversals, the manufacturer recommended using circuitry consisting of a high-voltage protection diode stack in parallel with the power supply output power resistors of 10 Ω ($R_{prot\ 1}$) and 1 Ω ($R_{prot\ 2}$) in series with the output.[25,28] If a voltage reversal should occur at the load, the reversed current flows through the diode stack rather than the supply. The diode stack consists of nine International Rectifier SD553C45S50L fast recovery diodes (FRDs) connected in series. The voltage rating of these diodes is 4.5 kV for a total maximum voltage rating of 40.5 kV. The maximum forward current for each diode is 560 A. Each diode has a 1-MΩ resistor connected in parallel to uniformly grade the voltage across the entire diode stack.

3.3.2 Output Capacitor

As a capacitive load is required at all times for stable operation, a 1.67-µF capacitor (C_{load}), (which consists of three 5 µF–4 kV capacitors connected in series) was installed in parallel with the diode stack at the output of the supply. Note that the 'output capacitor' is a permanent fixture in the charge-control rack and is distinct from the capacitor bank load to be charged. The voltage rating on the present output capacitors have a voltage rating that will permit operation of the supply up to 8 kV while maintaining adequate margin for voltage reversals. The output capacitors have a 30 MΩ bleed resistor across the unit (10 MΩ across each capacitor) to ensure the capacitors are discharged when not in use. For higher voltage operation (higher than 8 kV), the output capacitor should be replaced with capacitors that have a higher voltage rating.

3.3.3 Isolation Circuitry

The isolation circuitry is used to further protect the power supply from transients during repetition-rated operation, serving to significantly reduce the current to which the protection diode

stack could be exposed. A high-power 10 Ω (±10%) resistor (manufactured by Kanthal) is used for the series isolation resistance (R_{iso}). The resistor is rated for a peak voltage of 75 kV, an average power of 150 W, and a single-shot energy limit of 75 kJ. This resistor is capable of handling the dissipated power at the low charge rates explored in this TP, however, for higher charge rates (higher charge voltages and current levels), forced air cooling of the resistor may be required. Five high-power 18 μH inductive chokes (manufactured by Ohmite) are used for the series isolation inductance (L_{iso}). The insulation on these inductors was damaged in places, so they were painted with two coats of Viking high-voltage insulation varnish and then covered with a layer of Kapton® tape to prevent arcing.

3.3.4 Mechanical Switches

The power supply output is switched to the load through a Ross relay (rated for operation up to 40 kV) configured in the normally open position. In repetition-rated operation, this 'charge relay' is energized closed to keep the supply and load connected. After operation, the load and supply are disconnected by opening the charge relay. Any energy remaining in the capacitor bank after the charge relay is open is shunted to ground through a resistive load consisting of two high-power resistors in parallel (total resistance of 4.3 kΩ). The connection to ground through the resistors is completed through another Ross relay. This relay is called the 'dump relay,' and is configured in a normally closed position such that it must be energized open during repetition-rate operation. Two resistors are used for redundancy in case one fails. Each resistor is capable of dissipating up to 10 kJ per pulse. For higher energy capacitor banks, a water resistor is also available. Both the charge and dump relays are fiber optically controlled from the control system. The locations of these relays in the charging circuit are shown in figure 26.

3.3.5 Voltage Monitor

A fiber optic coupled voltage monitor is used to remotely measure the power supply voltage. This monitor is a 10,000:1 voltage divider installed across the output capacitor (C_{load}). The sense voltage on the lower leg of the divider is connected to a fiber optic modulator/transmitter link that transmits a frequency modulated light signal (via a POF-type fiber) to a receiver/demodulator in the control system. The frequency modulation on the data makes it less sensitive to drift and noise. The demodulated signal may be read into a digitizer for display by LabVIEW™ or it may be directly measured using a handheld voltmeter or oscilloscope. The voltage monitor was calibrated by applying voltages in the range of 0 to 8 kV to the output capacitor and measuring the voltage at the receiver/demodulator ($V_{FO\ Rx}$). Using this calibration, the scaled bank voltage is given by

$$V_{\text{bank}} = a + b\,V_{FO\ Rx}\ , \tag{25}$$

where

$a = 73 \pm 4$ V
$b = 9{,}430 \pm 20$.

3.3.6 Interlock System and Ground Isolation

A safety interlock circuit for the power supply consists of an interlock control box with a latching enable switch, an 'interlock engaged' switch, and an E-stop button at the operator's station. In addition, there is a remote E-stop button on the platform adjacent to the vacuum facility. The interlock loop may be expanded with more E-stop buttons as needed. When the interlock condition is met, steady-state light is transmitted on two separate fibers (POF-type). One fiber is routed to the charge-control rack while the other goes to the test control system.

The interlock function of the charge-control rack is fiber optically controlled and centralized in a panel at the bottom of the charge-control rack, seen in figure 29. When the fiber optic signal from the interlock loop is received, power is enabled to both the charge and dump relays, and only then is actuation of the relays possible. Power is also enabled to a separate relay which closes the interlock circuits of the individual CCS power supplies. In the event that the interlock loop is interrupted, either when one of the E-stop buttons is pressed or if power to the building is lost, the charge relay will open, the dump relay will close, and the power supplies will be disabled.

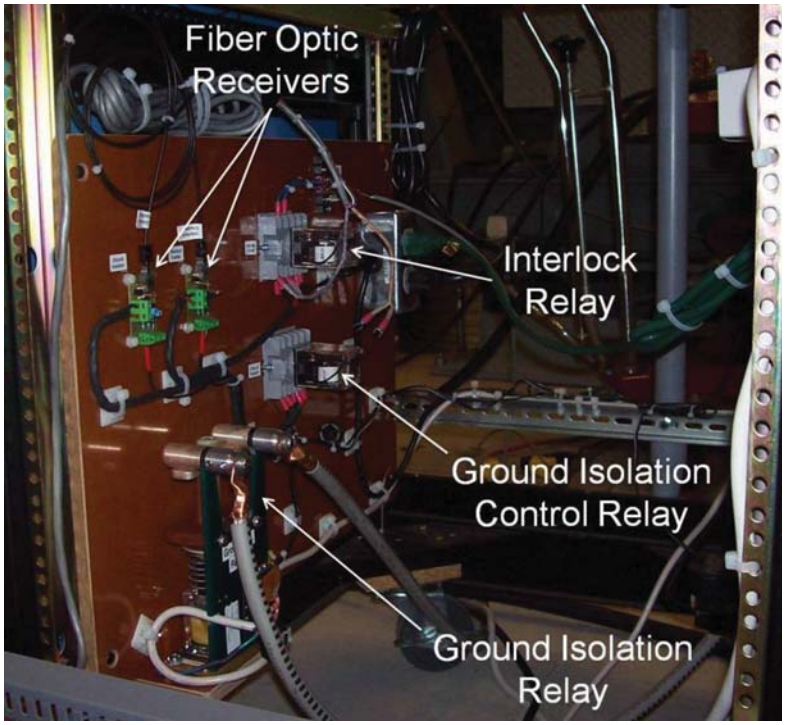

Figure 29. Charge-control interlock panel showing fiber optic receivers, interlock relays, ground isolation relay, and grounding cable.

The charge-control rack and the power supply rack operate on separate electrical service. An isolation transformer for the charge-control rack is available if it is ever necessary to float the charge system. The building ground is typically connected to the chassis ground of the charge-control rack (and to the power supply rack through that connection as well) with 00-gauge cable

wired to a high-voltage, normally closed Ross relay. This ground isolation relay is controlled by a fiber optic cable from the test control system and is provided to permit floating of the system. This relay is not interlocked, so the system can be kept floating even if the interlock function has been activated.

3.3.7 Repetition-Rated Operation Design Considerations and Thruster Modeling

Prior to this program, the CCS power supply had only been used to charge a capacitor bank for single-pulse operation. Continuous, repetition-rated operation presents complications not experienced during single-pulse operation. Specifically, during single-pulse trials, a mechanical switch can be opened to electrically isolate the supply from the pulsed discharge. During repetitive pulsing, mechanical isolation switches are not fast enough to open and close to permit recharging between pulses, so the pulsed load and supply remain electrically connected during the discharge. This has the potential to expose the power supply output to the ringing voltage on the capacitor bank as it is discharged, which could be destructive to the supply if it is not properly protected.

The thruster and power supply protection circuit were modeled using Intusoft's ICAPS Simulation Program with Integrated Circuit Emphasis (SPICE) electrical circuit simulation software to determine the likelihood and magnitude of the voltage reversal problem and explore avenues to minimize the voltage appearing at the power supply output. The circuit schematic for this simulation is shown in figure 28. The power supply is modeled as a constant voltage source with a generic diode at the positive output terminal to serve as a substitute for the internal high-voltage rectification diodes. The thruster is modeled as a simple inductive-resistive-capacitive (LRC) circuit. While the values of the thruster inductance, resistance, and capacitance correspond to a particular thruster (specifically the flat-plate IPPT of sec. 4), the resulting discharge characteristics are sufficiently general for the purposes of this design exercise. The thruster is modeled with a capacitance of 10 μF, a coil inductance of 650 nH, a stray inductance of 200 nH, and a series resistance of 10 mΩ. A generic soft-switch model is used to represent either a spark gap or a thyristor, which discharges the capacitor bank through the inductive coil. The switch is programmed to close every 50 ms (repetition-rate of 20 Hz), with the entire simulation lasting for 500 ms. The capacitor in the thruster circuit discharges with every switch closing, and once the bank is discharged, the power supply recharges it. The resulting voltage output is a sawtooth waveform.

Without any other circuitry between the power supply and the thruster (i.e., no 'isolation circuitry'), the model predicted a large ringing voltage at the power supply output, as well as a large unipolar current through the protection diodes in excess of 500 A, close to their rated current limit. This gave rise to the additional isolation circuitry consisting of a series resistance of 10 Ω and a series inductance of 90 μH between the power supply output and the load.

The results of the SPICE simulation are shown in figure 30, with the view expanded to show the waveforms that result from one discharge of the thruster circuit at $t = 50$ ms. The charge voltage in this case is 4 kV. The voltage at the thruster capacitor (node 6) rings, while the isolation circuitry keeps the voltage from ringing at the load capacitor (node 4) and causes the value of the voltage to quickly drop to 0. The peak current in the thruster circuit is just over 12 kA, but the current in the protection diode stack is no more than 70 A, which is well below the rated limit.

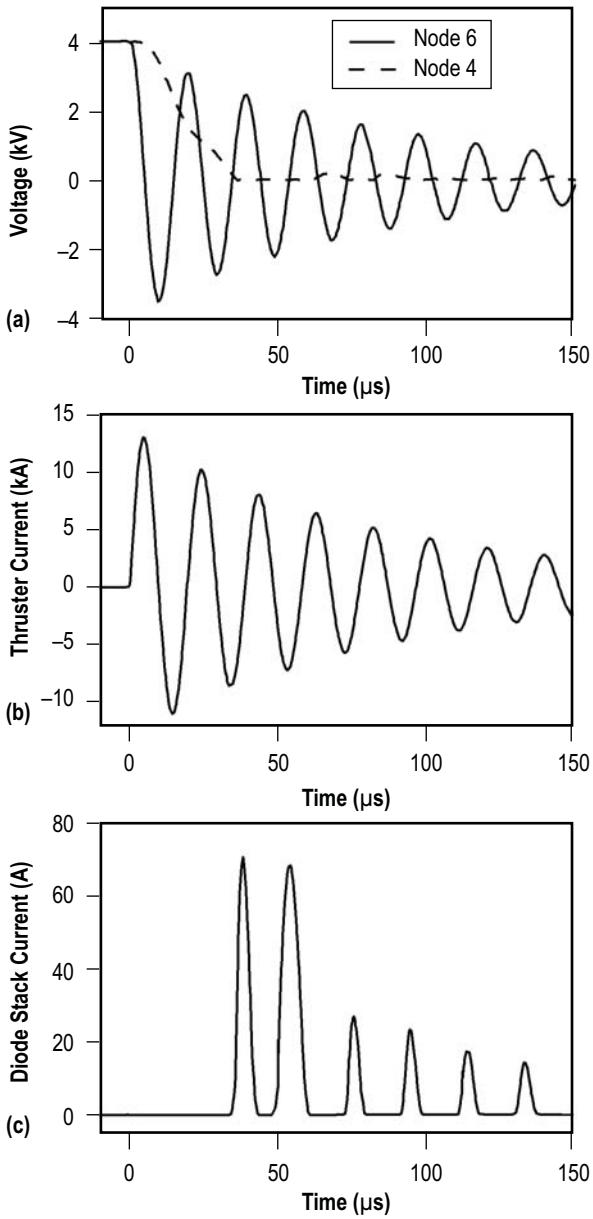

Figure 30. Outputs from the SPICE model showing (a) the voltage at nodes 4 and 6 (as indicated in fig. 28), (b) the current in the thruster circuit, and (c) the current in the protection diodes.

The SPICE simulation indicates that for a 4-kV charge voltage, inclusion of a series resistance and inductance can adequately isolate the protection diodes and the power supply with minimal impact on the performance of the charge system. The 10-Ω resistors will only dissipate 10 to 500 W over the entire operating range of the charge system, representing a small fraction of the overall power delivered to the load by the CCS. It should be noted that for much higher voltages, or very different load characteristics, it would be wise to perform additional SPICE simulations to ensure that current in the protection diodes does not exceed the specifications.

3.4 Testing of the System

The fast-charge system was tested in repetition-rated mode with the CTP IPPTs described in section 2 of this TP. Problems were encountered with the remote control of the CCS. Subsequent investigation has shown that the power supplies themselves are operating properly, indicating a potential failure in the FIB.

To expedite testing, an older CCDS model with manual front panel controls was employed. Other than the front panel, the CCDS model is the same as the CCS. The voltage level was adjusted manually, but it was enabled remotely using a dedicated internally fabricated controller that interfaced to the supply through the back panel connector. A voltage trace of the capacitor bank voltage during a repetition-rated test of the thruster is shown in figure 31(a). The charge system performed as desired, recharging the thruster capacitor bank after every discharge. The internally fabricated controller was also used to control one of the CCS, verifying that they were operating properly and that remote control was possible. An LGDT waveform from a test with the 38° CTP IPPT (described in sec. 2) is displayed in figure 31(b) for operation at 5 Hz for 5 s. During pulsed operation, the thrust stand oscillates about a displaced position, with the difference between the displaced neutral position and 0 corresponding to the average thrust imparted by the thruster.[19]

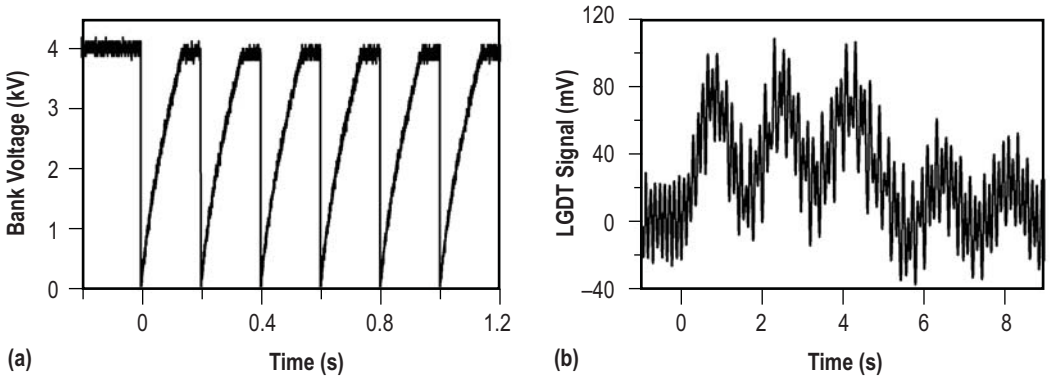

Figure 31. Test of the 38° CTP IPPT, 5-Hz, 5-s repetition-rated: (a) Voltage waveform and (b) LGDT signal.

The average thrust as a function of mass flow rate for 5-Hz operation of the 38° CTP IPPT is presented in figure 32 for three separate capacitor charge voltages. During repetition-rate testing, there were issues with the high-voltage insulation on the charge and pulse lines short-circuiting at 5 kV. The trend in these data, specifically the 4-kV charge data, shows an increasing level of thrust as a function of mass flow rate, mirroring the single-pulse data presented in figure 14. The authors compare the single 5-kV data point in figure 32 with the corresponding data point in figure 14, observing that the average thrust operating in repetition-rate mode is greater than simply calculating five times the single-shot impulse bit. This suggests better gas acceleration in the pulsed mode, but the exact mechanism for this improvement remains an open question for future study.

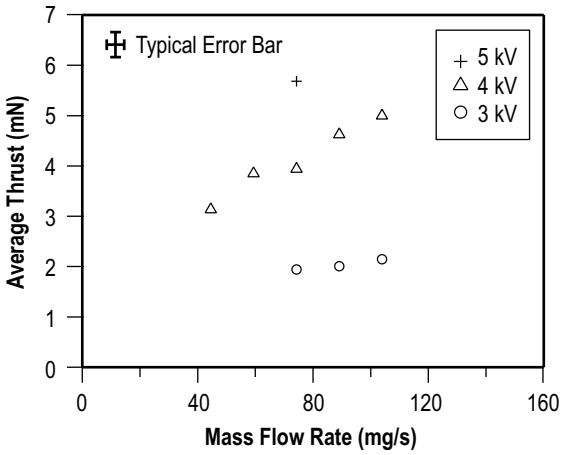

Figure 32. Average thrust as a function of continuous mass flow rate for a 5-Hz, 5-s repetition-rated test of the 38° CTP IPPT operating on argon.

4. FLAT-PLATE THRUSTER WITH PULSED GAS INJECTION

Apart from the data reported in the previous section, all testing of IPPTs has been performed in single-discharge (single-shot) mode, while no testing has been performed in the repetitive operation mode that an actual thruster would use. Testing of IPPTs has also not been performed using solid-state switching components, with almost all development to date, including the current IPPT state-of-the-art PIT MkV/MkVa, using triggered spark gaps to discharge capacitors through the acceleration coil.[2] Although it was recognized that a practical thruster would require solid-state switches, the requisite performance and reliability in such switches did not exist at the time. Within the last decade, high-power, solid-state switches (thyristors and insulated-gate biopolar transistors) that meet the requirements of an IPPT have become available, their development driven mostly by the needs of the power and rail industries. Such switches have been used most notably in the small-scale development testing for later generations of the PIT, again with all testing performed in single-discharge mode.[29] The apparatus described in this section was aimed at integrating into an IPPT the capability of repetitive (multiple-discharge or repetition-rate) operation switched using solid-state components with propellant injected using a PGV, integrating all these aspects into a single thruster for the first time. At the time of this TP's publication, a fully integrated version of this thruster has not yet been tested.

4.1 Design Considerations

To meet the goals described above, an IPPT was designed that would permit thrust stand testing of a repetitively operated, solid-state switched thruster with relatively little investment in time and expense. The design target for the thruster is a jet power (P_{jet}) in the range of 2 to 5 kW, with I_{sp} in the range of 3,000 to 6,000 s. The target conditions are in the range of those that would be required for certain missions,[30] while at the same time, a thruster operating at these conditions could be feasibly tested in the 2.75-m- (9-ft-) diameter electric propulsion vacuum testing facility at MSFC. Although only quasi-steady-state testing is planned for the immediate future, the design could permit the eventual evolution to continuous testing. The mass flow rate for the target parameter range is 1 to 10 mg/s, which corresponds to throughputs of 53–533 Pa-L/s (0.4–4 torr-L/s) for argon, or 133–1,330 Pa-L/s (1–10 torr-L/s) for ammonia. The maximum throughput of the vacuum facility operating on diffusion pumps is roughly 2,670 Pa-L/s (20 torr-L/s), implying that steady-state operation should be possible without an unacceptable increase in the chamber base pressure. For condensable propellants, such as ammonia, a cold-wall inside the chamber could further improve the throughput for long-duration, steady-state testing.

A flat-plate coil design, as used with the PIT and later in the Faraday Accelerator with Radio-Frequency Assisted Discharge (FARAD), was selected for ease of fabrication.[2,4,5] As was the case in FARAD, the coil leads are connected in parallel and driven with a single capacitor bank and switch. The structural components are primarily Lexan, phenolic, and fiberglass rod. These materials could not necessarily be used in a flight unit or for a long-duration, ground test article where thermal

management of the device during continuous operation is an important consideration. In those cases, refractory materials such as alumina or boron-nitride would be required for many of the key components. For quasi-steady operation, however, brief bursts of up to 100 pulses should be possible without significant heating affecting the structure. A partial assembly of the thruster, as it stands at the writing of this TP, is shown in figure 33.

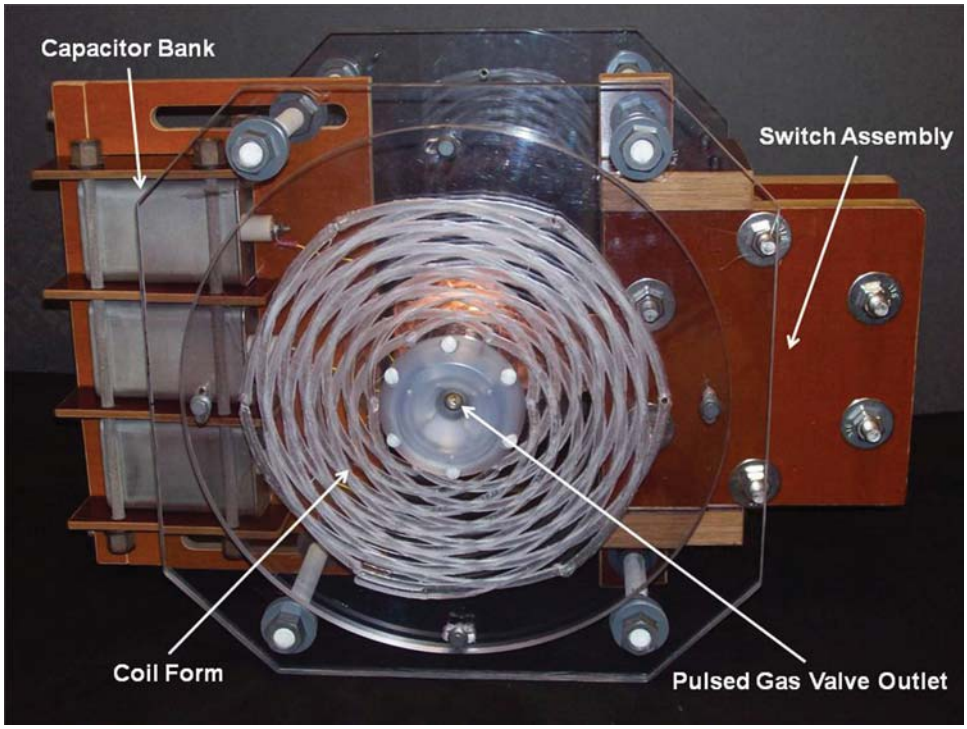

Figure 33. Front view of coil form showing the Archimedes spiral-shaped grooves in which the leads lie. The coil form is fabricated from a Lexan sheet 1.3 cm (0.5 in) thick and has an outer diameter of 35.5 cm (14 in).

4.2 Design, Fabrication, and Assembly

The thruster consists of five major components: the acceleration coil, capacitor bank, switch assembly, preionizer, and the PGV/propellant delivery system. All five subassemblies are mounted on a structural frame consisting of two 1.3-cm- (0.5-in-) thick Lexan plates, adjoined by four 1.6-cm- (0.625-in-) diameter fiberglass threaded rods. The major components are modular and can be easily removed from the frame to implement any repairs, modifications, or later upgrades to the thruster.

4.2.1 Acceleration Coil

The coil consists of six leads in parallel, wound on the Lexan coil form. Each lead begins on the front side of the coil form at an inner radius (r_{in}) of 5 cm and spirals out in one complete turn (2π radians) to an outer radius (r_{out}) of 15 cm. Each lead passes through a hole in the coil form,

emerging on the opposite side to spiral back inwards on the back side in the same sense as the top windings, completing another full turn before returning to the starting angular and radial position. The starting and ending points of the six leads are arranged around the coil form at 60° intervals. The formula for the path of each lead is that of an Archimedes spiral, given for θ in radians as

$$r = r_{\text{in}} + \frac{\left(r_{\text{out}} - r_{\text{in}}\right)}{2\pi}\theta \quad . \tag{26}$$

The leads consist of copper wires, laid in grooves that are machined in the coil form. An illustration of the coil form showing the multiple offset Archimedes spiral paths is shown in figure 34.

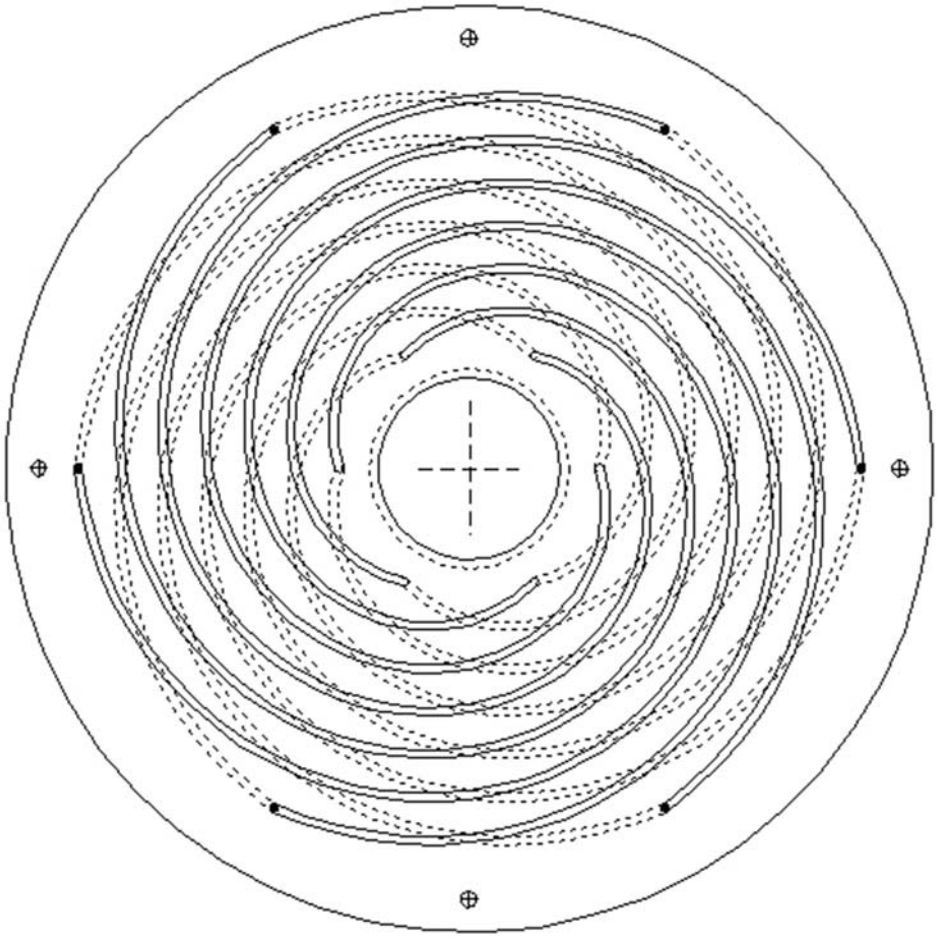

Figure 34. Front view of coil form showing the Archimedes spiral-shaped grooves in which the leads lie. The grooves on the front of the form are shown with solid lines and the back side grooves are shown with dotted lines. The dark circles at the outer radius where the two meet are transitions from the front side of the form to the back side.

The inductance of the coil was calculated using QuickField™, a two-dimensional axisymmetric magnetic field solver. Although the coil is not axisymmetric, it is possible to model it in this manner if the azimuthal current density over the face of the coil is approximately uniform. This condition is met with the six-lead configuration of the present thruster. The six two-turn leads are modeled as twelve one-turn leads, the location of each can be visualized if a cross-sectional radial cut is taken across the coil face and a circular conductor is placed at every location in the *r*-*z* plane where the cut intersects the coil. Front and back leads are paired in series as shown in figure 35(a) just as the leads intersecting the cut-plane would be paired, yielding six coil pairs that all have comparable self-inductances.

An annular disc-shaped slug, 5 mm thick and with a resistivity of 4×10^{-8} Ω-m (equal to that of 6061 aluminum), represents the plasma in the QuickField model. When the plasma is near the coil, it acts to exclude magnetic flux, lowering the effective inductance (L_{eff}) of the coil as measured at the terminals (where all six parallel coil sets converge to single conducting entrance and exit points). The magnetic field was calculated using the AC-magnetics mode of QuickField. A voltage oscillating at a frequency of 50 kHz was applied to the coil pairs to approximate the discharge frequency at which the thruster would operate. The model is shown in figure 35(a), and the resulting flux contours from one such calculation are shown in figure 35(b).

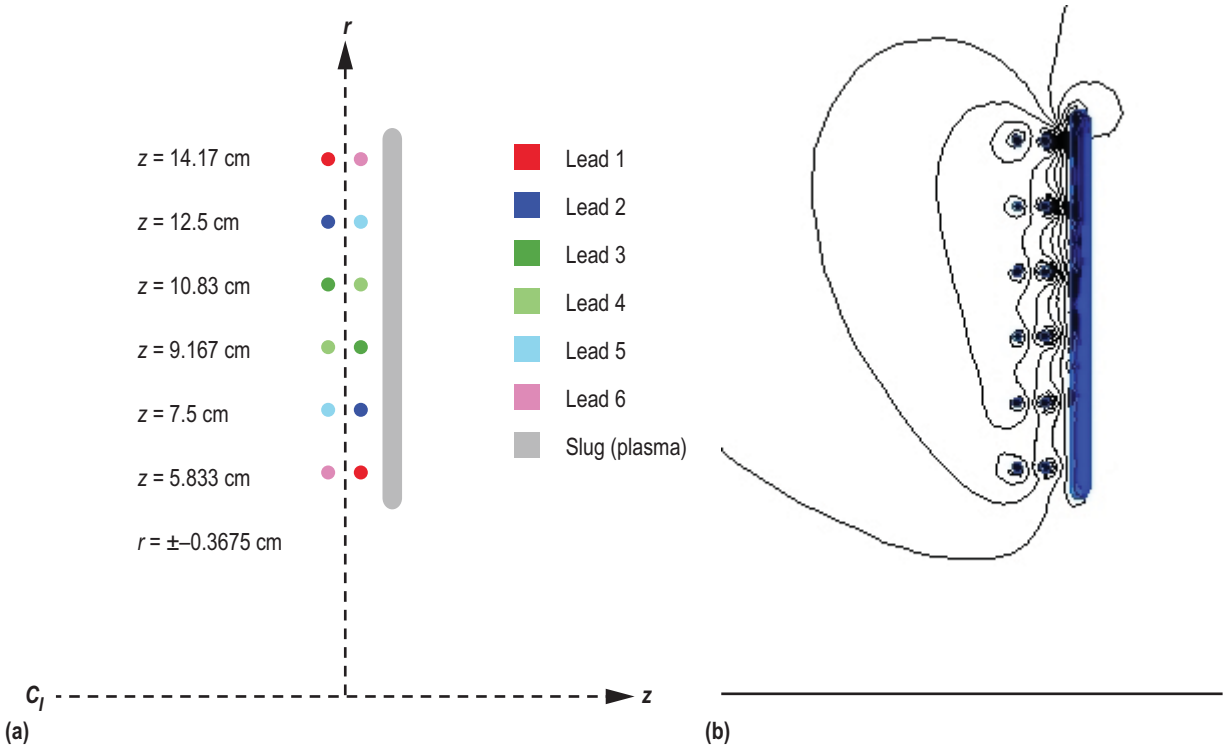

Figure 35. QuickField model of (a) coil arrangement for QuickField calculation and (b) calculated flux contours for one particular location of the slug (plasma).

The resulting currents, magnetic fields, and magnetic field energies were calculated over the entire domain. From these data, the value of L_{eff} was calculated using the formula for magnetic field energy:

$$W_B = \frac{L_{eff} I_{\text{tot}}^2}{2} \quad , \tag{27}$$

where I_{tot} is the total current in all six sets of leads. The slug was advanced in axial position z away from the coil face, and L_{eff} was calculated at every step to yield the data shown in figure 36.

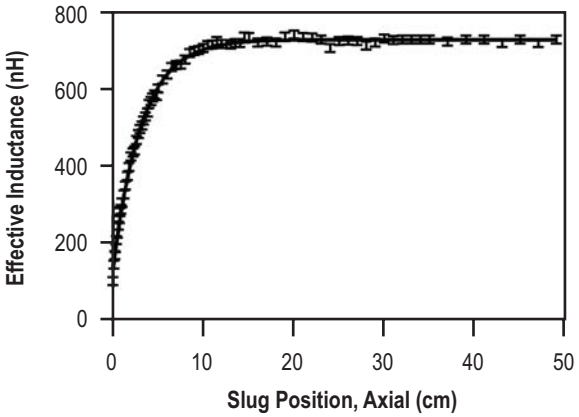

Figure 36. L_{eff} as a function of z as calculated with QuickField, with a calculated uncertainty of ±10 nH. The solid curve is a fit to the results of the calculation performed using equation (28).

These QuickField results were then fit with a curve of the form

$$L_{eff} = L_C \left[1 - k_0^2 \exp\left(-\frac{2z}{z_0} \right) \right] \quad , \tag{28}$$

where

L_C = self-inductance of the coil
k_0 = coupling coefficient
z_0 = electromagnetic decoupling distance for the coil, also known as the electromagnetic stroke length.

The uncertainty on L_{eff} was taken to be ±10 nH (based upon the criteria for solution 'convergence' in the analysis program). The fit parameters for the curve plotted with the data in figure 36 are $L_C = 729$ (±2) nH, $k_0 = 0.903$ (±0.003), and $z_0 = 6.3$ (±0.1) cm. The goodness of the fit is given by the reduced χ^2 error, defined as χ^2/ν, where χ^2 has its usual definition from curve-fitting statistics. For the term $\nu = N - p - 1$, N is equal to the number of points (78), and p is the number of fit parameters (3). For the curve fit of L_{eff}, the value of χ^2/ν was 0.66, which is less than unity indicating a good fit.

In fabricating the coil, it is imperative that the coil leads be well insulated so that they do not electrically short when the high-voltage pulse is applied to the thruster. As the top and bottom windings need to be close to one another to minimize stray inductance, the coil form must be fabricated from a material with good insulating properties and a high voltage holdoff. The coil form consists of a 1.3-cm- (0.5-in-) thick disk of optical-grade (transparent) Lexan with an outer diameter of 35.5 cm (14 in) and an inner diameter of 7 cm (2.75 in), which not only has good insulating properties, but is also mechanically strong and readily machinable. Channels for the coil leads possessing a 4.75-mm (0.1875-in) square cross section were machined into the form using a Sherline 2000 tabletop CNC milling machine. The walls and floors of the channels will be painted with Viking high-voltage insulation varnish to fill and/or cover any microcracks that may have been produced during machining. The coil leads consist of No. 10 enamel-coated magnet wire. Once the coil is wound in the grooves, the channels will be filled with RTV-560 (a high-voltage, vacuum-compatible, silicone insulating compound supplied by Momentive Inc.) for additional electrical insulation.

The current feed for the coil consists of two coaxial cylindrical bus-plates, fabricated from a 1.02-mm- (40-mil-) thick, alloy 110 copper sheet. The cylindrical plates are separated by a Lexan tube with an outer diameter of 7.6 cm (3 in) and a wall thickness of 3.2 mm (0.125 in), which is glued to the coil form. The bus plates are three times thicker than the skin-depth in copper at a frequency of 50 kHz to minimize the additional resistance they add to the circuit. Both cylinders have an approximately 6.4-mm (0.25-in) azimuthal gap to prevent eddy currents from being induced by the discharge flowing through the coil. The connection to the coil leads will be made by soldering them to the plates. The cylinder surfaces are insulated with Kapton tape while the ends are insulated with high-voltage, vacuum-compatible RTV silicone (RTV-560, supplied by Momentive Inc.). Copper tabs (110 alloy, 1.02-mm- (40-mil-) thick) are soldered to the current feed at the end opposite the coil, and these are insulated from one another with a 1.3-cm- (0.5-in-) thick Lexan sheet possessing an outer diameter of 17.8 cm (7 in). The bus plates that connect the switch assembly and capacitor bank (discussed later) to the coil assembly are held against the copper tabs on the cylindrical copper current feeds with Lexan clamps. The coil assembly and cylindrical copper current feeds are shown with one of the Lexan clamps in figure 37. The entire coil assembly can be removed from the thruster as a unit.

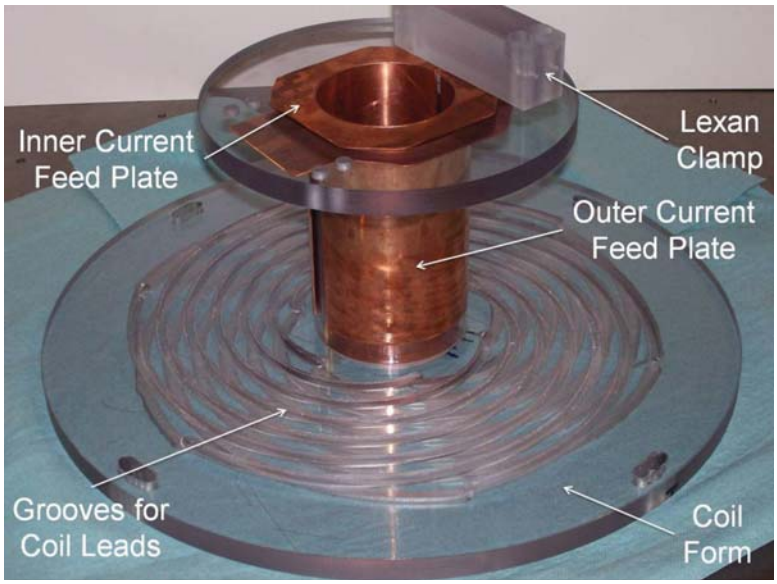

Figure 37. Coil assembly (partially assembled), showing the coil form (without leads), coaxial current feed plates, and one of the Lexan clamps.

4.2.2 Capacitor Bank

The capacitors used to store the energy for each discharge were obtained from CSI Capacitors. They are vacuum-compatible, oil-filled metal cans each possessing a capacitance of 10 μF. The maximum charge voltage for these capacitors is 7.5 kV, while the series inductance is not more than 20 nH. The terminations are side-by-side terminals of No. 8 threaded rod, insulated from the capacitor body using ceramic standoffs. Flexibility was desired in the thruster's parameters, so the bank was designed to use from one to three capacitors, making it possible to test at 10, 20, or 30 μF. Up to three capacitors can be simultaneously mounted on a frame, fabricated from LE-grade and XX-grade phenolic, which is held stationary to one side of the thruster using threaded rods.

4.2.3 Switch

The capacitor bank is discharged through the coil using a PT85QWx45 pulse power thyristor switch manufactured by Dynex™. It is configured in a flat 'hockey puck' package and has the following properties: maximum holdoff voltage of 4.5 kV, RMS current of 1,225 A, surge (nonrepetitive) current of 30 kA, and maximum dI/dt of 22 kA/μs. The thruster circuit was designed so that the initial current rise rate would stay below the dt/dl limit of the switch. Ideally, the current would be shut off at the first zero-crossing of the current (after the first half-cycle of the discharge). This can be accomplished with an FRD. The FRD recommended for the thyristor used in the thruster is the DSF21545SV (also manufactured by Dynex), which has a maximum current rating of 20 kA. Although this is the fastest FRD that could be obtained and that could handle the requisite current, its recovery time of 7 μs may still be too slow for the purpose of interrupting the discharge after the first half-cycle. However, since this is an unknown, it was deemed worthwhile to test the FRD

to quantify its performance in the thruster. The switch and diode together will be referred to as the 'switch-stack.'

The electrical connections to the switch are completed using copper tabs. For proper operation, the switch-stack must be sandwiched between these tabs with a force of 40 kN (about 9,000 lb) within ±10%. This is accomplished using a mounting yoke fabricated from two 2.6-cm- (1-in-) thick, CE-grade phenolic slabs. The switch-stack, taken together with the copper tabs and the yoke, are referred to as the 'switch assembly.' G-10 would have been preferable for the yoke, as it is stronger, however, phenolic was chosen as it is easier to machine. The compressive force is provided by several bolts azimuthally spaced around the circumference of the switch-stack and loaded in tension that squeeze the assembly. The slabs deform somewhat under load, and the resulting crowning would lead to a nonuniform pressure applied to the switch and diode. To counteract this, 1.3-cm- (0.5-in-) thick stainless steel disks are inset into the slabs so as to distribute the compressive force applied to the switch-stack. The slabs are held together and compressed with six 5.5-in-long, 1/2-13 stainless steel bolts encased in phenolic tubes for electrical insulation. The bolts are locked down with Bellville washers that are each compressed to a flat-load of roughly 6.6 kN (1,500 lb) so the six bolts can provide the required 40 kN (9,000 lb) of compressive force. A side view of the switch assembly is shown in figure 38.

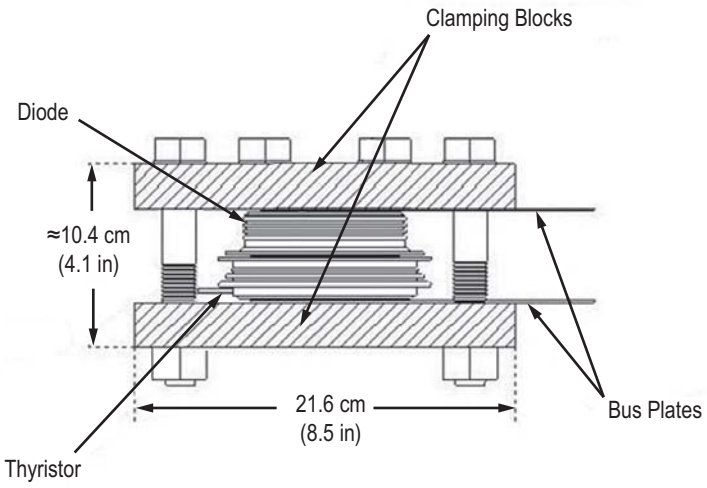

Figure 38. Side view of the switch assembly.

Initially, so as to mitigate any potential for electrical shorting across the switch-stack and to minimize the structural mass, the authors contemplated using strong high-temperature plastic Torlon® or glass-filled Ultem® bolts. While potentially useful in follow-on work, these items were cost-prohibitive for this particular project. Instead, the authors attempted to compress the switch-stack using glass-filled 3/4-11 polyurethane bolts. The torque-yield curve for these bolts had to be determined empirically, as no data were available. Testing showed that they could provide the requisite force; however, once under tension they would yield, relieving the compressive force by as much as 30% over time. This was deemed unacceptable, and the polyurethane bolts were rejected in favor of the 1/2-13 stainless steel bolts used in the final assembly.

Connections between the coil assembly, switch assembly, and capacitor bank are completed by compressing the bus-plates together with Lexan clamps. Where bus-plates join, the copper will be silvered with Cool-Amp paste. Silver gaskets having a thickness of 0.25 mm (10 mil) are used between the copper tabs of the switch assembly and the switch-stack to lower the contact resistance further. All exposed metal surfaces in the switch assembly will be insulated using RTV-560 where possible and by Kapton tape in all other locations.

The thyristor will be activated using a fiber optic coupled trigger circuit. Such a circuit could be mounted to the thruster inside the vacuum chamber. It would, however, require its own dedicated and isolated low-voltage power supply and would have to be electrically potted to prevent arcing. Since trigger circuit integration into the thruster is not pertinent to the goals of the present test program, it will instead be remotely located immediately outside the vacuum chamber, powered using a battery, and connected to the thyristor using twisted-pair wire.

4.2.4 Preionizer

A DC glow discharge preionizer will be used to provide initial ionization of the propellant gas. A stainless steel cap placed over the propellant outlet, which diverts propellant flow in the radial direction over the coil face, also serves as one electrode of the preionizer system. The other electrode consists of four stainless steel tubes rolled into arc segments and mounted at the outer radius of the coil. A capacitor, charged to a voltage between 1 and 3 kV and possessing an energy at this voltage of a few joules, is connected to the preionizer electrodes. When gas is puffed from the valve and flows over the coil face, it will ionize in the electrode gap, providing a connection between the two electrodes. As the capacitor is discharged, a pulsed glow discharge will be produced, ionizing a fraction of the propellant.

The preionizer circuit, shown in figure 39, is electrically isolated from the coil circuit and is also separated from facility electrical service through an isolation transformer. The capacitor and high-voltage supply for the preionizer will be placed outside of the vacuum chamber so as to minimize high-voltage insulation problems that are not directly germane to the problem under consideration.

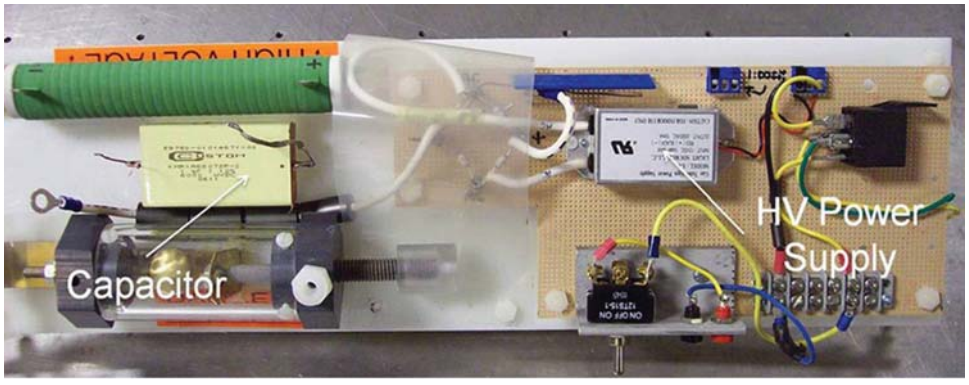

Figure 39. Preionizer circuit, including capacitor and high-voltage supply.

4.2.5 Pulsed Gas Valve/Propellant Delivery System

A fast gas-puff valve, shown in figure 40, is used to inject the propellant in discrete increments. This task requires a valve capable of injecting 100–1,000 μg of propellant, operating at rates of up to 30 Hz. The authors employ the same kind of valve that was developed for the MSFC plasmoid thruster experiment and was later used for the MSFC plasmoid thruster PT-1,[10] specifically a modified Parker Pneutronics valve with a 12-V solenoid coil (model 990-000285-004). The valve was machined to eliminate the dead space downstream of the outlet, and a thin, drawn glass tube was glued into the inlet with Torr Seal® to create a plenum. When the poppet is lifted, the plenum is rapidly exhausted through the outlet, but only slowly replenished through the limiting orifice on the inlet. The valve was soft-soldered to a brass KF-16 flange so that it could be mounted on a test chamber for detailed characterization prior to installation in the thruster. To open the valve quickly, the solenoid is driven with a 320-V pulse. This results in a measured poppet opening time of 300 μs.

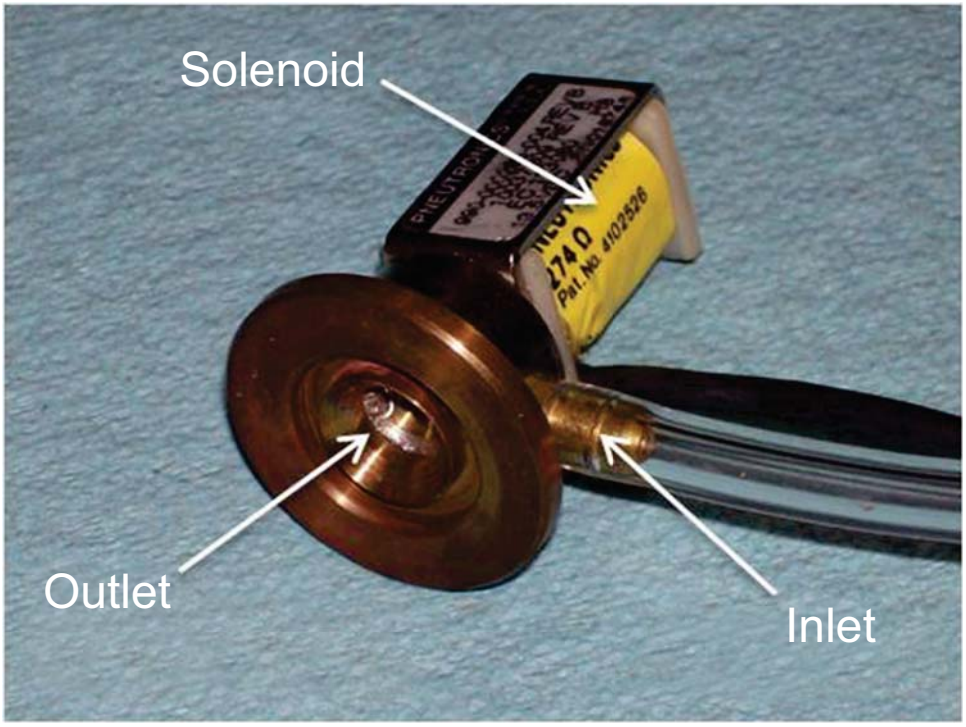

Figure 40. Modified Parker Pneutronics PGV; the flange diameter is 30 mm.

The single-pulse driver circuit previously used for the valve was modified for repetitive-pulse (repetitive-rated) operation (see fig. 41). This circuit is powered from an isolation transformer to electrically insulate it from the facility power and the other subsystems of the thruster.

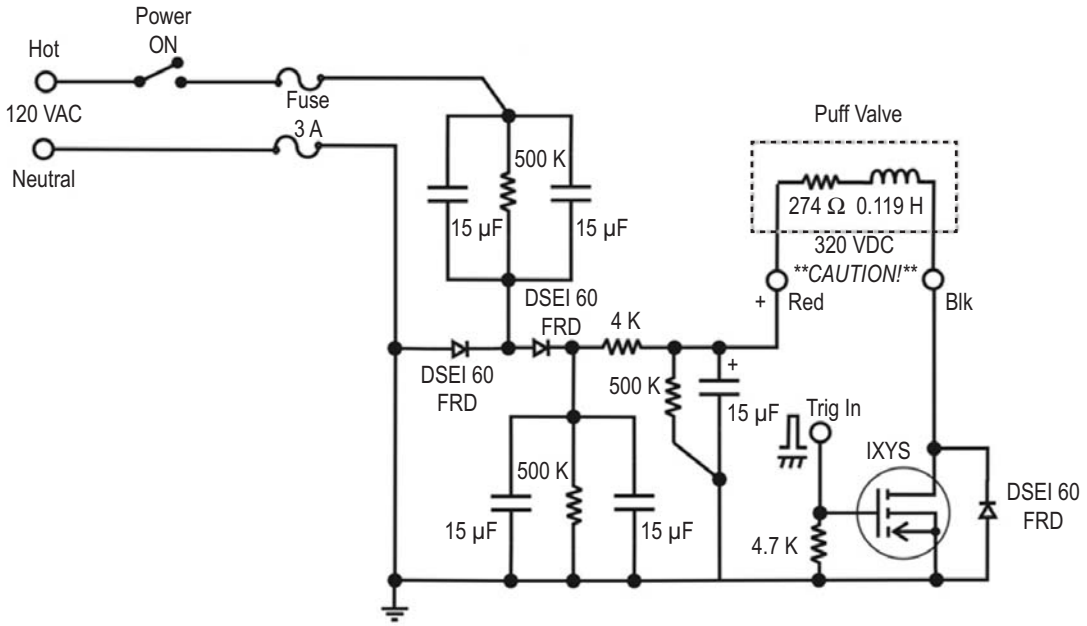

Notes:
1. IXYS is XTK21N100 1,400 V, 15 A HV MOSFET.
2. Trigger in is 9 VDC minimum (12 V nom.).
3. All capacitors rated 450 VAC.
4. 320 VDC drive voltage is lethal–use care!
5. Recommend isolation transformer on AC input.
6. Puff valve is modified Pneutronics 990-000285-004
   13.5 VDC, now obsolete (acquired by Parker).

Figure 41. PGV driver circuit for repetition-rated operation up to 30 Hz.

A control board circuit schematic for the valve-driver is shown in figure 42 and has a fiber optic receiver for plastic optical fiber (POF) and a fast fiber optic transmitter. Upon receipt of the fiber optic command signal, the valve-driver circuit discharges into the solenoid, and the transmitter sends out a pulse that can be used to drive another control system or to directly trigger the thyristor trigger circuit. A picture of the valve-driver with the control board is shown in figure 43.

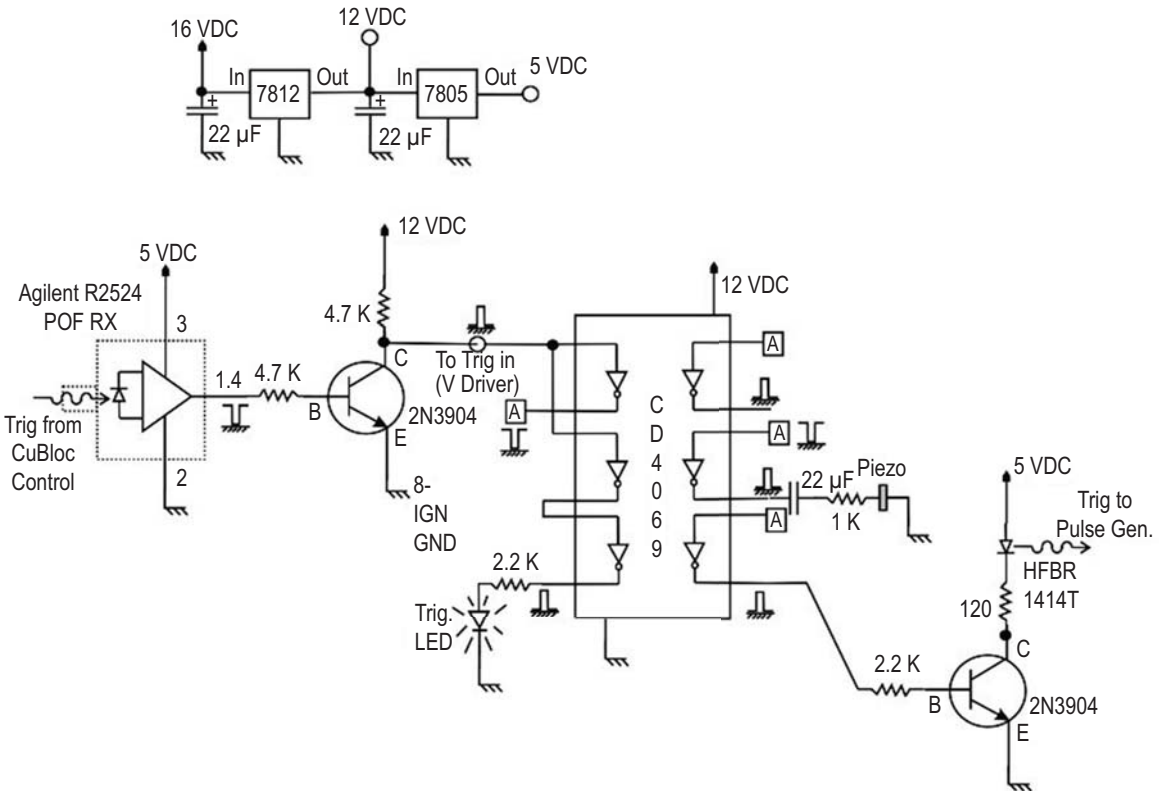

Figure 42. PGV control circuit; a fiber optic output is also provided to drive an external pulse generator or to trigger the thyristor switch.

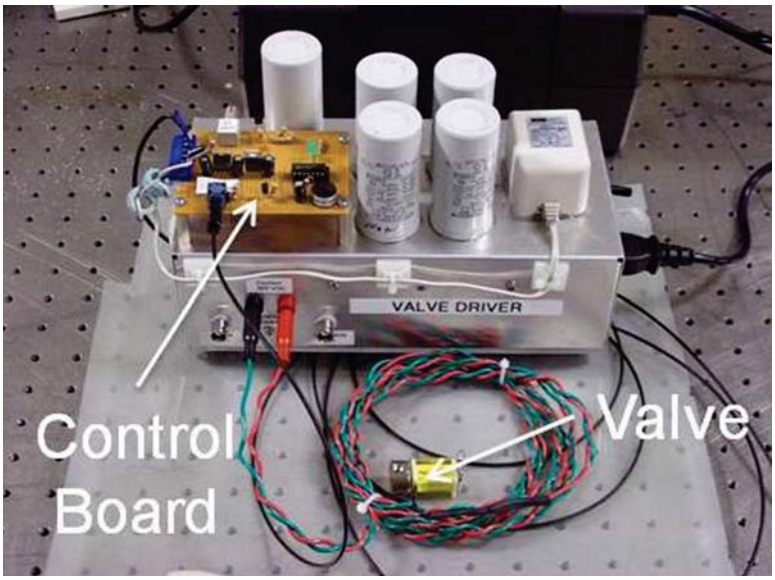

Figure 43. PGV driver with control board and modified Pneutronics valve.

The valve is supplied with gas from a small, self-contained propellant delivery system, which will be mounted directly on the thruster. This will both minimize pressure drops in the propellant line which could hinder replenishment of the plenum and eliminate spurious nonthrust forces that could be exerted on the thrust stand by pressurized propellant lines. The propellant delivery system, shown schematically in figure 44, consists of a small gas reservoir (run-tank), a fill-valve for isolation from the gas supply outside the tank, a regulator for adjusting the pressure of the gas delivered to the PGV, a run-valve that connects the regulated pressure source to the PGV, a transducer for monitoring the pressure upstream of the limiting orifice, and a transducer for measuring the pressure in the run-tank. Also present (not shown in the schematic) is a thermistor for measuring the reservoir temperature. The volume of the run-tank and manifold is approximately 140 cc. The mass flow to the thruster can be determined from the pressure and temperature at the run-tank, which are read by the controller. A picture of the propellant delivery system is shown in figure 45.

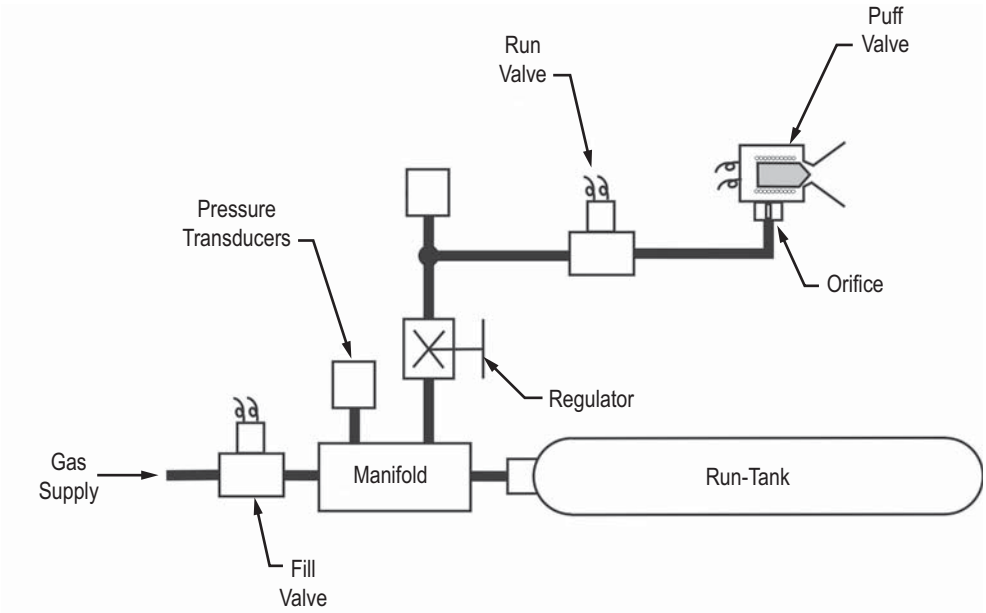

Figure 44. Propellant delivery system.

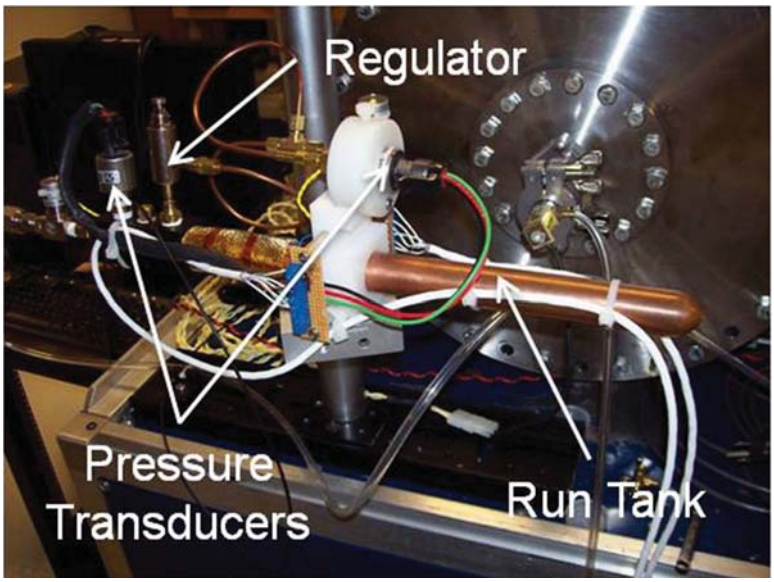

Figure 45. Propellant delivery system with run-tank, regulator, and pressure transducers.

The propellant delivery system and the valve-driver are controlled by a CuBloc single board computer (model Cubase 64T from COMFILE Technology), which is programmed in BASIC. The computer, shown in figure 46, is housed in a Hoffman box for electromagnetic interface shielding and is fitted with a four-line LCD display and manual user controls. It transmits a fiber optic command signal to the valve-driver, controls the fill- and run-valves, and reads and displays the transducer outputs from the propellant delivery system. The controller is programmed with four standard operating modes, each of which are manually selectable. The modes are single-shot and repetition-rated operations at fixed rates of 10, 20, and 30 Hz. The period and duty cycle may also be adjusted for customizable operation. The BASIC program used by the controller is provided in appendix A. The I/O port definitions are recorded in comments to the BASIC code.

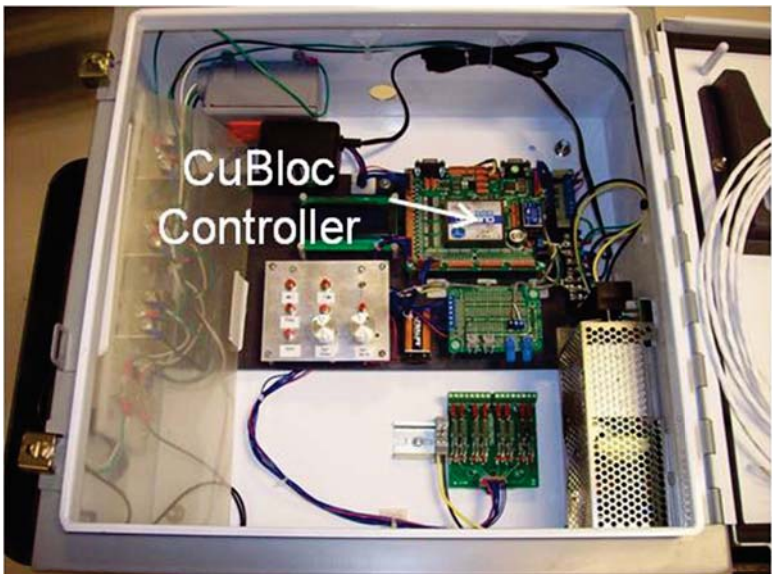

Figure 46. Propellant delivery system controller, using a CuBloc 64T computer.

4.3 Pulsed Gas Valve Testing

A small vacuum chamber, shown in figure 47, was used to characterize the gas pulse output of the fast PGV to be used with the flat-plate IPPT. The valve was mounted at the end of the chamber on a KF flange so any gas injected from the valve would have unimpeded access into the chamber. The volume of the chamber was measured using a calibrated leak (Laco Technologies, model CM225.0-21008), which has a known leak rate at standard conditions of $\Gamma = 4.79 \times 10^{-2}$ atm-cc/s (0.0364 torr-L/s) into vacuum. The accuracy of the leak given in the manufacturer specifications is ±4%. The chamber was evacuated to a base pressure of less than 13 μPa (10^{-7} torr), and air was then admitted back into the chamber through the leak over a period of about 3 hr. The resulting pressure rise was measured with a baratron (capacitance manometer) gauge, measuring over the range of 0 to 1,330 Pa (0 to 10 torr) (gauge not shown in fig. 47). Using the ideal gas law and correcting for temperature and atmospheric pressure (as opposed to standard temperature and pressure), the volume of the chamber was found using the relation $\Gamma = V\, dp/dt$ to be 106 (±5) L. The background leak rate was also measured using the same method and was found to be 7.5×10^{-6} atm-cc/s, which is less than 0.02% of the calibrated leak rate.

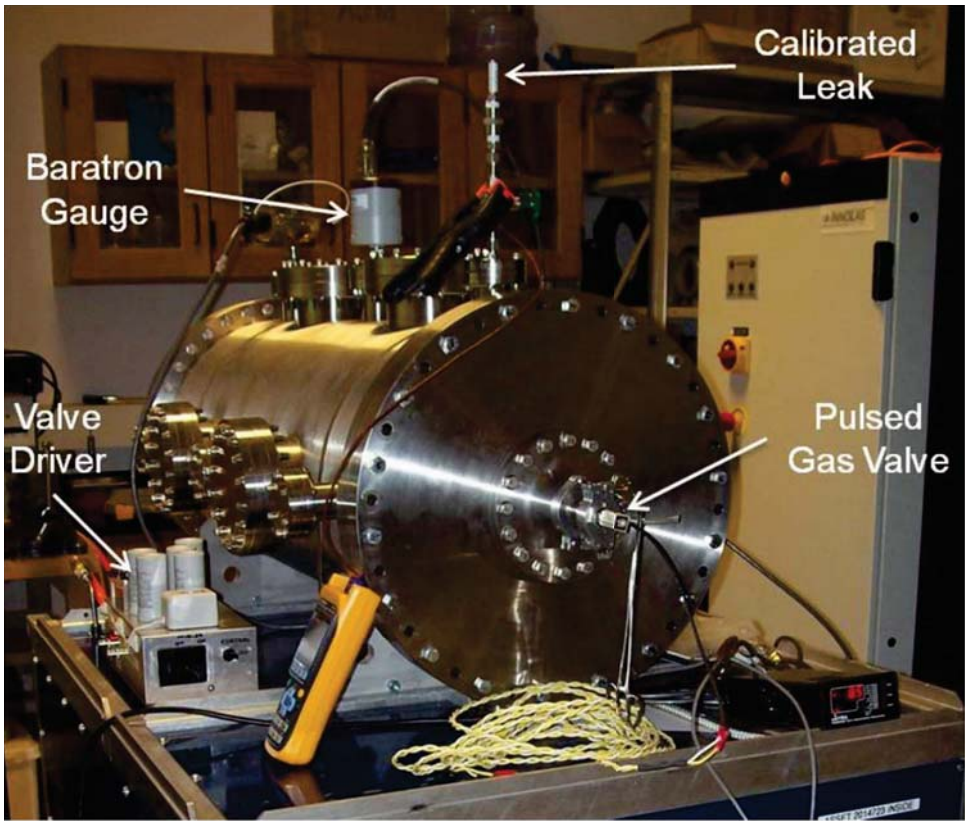

Figure 47. Vacuum chamber with PGV, calibrated leak, and 2-torr Baratron gauge.

With a measure of the chamber volume in hand, the amount of propellant injected by the PGV could be quantified. The valve was operated in single-shot mode, opening a number of times to measure the mass bit (mass per pulse) injected by the PGV. The short interval between each pulse permitted the equilibration of the chamber pressure. For this test, argon gas was used at a line pressure, and therefore, a valve plenum pressure of 157 kPa (22.8 psig). The temperature was measured with a type E thermocouple affixed to the chamber and was found to be 21.8 °C (295 K). The pressure in the chamber was recorded with an MKS model 626 baratron gauge having a range of 0 to 266 Pa (0 to 2 torr). Data from this incremental filling of the vacuum vessel through repetitive pulsing of the gas valve are shown in figure 48.

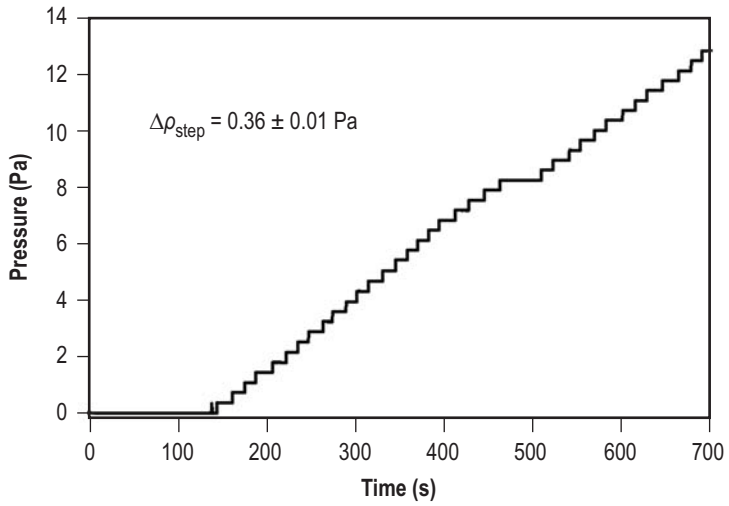

Figure 48. Pressure rise recorded for multiple openings of the PGV in single-shot mode on argon. The plenum pressure was 157 kPa (22.8 psig), and the temperature was 21.8 °C.

For the data in figure 48, the average incremental increase in pressure for each pulse was 0.36 ± 0.01 Pa (2.7 ± 0.1 mtorr). The mass per pulse, or mass bit, is given as

$$m_{\text{bit}} = nV m_{\text{Ar}} = \left(\frac{p}{kT} \right) V m_{\text{Ar}} \ , \tag{29}$$

where

n = number density
V = chamber volume
m_{Ar} = mass of an argon atom
p = pressure rise per pulse
T = temperature
k = Boltzmann's constant.

The mass bit measured in this way was 623 ± 54 μg/pulse.

In a subsequent test, the valve was operated a number of times in repetition-rated mode. The test was conducted on argon at a plenum pressure of 157 kPa (22.8 psig) and lasted for a total of 30 pulses at 10 Hz. The temperature recorded by the thermocouple was 22 °C (295.1 K). Between each burst of 30 pulses, a short interval was allowed to pass to permit equilibration of the pressure in the chamber. The incremental pressure increase data from this test are shown in figure 49. The fall in pressure at the end of the data set is the result of the vacuum vessel being evacuated as it is reexposed to the vacuum pump system. The average measured pressure change per pulse during this test is 0.76 ± 0.01 Pa (5.7 ± 0.1 mtorr). This corresponds to a total mass per sequence of 30 pulses of $1{,}315 \pm 90$ μg. In figure 49, a sharp rise in pressure at the beginning of each sequence is

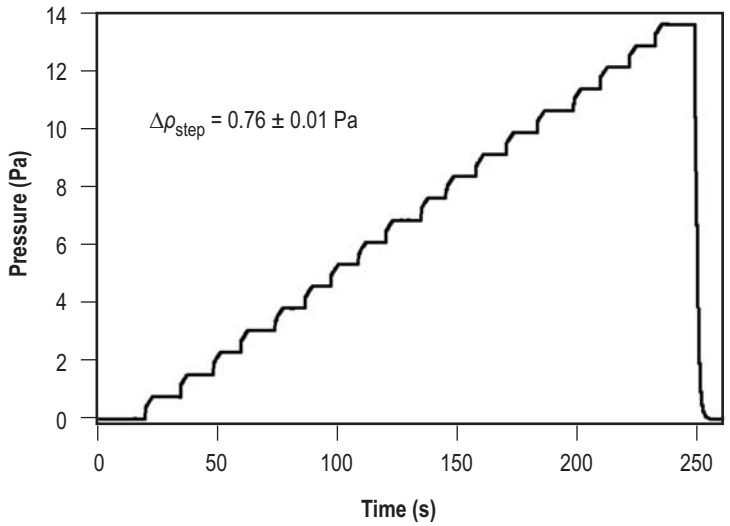

Figure 49. Incremental pressure rise recorded for multiple operations of the valve in repetition-rated mode on argon. For each discrete step, the valve was operated for 30 pulses at 10 Hz. The plenum pressure was 157 kPa (22.8 psig) and the temperature was 22 °C.

observed. This sharp rise is followed by a less rapid increase in pressure until that sequence of pulses is complete. The total duration of the rise is 3 s, as expected. The time response of the baratron is too slow to resolve the time-dependent pressure, and it is certainly too slow to permit a measurement of the mass bit from a time-resolved pressure increment per pulse. However, an estimate of the mass bit can be attempted by assuming that the valve plenum is exhausted during the first pulse, and that replenishment of the plenum is restricted during subsequent pulses in the pulse train by the limiting orifice on the plenum inlet. If this is the case, an amount of gas equal to the single-shot mass bit quantified in figure 48 (623 μg/pulse) is discharged during the first pulse and that the remainder of the pressure increase in the chamber occurs as propellant is exhausted at a uniform rate over the next 29 pulses. The mass bit for the remaining 29 pulses can then be estimated as $m_{\mathrm{bit}} \cong (1{,}315 - 623)[\mu g]/29\ [\mathrm{pulses}] = 24 \pm 4\ \mu g/\mathrm{pulse}$.

Higher mass bits could be obtained by using a larger limiting upstream orifice. Increasing the plenum pressure would also increase the mass bit. Such effects typically make the calculation of the change in mass bit too complicated, but the test setup described in this TP is capable of rapidly quantifying and calibrating the propellant delivery system response over a wide variety of operating conditions.

The closing time typical for valves of this kind is about 2 ms. While under typical 12-V operation, the opening time is expected to be on the same order; under the high-voltage initial pulse provided by the driver, the valve opens much more quickly. Current waveforms from the valve during two separate single-shot solenoid opening sequences are presented in figure 50. The curve ‘unloaded 1’ is the current provided to the solenoid when there is no valve stem. This is the case when the electrical load presented to the valve-driver is due only to the inductance and resistance of the

solenoid and not due to the dynamic impedance of the moving valve poppet. This curve exhibits the shape expected for an overdamped LRC circuit. The 'loaded' curve represents the current provided to the solenoid when the moving valve stem and poppet are in place and a valve opening will discharge argon into the vacuum vessel. This was performed at a plenum pressure of 150 kPa (21.7 psig). The loaded curve exhibits a marked jog owing to the dynamic impedance of the poppet moving under the influence of the magnetic field of the solenoid.

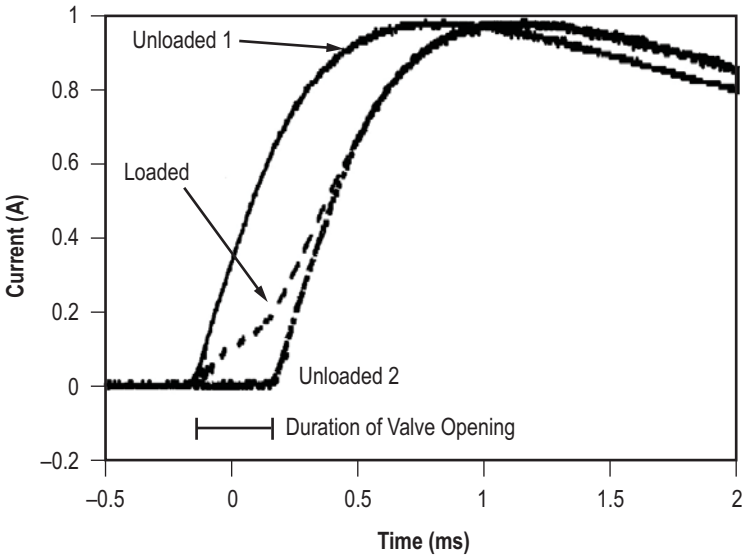

Figure 50. Current waveforms for valve solenoid in the loaded and unloaded cases.

While it takes longer due to the initial differences in the two curves, the current in the loaded case reaches the same peak value as in the unloaded case. Initially, the poppet moves rapidly as it lifts off the valve seat under the influence of the magnetic field, leading to a high dynamic impedance and hence, lower current. As the poppet is slowed by the restoring spring, the dynamic impedance decreases, and the current in the solenoid rises faster to its unimpeded value. The curve 'unloaded 2' is the same as unloaded 1, but time-shifted by 320 μs to align the peak current level with that of the 'loaded' curve. Note that in late time after the peak current, the two curves are indistinguishable from each other. The opening time is taken as equal to this time-shift. The horizontal bar in figure 50 is provided to show the magnitude of the time-shift on the graph.

5. LONG-LIFETIME PULSED GAS VALVE

It is advantageous for gas-fed, pulsed electric thrusters to employ pulsed valves so propellant is only flowing to the device during operation. The propellant utilization of the thruster will be maximized when all the gas injected into the thruster is acted upon by the fields produced by the electrical pulse. Gas that is injected too early will diffuse away from the thruster before the electrical pulse can accelerate the propellant. Likewise, gas that is injected too late will miss being accelerated by the already completed electrical pulse. This requires that the valve must open quickly and close equally quickly, only remaining open for a short duration. In addition, the valve must have only a small amount of volume between the sealing body and the thruster so the front and back ends of the pulse are as coincident as possible with the valve cycling, with very little latent propellant remaining in the feed lines after the valve is closed. For a real mission of interest, a pulsed thruster must cycle through at least 10^{10}–10^{11} valve actuation cycles,[30] setting the upper bound on the number of times a valve must open and close.

A PGV was designed and fabricated to have long lifetime and demonstrate the ability to rapidly open and close. The valve design and testing conducted under the present program are discussed in this section.

5.1 Requirements

The valve characteristics needed for the IPPT application requires a fast-acting valve capable of a minimum of at least 10^{10} valve actuation cycles. Since even 10^9 cycles is well above anything demonstrated, this value was selected as the design point. The valve seal must remain leak-tight throughout operation, and the body must maintain a low internal leakage at relatively high operating temperatures. The design requirements used for this program are given in table 1.

Table 1. Long-lifetime pulsed valve design requirements.

Parameter	Requirement
Flow rate	≥164 sccm (10 scim) GAr at 276 kPa (40 psia) inlet pressure, 0 kPa (0 psia) outlet pressure, and 21 °C (70 °F)
Opening and closing response	≤1 ms (goal) at 103–690 kPa (15–100 psid) and 21–149 °C (70–300 °F)
Internal leakage	$\leq 1 \times 10^{-3}$ sccs GHe at 103–690 kPa (15–100 psid) and 21–149 °C (70–300 °F)
Lifecycle	$>10^9$ cycles
Operating temperature	up to 149 °C (300 °F)

5.2 Design

Opening of the valve is accomplished by use of a solenoid electromagnetic actuator. The valve is normally closed and will fail closed upon loss of electrical power. When current is applied to the solenoid coil, magnetic forces pull the plunger away from the valve seat, allowing fluid to flow through the valve. Removal of the electrical current permits the spring and fluid pressure to seat the plunger, thus stopping the flow of fluid.

A flange-mounted interface is used between the valve and the PIT chamber. In the apparatus used for testing the valve, this interface contains both the supply and outlet ports to the valve and is sealed using two concentric O-rings. The test apparatus is illustrated in figure 51.

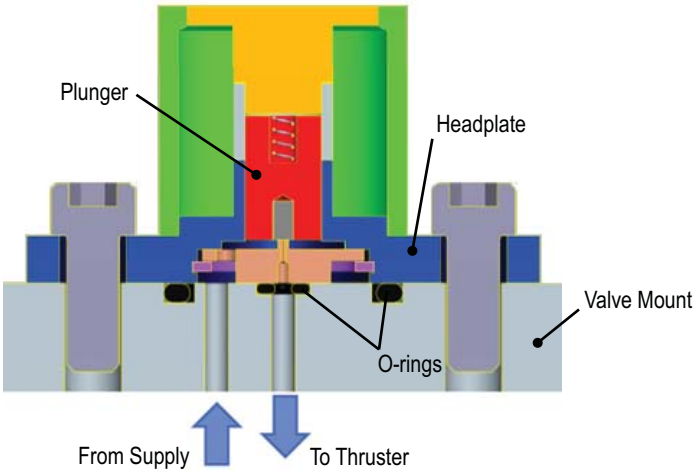

Figure 51. Cross-sectional view of the long-lifetime PGV assembly.

A secondary objective of the design was to minimize the valve size, making it not only applicable to the IPPT application, but also making it useful for other thruster platforms (e.g., microthrusters). The design was based solely on the use of analytical sizing calculations. Consequently, it does not represent a design optimized for mass and/or a given volume envelope. The valve envelope dimensions are shown in figure 52, with both a profile and a bottom view. The use of alternate materials combined with a more rigorous finite element analysis of the design could allow for a smaller/lighter future design iteration of this valve.

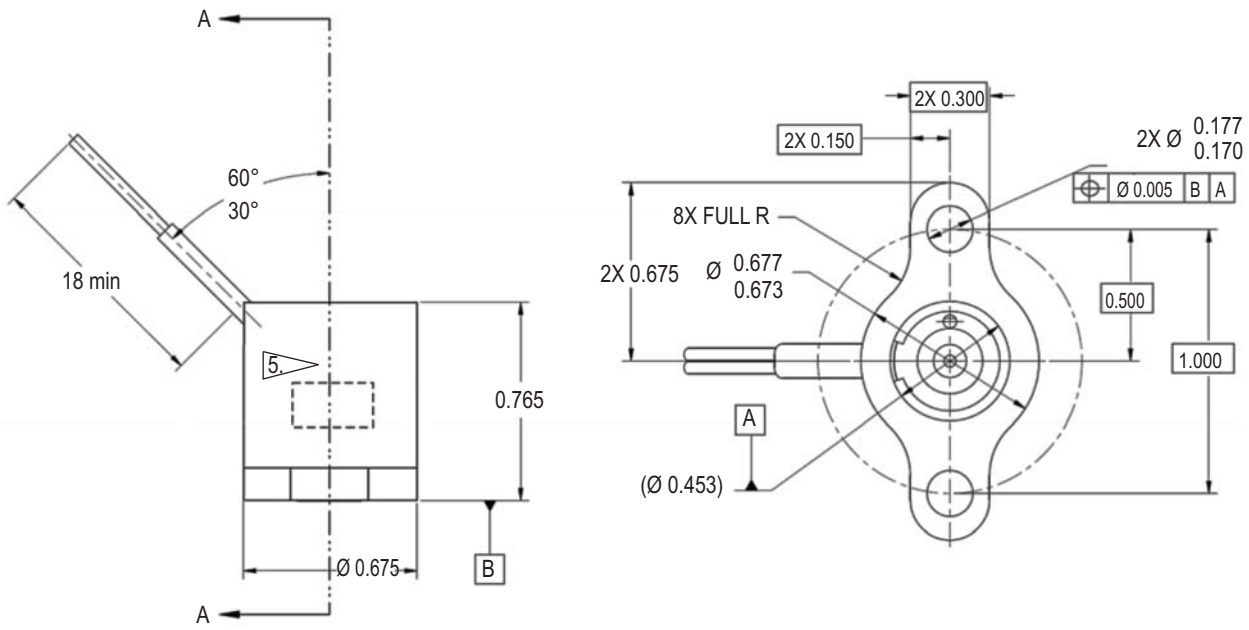

Figure 52. Drawings of the long-lifetime PGV showing (a) a profile view of the overall valve and (b) a view from the bottom.

5.3 Physical Construction

The valve, shown in detailed cross section in figure 53, is primarily fabricated from 304L corrosion resistant steel (CRES) and 430 CRES. The 430 CRES material is used in the parts of the valve that form the magnetic circuit, such as the plunger housing and spool end pieces, which must have a high magnetic permeability. This material does not have optimum magnetic properties, but its corrosion resistance permits incorporation in a design without requiring an additional plating process.

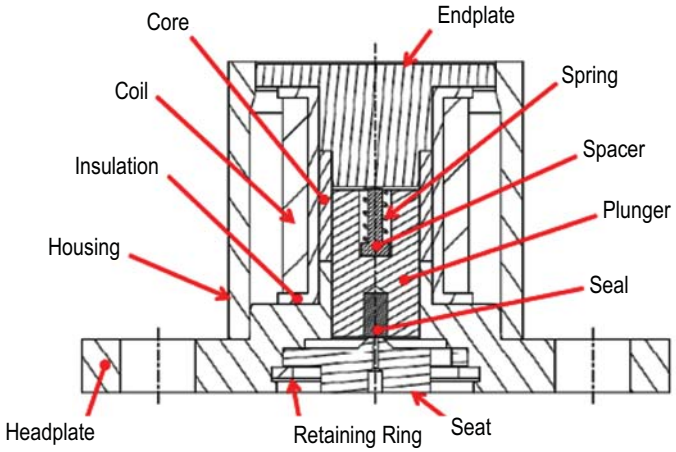

Figure 53. Cross-sectional view of the interior of the long-lifetime PGV.

A viton O-ring compound (Parker V0884-75) was used for the valve seat seal due to its mechanical strength at elevated temperatures. This seal material was installed into the plunger using a patent-pending process that eliminates the need for a separate seal retainer. The valve pressure boundary is sealed using electron beam welding at all valve joints as per AMS 2681.[31] Inspection of pre- and postweld samples and proof pressure testing were employed to verify weld integrity.

5.4 Initial Test Results

The testing performed at the time this TP was completed included a baseline evaluation of valve performance conducted before lifecycle testing. The tests were conducted at both 21 °C (70 °F) and 149 °C (300 °F) and included the following:

- Pull-in voltage.
- Dropout voltage.
- Opening response time.
- Opening plunger motion time.
- Closing response time.
- Flow rate.
- Internal leakage.

During initial checkout testing, several anomalies were encountered. The first anomaly occurred when the valve temperature was increased from room temperature to 149 °C (300 °F). As the temperature was increased, the flow rate observed from the valve outlet port decreased eventually to a point where the flow path was completely constricted. Further analysis showed that the designed stroke did not fully consider the effects of thermal swell of the viton seal material. The valve was disassembled and a new plunger assembly was installed with an additional 89 μm (0.0035 in) of stroke to account for thermal swell at elevated temperatures.

The second anomaly occurred during high-pressure, 1,034-kPa (150-psig) testing. During this test, internal leakage in excess of 10^{-2} sccs GHe was observed using a manometer. A review of the test configuration showed that the inner O-ring used to seal between the pressure supply and valve outlet ports did not contain any inner diameter supports. As a consequence of this lack of the inner diameter supports, the O-ring would roll inwards when this level of pressure was applied, producing a leakage path. In the test configuration, gas leakage at this O-ring gives a false-positive interpretation as internal leakage. The valve was removed from the test fixture, and the inner O-ring was replaced. Testing has subsequently been limited to no more than 45 psig. Higher pressure testing is possible if a test fixture modification to correct the O-ring support issue is implemented.

After experiencing these two anomalies, the valve was tested producing a baseline evaluation of performance. These tests are summarized in table 2.

Table 2. Test data showing the baseline response of the long-lifetime PGV under a range of experimental conditions.

Parameter	21 °C (70 °F)	149 °C (300 °F)	Requirement
Pull-in voltage			
at 103 kPa (15 psig)	13.1 VDC	10.2 VDC (0.145 A)	≤18 VDC
at 276 kPa (40 psig)	13.1 VDC	10.9 VDC (0.156 A)	≤18 VDC
Drop-out voltage			
at 103 kPa (15 psig)	1.0 VDC	1.8 VDC (0.026 A)	≥0.5 VDC
at 276 kPa (40 psig)	1.0 VDC	1.8 VDC (0.026 A)	≥0.5 VDC
Total opening response time			
at 103 kPa (15 psig)	1.53 ms	0.96 ms	<1 ms (goal)
at 276 kPa (40 psig)	1.52 ms	1.02 ms	<1 ms (goal)
Plunger opening time			
at 103 kPa (15 psig)	0.47 ms	0.28 ms	<1 ms (goal)
at 276 kPa (40 psig)	0.47 ms	0.28 ms	<1 ms (goal)
Total closing response time			
at 103 kPa (15 psig)	0.76 ms	0.70 ms	<1 ms (goal)
at 276 kPa (40 psig)	0.49 ms	0.46 ms	<1 ms (goal)
Flow rate			
at 103 kPa (15 psig) GN_2	352 sccm (21.5 scim)	Not Yet Tested	>100 sccm (6.1 scim)
at 276 kPa (40 psig) GN_2	634 sccm (38.7 scim)	Not Yet Tested	>266 sccm (16.25 scim)
Internal leakage			
at 103 kPa (15 psig) GHe	$<10^{-3}$ sccs	$<10^{-3}$ sccs	$<10^{-3}$ sccs
at 276 kPa (40 psig) GHe	$<10^{-3}$ sccs	$<10^{-3}$ sccs	$<10^{-3}$ sccs

5.5 Summary

In baseline testing, the PGV design has shown itself capable of meeting the requirements for use in an IPPT providing primary propulsion for a mission. While requiring some minor design modifications that require further development, the valve meets the target performance metrics in beginning-of-life testing. Future testing after the valve has completed a large number of cycles will be used to evaluate the lifetime of this design and determine if it could be capable of operating through enough cycles to complete a mission.

6. HIGH-VOLTAGE INDUCTIVE PULSED PLASMA THRUSTER POWER PROCESSING UNIT DEVELOPMENT

An IPPT is an inherently unsteady device, with capacitor banks undergoing repeated cycles of charging and discharging. To operate the thruster in any type of repetition-rate mode, the bank must be recharged quickly to a high voltage of several kilovolts between pulses. This implies that the bus voltage from the spacecraft must be transformed in the PPU to a high-voltage, relatively high-current level that can transfer the level of charge required for nominal operation in a relatively short period of time (fractions of a second).

The specifications for the PPU design and development work conducted during the course of this TP were as follows. It was assumed that the thruster possessed a 40 μF capacitor bank and that this would be charged from 0 to 4 kV, and at full voltage, this would result in a discharge energy of 320 J/pulse. It was assumed that the bus voltage feeding the PPU was 120 VDC (which corresponds to, among other things, the governing voltage on the International Space Station). The goal for this work was to investigate hardware that could recharge the capacitor bank at a rate that would permit operation on a timescale corresponding to a repetition-rate of approximately 30 Hz.

6.1 Power Processing Unit Design

The PPU designed in this project incorporates a coupled inductor topology of a flyback converter, also known as a buck-boost converter. The converter circuit is shown schematically in figure 54. Inductive field energy is stored in the inductor when the metal-oxide semiconductor field-effect transistor (MOSFET) in line with the primary side of the transformer is closed. When the MOSFET is opened, current flow through the primary side of the transformer is halted, and the inductively stored energy is transferred to the secondary side of the transformer, subsequently charging the capacitor bank. Over a number of cycles, the voltage on the capacitor bank will increase until the desired bank voltage is achieved. Voltage regulation on the capacitor is performed using a voltage divider to measure the voltage and a comparator to determine if the target bank voltage has been achieved. The operation for the coupled inductor power converter is illustrated conceptually in figure 55.

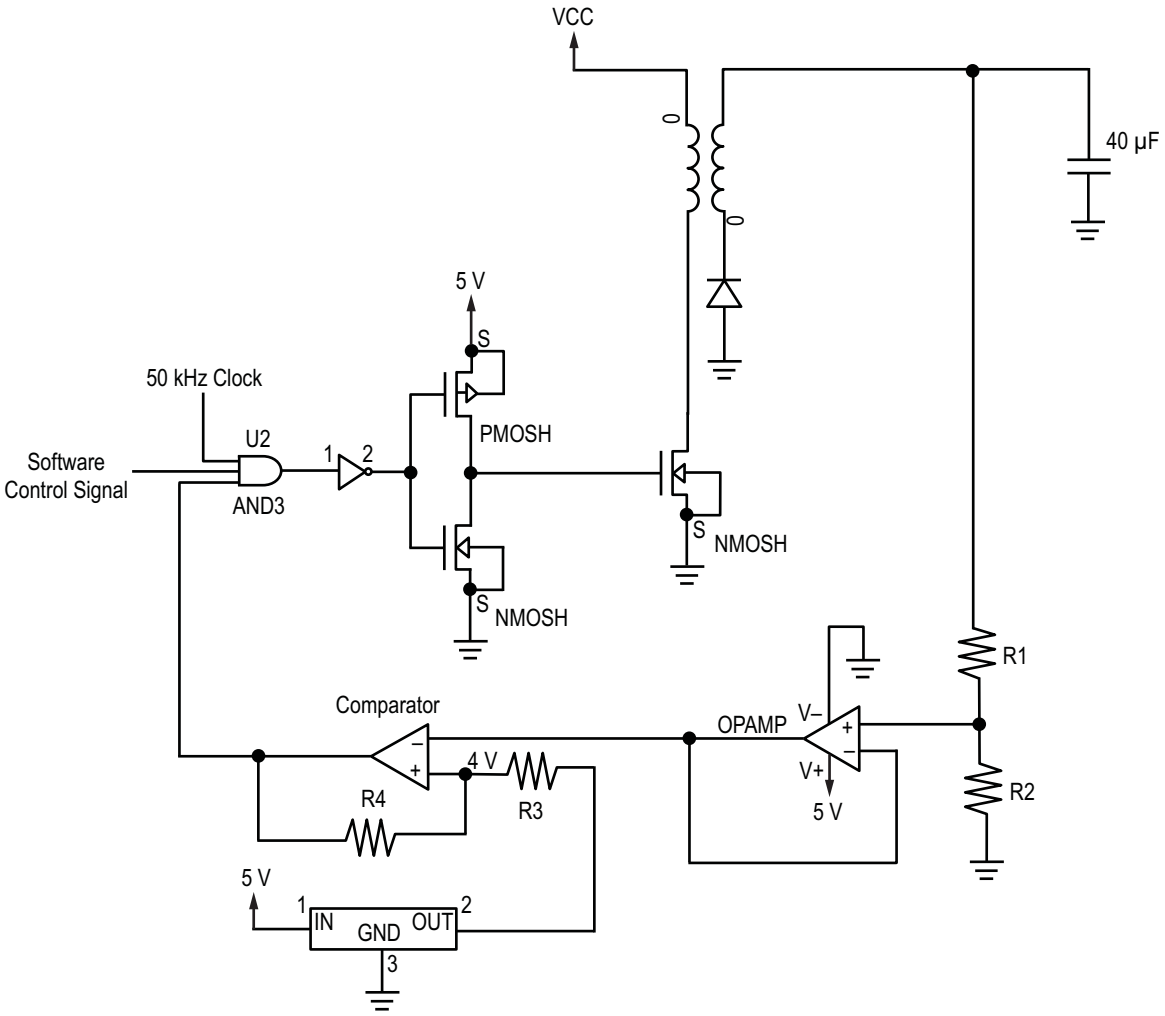

Figure 54. Circuit schematic for the coupled inductor PPU design.

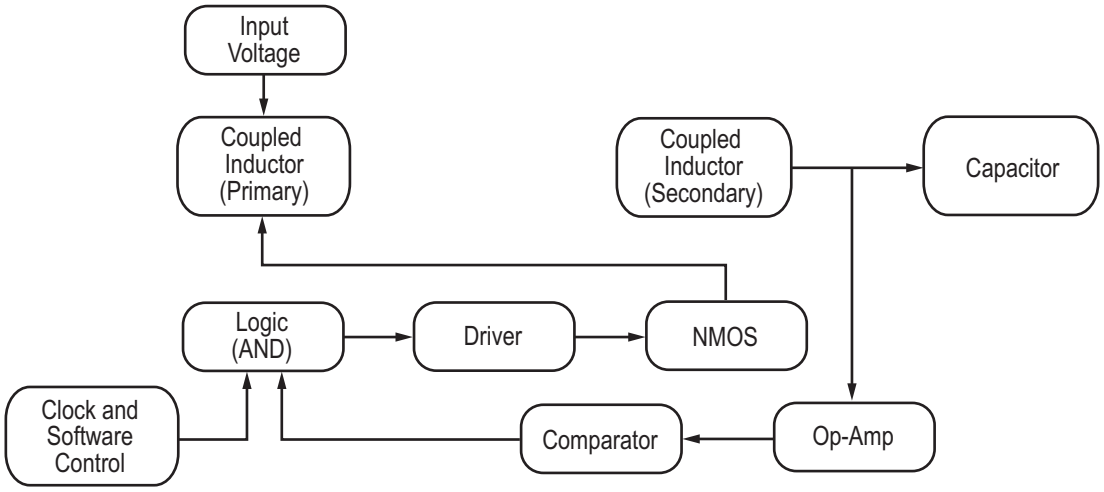

Figure 55. Concept of operation for the coupled inductor PPU design.

For a full 4-kV charge, a 1,000:1 voltage divider on the capacitor bank allows a comparator, referenced to 4 V, to determine when the charging sequence should be halted. A 50-kHz clock is used switch the flow of current through the transformer, controlling the charging sequence. This frequency was chosen because this bandwidth capability is readily available on the market, and it is a value that permits beneficial reduction in the transformer size and associated magnetic losses throughout the system. In the present design, the clock switches the current to maintain a 50% duty cycle. While the constant duty cycle was used in this design, further research may reveal that varying the duty cycle can permit better control of initial current transients. At a constant 50% duty cycle, the transformer is charged in 10 μs, and in another 10 μS, that energy is transferred to the capacitors. For a 120-VDC input, this results in 213 mJ of energy transferred per pulsed cycle, with 1,500 pulsed cycles over 30 ms required to charge the bank to 320 J (40 μF at 4 kV). Once the charging cycle is complete, a switch is activated to electrically isolate the capacitor from the charging system/PPU, providing protection for the PPU during the pulsed discharge of the capacitor bank.

The design can employ both hardware and software controls on the capacitor charging sequence. The charging cycles are performed using hardware, but software can be used to monitor the system and also to provide a secondary avenue for the implementation of safety measures. A field programmable gate array can offer many of these advantages and provide adequate charging system control and safety measures in future iterations.

6.2 Experimental Results

The control system for the PPU operates on standard transistor-transistor logic. The output to the capacitor bank is monitored, with the monitoring signal into the comparator scaled through a voltage divider to the 0 to 4 V range. The charging sequence is halted when the voltage into the comparator reaches or exceeds 4 V. The charge sequence should be completed in 30 mS, allowing 3.3 mS to discharge the capacitor bank and allow the system to reinitialize before the next charging sequence commences.

The coupled inductor charging supply concept shown in figure 54 was simulated using Personal Simulation Program with Integrated Circuit Emphasis (PSPICE) to determine the efficacy of the design. The PSPICE results shown in figures 56(a)–(c) are for a PPU design scaled to an input voltage of 1% of the design value (1.2 VDC input), resulting in a commensurate capacitor charge of 40 V. This simulation is representative of the first scaled-down test apparatus that was fabricated for the project (1/100-scale). A second prototype at 1/10-scale was also fabricated and tested. Results from testing with these two prototype systems are discussed in turn within this subsection.

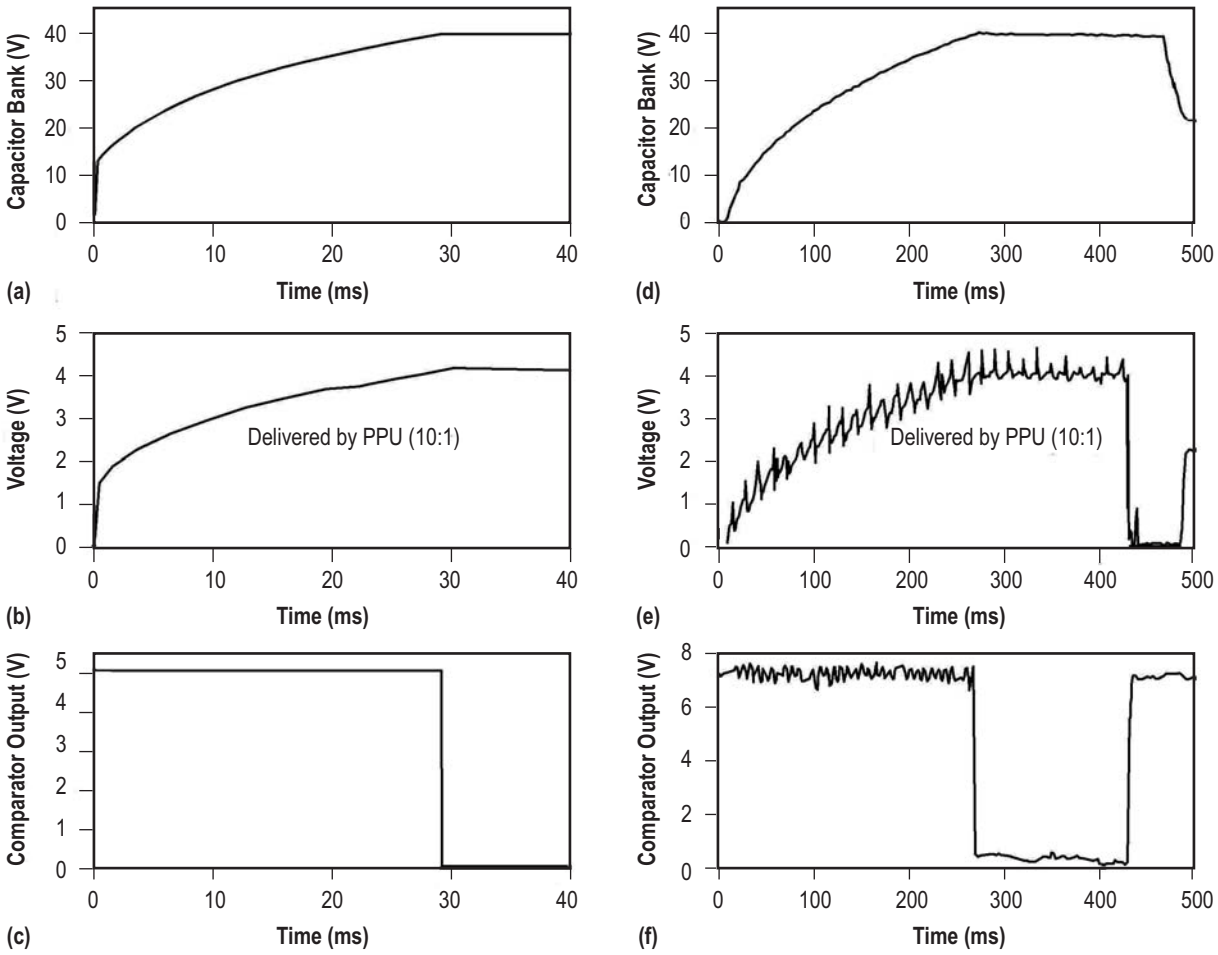

Figure 56. PSPICE simulation ((a)–(c)) and experimental data ((d)–(f)) for a 1/100-scale coupled inductor PPU system.

6.2.1 First Prototype—1/100-Scale

In the 1/100-scale prototype, a 1.2-VDC input supplied power to the PPU, resulting in a charge voltage of 40 V. A charging sequence is shown in figures 56(d)–(f), with the voltage on the capacitor reaching 40 V in approximately 260 ms. This was slower than the PSPICE simulation suggested, and upon investigation, it was determined the transformer started operation in a continuous mode and then it would transition to a discontinuous mode. In the continuous mode, energy remains on the secondary transformer coil at the end of a pulsed cycle, while in the discontinuous mode, the inductor is completely depleted, and all the energy is transferred to the capacitor bank by the end of a cycle. In the discontinuous mode, the current can be up to two to three times as large as in the continuous mode, providing for faster energy transfer. A major advantage is the smaller required mutual inductance that will, in turn, benefit the power converter by reducing magnetic losses. In the discontinuous mode, the higher peak secondary current and an associated large voltage spike at turnoff limits the selection of components for the system.[32] While the discontinuous mode has

disadvantages when attempting to regulate current and voltage, this disadvantage does not directly affect the performance of the power converter described in this TP.

An issue with operating on a 1.2-VDC input is that the components, such as MOSFET transistors, had turn-on voltages in the 2 to 4 V range. Consequently, the MOSFETs were mainly operating in the triode region instead of in saturation where the best results could be achieved. This problem will abate as the input voltage is increased. An additional problem that arose during testing was that the comparator circuit that terminated charging when the capacitor bank reached full voltage did not incorporate hysteresis. The consequence of this can be observed in figure 56(b), where instead of permitting the capacitor to fully discharge, the charge sequence would start as soon as the voltage measured by the comparator dipped below 4 V.

6.2.2 Second Prototype—1/10-Scale

The 1/10-scale prototype operated on an input voltage of 12 V, permitting the MOSFET transistors to operate in the saturation regime. The output charged a capacitor to 430 V over 80 ms. The comparator was set to halt the charging sequence at a voltage (measured using a 100:1 voltage probe) of 4.3 V, resulting in a slight overcharging of the capacitor above the target 400 V. The slight overcharge ensured the desired voltage was achieved and would compensate for slight leakages that might arise. The overcharge did serve to increase the charge time, implying that an additional improvement in time could be realized by setting the upper threshold voltage of the comparator hysteresis to 4 V. The lack of hysteresis in the 1/100-scale prototype system comparator was addressed in the 1/10-scale system by incorporating a Schmitt trigger into the comparison circuitry, providing a wide hysteresis (0.8 V and 4.3 V) to prevent spurious or unplanned initiation of the charging sequence.

During testing, the charging sequence was activated with a control signal lasting 320 ms. The capacitor would charge in a much shorter timespan, testing the ability of the comparator to halt the charging sequence. A waveform showing the voltage on the capacitor bank during charging is presented in figure 57. Two sets of data presented in figure 58 show waveforms for the control signal that enables the charging system, the 100:1 voltage divider measurement on the capacitor bank, and the comparator signal (which goes to 0 when the full charge voltage is reached) to end the charge sequence. The transient portion of the data in figure 58(a) is enlarged for clarity in figure 58(b).

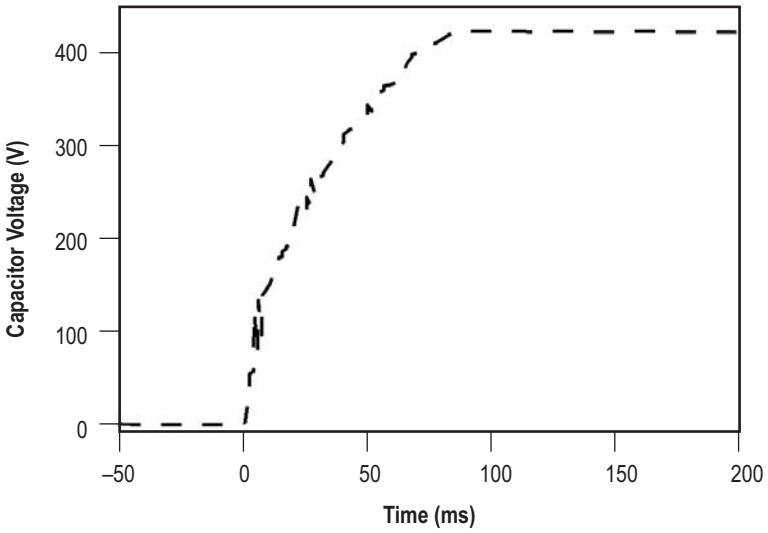

Figure 57. Charge voltage waveform on the capacitor bank for the 1/10-scale coupled inductor PPU system.

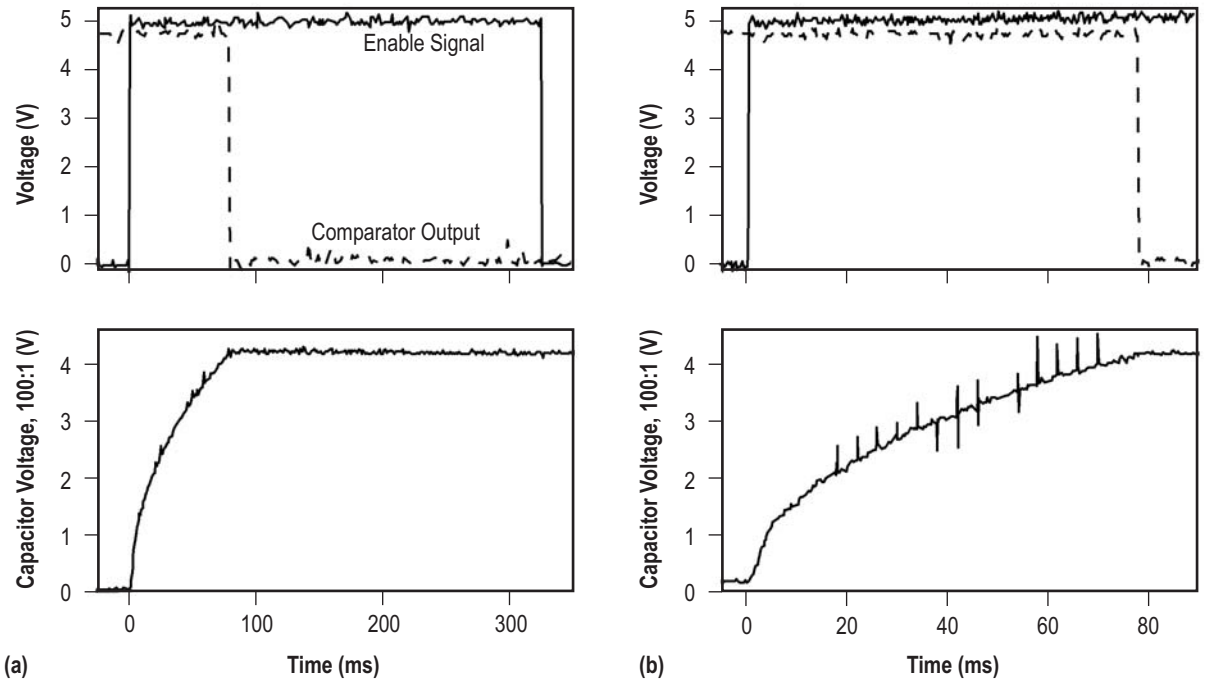

Figure 58. From the 1/10-scale coupled inductor PPU: (a) Waveforms for the control signal, 100:1 voltage divider measurement, and comparator output for the charge in figure 57, and (b) enlargement of the waveforms to better show the transient region.

A minor issue was observed in figure 58 at the beginning of the charge sequence. The separate pieces of equipment could not be properly synced during the first clock cycle of the charging sequence. Specifically, the data acquisition system operated at a frequency bandwidth of 20 kHz, while the power converter was operating on a 50-kHz clock, creating some aliasing problems resulting in improper control of the power converter. This had a minor impact since the circuit was not operating in the discontinuous regime throughout the charge sequence.

The magnetic design has been shown even in the 1/10-scale prototype to be a key to the overall system performance. The losses due to inductive leakage and providing for optimal energy transfer from the transformer to the capacitor through operation in the proper regime (discontinuous versus continuous) are critical in lowering the charge time in the system. In the prototypes, a low-mu (low-permeability) core was used to permit higher power transfer, which is common in power supply design.

6.3 Additional Background and Insights

In testing of the 1/100- and 1/10-scale prototypes, the PPU design demonstrated scalability and a reduction in charge time as the size was increased. While a full-scale design would require more robust components, potentially configured as stacks of components in series and parallel to handle the loads, the success of the prototypes suggests that a full-sized prototype is feasible. Improvement of the control equipment, specifically the frequency response of the data system, can help realize further improvement in PPU operation.

The magnetic design for the transformer has proven to be the critical component in the design for both the 1/100- and 1/10-scale prototypes. This design problem will be even more critical in a full-scale PPU. The leakage inductance of the transformer, the magnetic permeability of the core, the configuration of the windings, and the slurry material comprising the toroid used for the transformer are all factors that require improvement to permit the fabrication of a full-scale system. It was suggested that a nanocrystalline core may help alleviate some of the transformer design concerns (M. Stangenes, Personal Communication, Stanges Industries, Inc.).

It was also suggested that a stack of diodes would be required to charge the capacitor bank (C. Chandler, Personal Communication, Southeast Power Components, Inc.). These diodes experience large swings of high initial current at low voltage during the charging pulses. Testing of diode stacks should be undertaken as part of any future work to extract data regarding the feasibility of this scheme.

The transistor used on the primary side of the transformer must also be selected with care. As the PPU increases to full-scale, the voltage stress on the transistor may cause problems. A possible solution is to use a stack of transistors instead of the single N-channel MOSFET currently used on the 1/100- and 1/10-scale prototypes.

7. CONCLUSIONS

The contents of this TP have summarized IPPT development and testing performed at MSFC during the fiscal year 2012. This program was aimed at starting the process of identifying and addressing several critical IPPT development issues. During the course of this work, the following activities were completed:

- Several CTP IPPTs were fabricated, mounted on a thrust stand, and operated in a single-pulse mode in a large vacuum chamber, providing direct measurements of the impulse bit and permitting an estimate of the thrust efficiency.

- A capacitor charging system was assembled to provide for fast recharging of an IPPT capacitor bank, permitting repetition-rate operation. A CTP IPPT was subsequently tested at a repetition-rate of 5 Hz, which at 5 kV on a 40 μF bank represents a power of 2.5 kW, which to the authors' knowledge is over an order of magnitude greater than any previous repetition-rate operated, pulsed plasma thruster.

- Multiple components for a small-scale, flat-plate IPPT were fabricated. This device was different from the CTP in that it was equipped with the capability to employ pulsed gas injection and the capacitor bank was to be discharged with a solid-state switch. The assembly and integration process for this thruster was not yet completed by the end of the present program.

- A prototype long-lifetime PGV was fabricated, and testing was initiated to quantify the response time and internal leak rate at the beginning-of-life. This valve will be tested in future work to quantify the lifetime and changes in leak rate as a function of the number of times the valve is cycled.

- An investigation into the power systems needed for an IPPT was initiated under this program. Subscale 1/100- and 1/10-scale breadboard power supplies that could accept a low DC bus voltage input and provide a voltage to charge an IPPT capacitor bank were fabricated and tested to quantify the response of the design. Many insights into the improvement of the power system response time and the types of components required were gained during the course of the present effort.

APPENDIX A—BASIC CODE FOR CUBLOC 64T CONTROLLER AND PERIPHERALS

```
'  EPVALVE Controller
'  Program for Cubase 64T  RE  3/26/12 Comfile Cubloc BASIC
'   V 5.0
'
'   This one works very well!
'
'   first version to use control panel to set parameters
'   also use the LCD screen V1.0,  also now has comments
'   mode 1,2,3 all work (10,20, 30 Hz, set to 5 Hz at startup)
'   mode 4 allows you to program delay time between pulses, the "on"
'   time  and the # of pulses,  goto mode 4 and set # pulses,  then return to
'   mode 1 2 or 3 to change pulses
'
'   NOTE:  Cubase 64T has a board error,  for some reason when more than
'   one input is active at a time,  then ALL 8 inputs in each common ground
'   block are active.  this more or less precludes the use of sw1,sw2, an sw3
'   Also I had to use a battery to power each button because if the system power
'   is used on any 8 port group,  then the whole group lites up also.
'   Fortunately,  the battery only draws current when a button is being pressed
'   so it should last a long time.  This was easier than starting all over with
'   another board
'   modified 12/12/11  to start up in single shot mode
'
' 3/27/2012
'          ' This version uses 3 inputs...  the start button and the 2 POF fibers
'   pressing the start button will start the sequence without "fill"  and
'   "shutoff"  valve support.   Starting with the POF # 1 will initiate the
'   sequence with flow valve open.   Activating POF #2  will fill the run tank
'
' 6/4/12
'          'This version supports the display of the tank pressure (from AD5),
'the run pressure (from AD4),  and the temperature (from AD6) on the debug screen
'
'Ports:
'
'Outputs
'
'P24  Terminal F on FO board (see notes p11)
'P25  Terminal E on FO board
'P26  Terminal D on FO board
'P27  Terminal C on FO board
'P28  Terminal B on FO board
'P29  Terminal A on FO board
```

```
'P30  FO POF XMTR 2 on FO board (T2)
'P31  FO POF XMTR 1 on FO board (T1) fires the valve
'P32-P39 Connector 15  (see notes p10)
'P40-P47 Connector 16  (see notes)
'P48-P55 Connector 17  (see notes)
'Port 48  "fill" valve relay (1= open)
'Port 49  "flow" valve relay (1 = open)
'port 50 spare relay
'port 51 spare relay
'port 52 thermistor iso relay
'port 53 tank press iso relay
'port 54 run press iso relay
'port 55 agnd iso relay
'
'Inputs
'
'P87 Enter Button (use to enter mode or set value)
'P86 Status button press to see pressure and temp on debug screen RE 6/4/12
'P85 Program Button (use to go into program parameter mode)
'P84 Start Button (use to start a valve pulse sequence)
'P83 cursor left button (use to select menu option) not used
'P82 cursor right button (use to select menu option) not used
'P81 Switch 3 can't use because of board error
'P80 not connected
'
'P79-P72 connector 12 (see notes)
'P71-P64 connector 11 (see notes)
'P63-P56 connector 10 (see notes)
'
'Analog Inputs (these are 5.0 VFS, 10 bits, 5V=1023 cnts, 0V=0 cnts)
'
'AD0- Rotary Switch (see notes p 9) 4.481,3.812,2.713,1.362 volts (left to right)
'      4.481 is INT 930 (Mode 1), 3.812 is INT 792 (Mode 2),
'      2.713 Is INT 563 (Mode 3) , 1.362 Is INT 281 (Mode 4)
'
'AD1- Enter Value Pot (see notes p. 9)fully CW 4.794 volts, fully CCW 0 0olts
'    integer values 0 - 982
'AD2- FO Receiver 1 (see notes p 11)  226 dark   268 light ... start with flow valve
'AD3- FO Receiver 2 (see notes p 11)  220 dark   268 light ...fill command
'AD4- Run pressure 0-5V,  has 0.5 V offset, range (0-50 psig) 0.5-5 Volts=0-50
'AD5- Tank pressure 0-5V,  has 0.5 v offset, range (0-200 psig) 0.5-5 Volts=0-200
'AD6- Thermistor 0-5 V,12.06 K in series as divider, Omega #55016 12.5 K @ 20C
'AD7- spare
'
'          *** Note AD4,5,6 are routed through relays as follows:  ***
' AGND=P32, (AD4)XDUCER2=P31, (AD5)XDUCER1=P30, (AD6)Thermistor=P29 to protect
' the Cubloc controller during charge and firing of the thruster
' to read AD4,5,6  first make P32,31,30,29  high,  then make these low again before firing
'
'
```

```
Const Device = cb290
'
' variables in Main program are all global variables
'
Dim TX1 As Integer, TY1 As Integer
Dim I As Integer
Dim jj As Integer
Dim a0 As Integer
Dim a1 As Integer
Dim a2 As Integer
Dim a3 As Integer
Dim imode As Integer
Dim ihz As Integer
Dim ipulses As Integer
Dim iperiod As Integer
Dim isec As Integer
Dim ipress As Integer
Dim iton As Integer
Dim ipro As Integer
Dim ifirst As Integer
Dim ifill As Integer
Dim iflow As Integer
Dim istat As Integer
Dim RunP As Single ' run pressure (PSIG)
Dim FillP As Single ' fill tank pressure (PSIG)
Dim TTemp As Single ' fill tank temperature (C)

Set Outonly On  'required for cb290

 '
 '  set for a clcd display using Cunet with address 0  and buffer size of 72 bytes
 '
 Set Display 2,0,0,72

 '
 ' write startup message
 '
 startup:
 '
 '
 '
 Delay 100
 Cls
 Delay 200
 Locate 0,0
 Print "Starting Up!"
 Delay 2000
Locate 0,0
 Pause 100
```

```
 Print "EP Valve Controller "
 Locate 0,1
Pause 100
 Print "V4.0 press start! "
 Locate 0,2
 Pause 100
 Print "Single Shot Mode"
'default parameters
ifirst=1
iperiod=205
ihz=5
isec=2
iton=1
ifill=0
iflow=0
'ipulses=ihz*isec
ipulses=1
getmode
Pause 100
Locate 0,3
Print "# Pulses  ",Dec(ipulses)
Do

 'set all the outputs low (outputs are 24 thru 55 on Cubase 64)
 '
 I=24
Do Until (I > 55)
                    Out I,0
          I=I+1
Loop
 '
 '  test all the inputs (56 thru 87)
 '
 ' wait to press start button
 '
 Waitstart
 If (iflow = 1 ) Then Out 49,1
 If (iflow = 1 ) Then Pause 1000
 PulseValve ipulses, iperiod
 Out 49,0
 Pause 500
  Loop
  End

Sub PulseValve(ipul As Integer,iper As Integer)
'
' fire the valve ipul times at rate given by iper
Dim II As Integer
II=0
```

```
If (iflow = 1) Then Out 49,1  ' use flow valve if commanded by FO to start
If (iflow = 1) Then Delay 2000
Do Until (II=ipul)
High 31
Pause 1
II=II+1
Low 31
Pause iper
Loop
Out 49,0
iflow = 0
End Sub

Sub Waitstart()
'
' wait for start button to be pressed or for signal on FO receiver 1
'  if program button is pushed change parameters and come back here
'  if ad3 (FO2) is active then fill the run tank (ifill is made 1)
'  if ad2 (FO1) is pulsed then open the flow valve and run the sequence (iflow =1)
'
'
Dim igo As Integer
Dim ir1 As Integer
Dim ir2 As Integer
Dim ibut As Integer
igo=0
ipro=0
ibut=0
ifill=0
iflow=0
Do Until (igo=1)
ir1=Tadin(2)  'ad2 Is the FO receiver ir1
If (ir1 > 245) Then iflow=1
ir2=Tadin(3)  'ad3 is the FO receiver ir2
If (ir2 > 245) Then ifill=1
ibut= In(84)  'port 84 is the start button
ipro = In(85) ' port 85 is the program button
istat = In(86) ' Port 86 is the status button
If (ipro=1) Then ChangeParameter
If (ifill=1) Then Fill
If (istat=1) Then Status
If ((ir1 > 245) Or (ibut =1)) Then igo=1
Loop
ibut=0
igo=0
End Sub


Sub ChangeParameter()
```

```
"come here if program button is pushed and parse buttons to change parameters
'
'global parameters  iperiod, ipulses, ihz, imode, isec, ipress, iton
'
getmode
If (ifirst=1) Then ipulses=30
If (ifirst=1) Then ifirst=0
If (imode=4) Then Goto setmode
If (imode=1) Then Goto mode1
If (imode=2) Then Goto mode2
'
' here if mode 3 (30 Hz)
'
mode3:
'30 Hz
ADOFF
iperiod=30
Delay 100
Cls
Delay 200
 Locate 0,0
 Print "Mode 3 Active!"
Delay 2000
Locate 0,0
Print "EP Valve Controller "
 Locate 0,1
Print " M3 press start! "
Locate 0,2
Print "valve out 30 Hz"
Pause 100
Locate 0,3
 Print "# Pulses  ",Dec(ipulses)
 Goto last2
'
' here if mode 2 (20 Hz)
'
mode2:
'20 Hz
ADOFF
iperiod=47
Delay 100
 Cls
 Delay 200
 Locate 0,0
Print "Mode 2 Active!"
Delay 2000
 Locate 0,0
Print "EP Valve Controller "
Locate 0,1
```

```
Print " M2 press start! "
Locate 0,2
Print "valve out 20 Hz"
Pause 100
 Locate 0,3
Print "# Pulses  ",Dec(ipulses)
 Goto last2
'
' here if mode 1 (10 Hz)
'
mode1:
'10 Hz
ADOFF
iperiod=100
 Delay 100
 Cls
 Delay 200
 Locate 0,0
Print "Mode 1 Active!"
Delay 2000
Locate 0,0
 Pause 100
Print "EP Valve Controller "
Locate 0,1
Pause 100
Print " M1 press start! "
Pause 100
Locate 0,2
Print "valve out 10 Hz"
Pause 100
Locate 0,3
 Print "# Pulses  ",Dec(ipulses)
Goto last2
'
'here if mode 4  (set mode parameters)
'
setmode:
'
' set period (Hz)
Cls
Pause 100
Locate 0,0
Pause 100
Print "Set Parameters "
Pause 100
Locate 2,0
Pause 100
Print "Set Period value"
ipress=0
```

```
Do Until (ipress=1)
        iperiod=Tadin(1)
        iperiod=iperiod/3
        ipress=In(87)
        Locate 0,3
        Pause 100
        Print "Period  ",Dec(iperiod),"  "
        Pause 300
Loop
' set time on
Cls
Pause 100
Locate 0,0
Pause 100
Print "Set Parameters "
Pause 100
Locate 2,0
Pause 100
Print "Set On Time value"
ipress=0
Do Until (ipress=1)
        iton=Tadin(1)
        iton=iton/30
        If (iton=0) Then iton=1
        ipress=In(87)
        Locate 0,3
        Pause 100
        Print "Time on  ",Dec(iton),"  "
        Pause 300
Loop
' set number of pulses
Cls
Pause 100
Locate 0,0
Pause 100
Print "Set Parameters "
Pause 100
Locate 2,0
Pause 100
Print "Set # pulses"
ipress=0
Do Until (ipress=1)
        ipulses=Tadin(1)
        ipulses=ipulses/3
        ipress=In(87)
        Locate 0,3
        Pause 100
        Print "Pulses ",Dec(ipulses),"  "
        Pause 300
```

```
Loop
Delay 100
Cls
Delay 200
Locate 0,0
Print "Starting Up!"
 Delay 2000
Locate 0,0
Pause 100
Print "EP Valve Controller "
 Locate 0,1
Pause 100
Print "press start! "
Pause 1000
Locate 0,1
Pause 100
Print "Period ",Dec(iperiod),"   "
Locate 0,2
 Pause 100
Print "Time on ", Dec(iton),"   "
Locate 0,3
Pause 100
Print "Pulses ", Dec(ipulses),"    Mode 4"
ipro=0

last2:
End Sub

Sub getmode()
'
'determine the operating mode from the rotary switch
'
' get mode
'imode and a0 are global
'
'Mode 1 is 10 Hz, Mode 2 is 20 Hz , Mode 3 is 30 Hz Mode 4 is set Hz
a0=Tadin(0)
'Debug "getmode ",Dec(a0),Cr
If(a0 < 900) Then Goto aa
imode=1
Goto last1
aa:
If(a0 < 700) Then Goto bb
imode=2
Goto last1
bb:
If(a0 < 500) Then Goto cc
imode=3
Goto last1
```

```
cc:
imode=4

last1:
End Sub



Sub Fill()
'
' Leave fill valve open until fill command goes low
'
Dim idone As Integer
Dim ir2 As Integer

idone=0
Out 48,1  'Port 48 is fill valve ,port 49 is the flow valve
          Do Until (idone=1)
            ir2 = Tadin(3)
          If (ir2 < 245) Then idone =1
          Loop
Pause 1000  ' minimum fill time is 1 sec
Out 48,0
ifill=0
idone=0
End Sub

Sub ADON()
'
'Enable the AD ports - do this only when High Voltage is OFF
'
Out 55,1  ' AGND
Out 54,1  ' Xduc2
Out 53,1  ' Xduc1
Out 52,1  ' Thermistor
End Sub

Sub ADOFF()
'
'Disable the AD ports to protect them from High Voltage
Out 55,0  ' AGND
Out 54,0  ' Xduc2
Out 53,0  ' Xduc1
Out 52,0  ' thermistor
End Sub

Sub Status()
Dim itankp As Integer
Dim irunp As Integer
```

```
Dim itemp As Integer
Dim itanksum As Integer
Dim irunsum As Integer
Dim itempsum As Integer
Dim icnt As Integer
Dim tpr As Single
Dim rpr As Single
Dim ttr As Single
Dim ist As Integer
'
' Come here when status button is pressed and print out the Pressures and temperatures
' RunP  FillP  TTemp are real global variables for Fill press, Run press  and Temperature
'
ADON ' enable these channels

Out 48,1 ' fill valve
Out 49,0  ' flow valve
Pause 400
ist=0
Do Until (ist = 1)
itanksum=0
irunsum=0
itempsum=0
icnt=0
        Do Until ( icnt=50 )
                itanksum=itanksum+Tadin(5)
                irunsum=irunsum+Tadin(4)
                itempsum=itempsum+Tadin(6)
                icnt=icnt+1
        Loop

tpr=(200.0*((itanksum/10230.0)-0.5)/4.0)-1.15
rpr=(50.0*((irunsum/10230.0)-0.5)/4.0)-0.22
ttr=itempsum/50.0
Debug "Tank Press " , Float(tpr),Cr
Debug "Run Press ", Float(rpr), Cr
Debug "Temperature ",Float(ttr), Cr
Debug Cr
ist= In (86)
Pause 2000
Loop

ADOFF
Out 48,0
Out 49,0
Pause 400
End Sub
```

REFERENCES

1. Polzin, K.A.: "Comprehensive Review of Planar Pulsed Inductive Plasma Thruster Research and Technology," *J. Propul. Power*, Vol. 27, No. 3, pp. 513–531, doi:10.2514/1.B34188, May–June 2011.

2. Dailey, C.L.; and Lovberg, R.H.: "The PIT MkV Pulsed Inductive Thruster," NASA CR-191155, Lewis Research Center, July 1993.

3. Dailey, C.L.; and Davis, H.A.: "Pulsed Plasma Propulsion Technology," Tech. Rep. AFRPL-TR-73-81, TRW Systems Group, Redondo Beach, CA, July 1973.

4. Polzin, K.A.: "Faraday Accelerator with Radio-Frequency Assisted Discharge (FARAD)," Ph.D. Thesis, Princeton University, Princeton, NJ, June 2006.

5. Choueiri, E.Y.; and Polzin, K.A.: "Faraday Acceleration with Radio-Frequency Assisted Discharge," *J. Propul. Power*, Vol. 22, No. 3, pp. 611–619, doi:10.2514/1.16399, May–June 2006.

6. Lovberg, R.H.; and Dailey, C.L.: "A PIT Primer," Tech. Rep. 005, RLD Associates, Lebanon, PA, 1994.

7. Polzin, K.A.:"Scaling and Systems Considerations in Pulsed Inductive Plasma Thrusters," *IEEE Trans. Plasma Sci.*, Vol. 36, No. 5, pp. 2189–2198, doi:10.1109/TPS.2008.2003537, November 2008.

8. Josephson, V.; and Hales, R.W.: "Parametric Study of the Conical Shock Tube," *Phys. Fluids*, Vol. 4, No. 3, pp. 373–379, doi:10.1063/1.1706336, 1961.

9. Fimognari, P.J.; Cassibry, J.T.; and Ims, K.-E.: "Effects of Pre-ionization and Bias Field on Plasmoid Formation and Acceleration," Paper Presented at 43rd AIAA/ASME/SAE/ASEE Joint Propulsion Conference, Cincinnati, OH, July 8–11, 2007.

10. Eskridge, R.H.; Fimognari, P.J.; Martin, A.K.; and Lee, M.H.: "Design and Construction of the PT-1 Prototype Plasmoid Thruster," *AIP Conf. Proc.*, Vol. 813, No. 1, pp. 474–483, doi:10.1063/1.2169225, January 2006.

11. Josephson, V.: "Production of High-Velocity Shocks," *J. Appl. Phys.*, Vol. 29, No. 1, pp. 30–32, doi:10.1063/1.1722937, January 1958.

12. Cruddace, R.C.; and Hill, M.: "Mechanism of Plasma Acceleration in a Conical Theta-pinch Gun," Tech. Rep. CLM-M52, Culham Laboratory, Oxfordshire, UK, 1966.

13. Niemala, C.S.; and Kirtley, D.E.: "Initial Results on an Annular Field Reversed Configuration Plasma Translation Experiment," Tech. Rep. AFRL-RZ-ED-TP-2008-489, Air Force Research Laboratory, Edwards Air Force Base, CA, November 2008.

14. Kirtley, D.E.; Gallimore, A.D.; Haas, J.; and Reilly, M.: "High Density Magnetized Toroid Formation and Translation with XOCOT: An Annular Field Reversed Configuration Plasma Concept," Tech. Rep. AFRL-PR-ED-TP-2007-387, Air Force Research Laboratory, Edwards Air Force Base, CA, August 2007.

15. Hallock, A.K.; and Polzin, K.A.: "Design of a Microwave Assisted Discharge Inductive Plasma Accelerator," Paper Presented at Space Propulsion 2010, San Sebastián, Spain, May 3–5, 2010.

16. Hallock, A.K.; Polzin, K.A.; Bonds, K.W.; and Emsellem, G.D.: "Effect of Inductive Coil Geometry and Current Sheet Trajectory of a Conical Theta Pinch Pulsed Inductive Plasma Accelerator," Paper Presented at 47th AIAA/ASME/SAE/ASEE Joint Propulsion Conference, San Diego, CA, July 31–August 3, 2011.

17. Browning, J.; Lee, C.; Plumlee, D.G.; et al.: "A Miniature Inductively Coupled Plasma Source for Ion Thrusters," *IEEE Trans. Plasma Sci.*, Vol. 39, No. 11, pp. 3187–3195, doi:10.1109/TPS.2011.2167634, November 2011.

18. Polzin, K.A.; Markusic, T.E.; Stanojev, B.J.; et al.: "Thrust Stand for Electric Propulsion Performance Evaluation," *Rev. Sci. Instrum.*, Vol. 77, No. 10, 105108., doi:10.1063/1.2357315, October 2006.

19. Wong, A.R.; Toftul, A.; Polzin, K.A.; and Pearson, J.B.: "Non-contact thrust stand calibration method for repetitively-pulsed electric thrusters," *Rev. Sci. Instrum.*, Vol. 83, No. 2, 025103, doi:10.1063/1.3680557, February 2012.

20. Hallock, A.K.; and Polzin, K.A.: "Computational Validation of a Two-dimensional Semi-Empirical Model for Inductive Coupling in a Conical Pulsed Inductive Plasma Thruster," Paper Presented at Joint Army-Navy-NASA-Air Force 8th MSS/6th LPS/5th SPS Meeting, Huntsville, AL, December 5–9, 2011.

21. Polzin K.A.; and Choueiri, E.Y.: "Performance Optimization Criteria for Pulsed Inductive Plasma Acceleration," *IEEE Trans. Plasma Sci.*, Vol. 34, No. 3, pp. 945–953, doi:10.1109/TPS.2006.875732, June 2006.

22. Polzin, K.A.; Adwar, J.E.; and Hallock, A.K.: "Optimization of Electrodynamic Energy Transfer in Coilguns with Multiple, Uncoupled Stages," *IEEE Trans. Magn.*, Vol. 49, No. 4, pp. 1453–1460, doi:10.1109/TMAG.2012.2230271, April 2013.

23. Jahn, R.G.: *Physics of Electric Propulsion*, McGraw-Hill Book Company, New York, NY, 1968.

24. Polzin, K.A.; Reneau, J.P.; and Sankaran, K.: "Incorporation of an Energy Equation into a Pulsed Inductive Thruster Performance Model," Paper Presented at 32nd International Electric Propulsion Conference, Wiesbaden, Germany, September 11–15, 2011.

25. "CCS Power Supply Operations & Maintenance Manual," General Atomics Electronic Systems, Manual #14187 - Revision H, April 2009.

26. Ennis, J.B.; Song, B.M.; Bushnell, A.H.; et al.: "Custom Design of Components and Power Supplies for Pulsed Power Systems," Engineering Bulletin Presented at IEEE Industrial Electronics Conference 2003, Roanoke, VA, November 2–6, 2003.

27. Dobrino et al., "NASA Interface Communications Specification," General Atomics Energy Products, Rev. X6, September 2, 2004.

28. Bushnell, A.H.: "Interfacing Pulsed Power Systems to Switching Power Supplies," Engineering Bulletin Presented at IEEE International Power Modulator Conference, Hollywood, CA, July 1–3, 2002.

29. Poylio, J.H.; Russell, D.; Goldstein, W.; et al.: "Pulsed Inductive Thruster: Flight-Scale Proof of Concept Demonstrator," 40th AIAA/ASME/SAE/ASEE Joint Propulsion Conference, Fort Lauderdale, FL, July 11–14, 2004.

30. Frisbee, R.H.: "Evaluation of High-Power Solar Electric Propulsion Using Advanced Ion, Hall, MPD, and PIT Thrusters for Lunar and Mars Cargo Missions," Paper Presented at 42nd AIAA/SAE/ASME/ASEE Joint Propulsion Conference, Sacramento, CA, July 9–12, 2006.

31 AMS 2681, Electron-Beam Welding, SAE International, Warrendale, PA, 2006.

32. Pressman, A.I.; Billings, K.; and Morey, T.: *Switching Power Supply Design*, 3rd ed., McGraw-Hill Professional, New York, NY, pp. 103–115, 2009.

REPORT DOCUMENTATION PAGE

Form Approved
OMB No. 0704-0188

1. REPORT DATE *(DD-MM-YYYY)*	2. REPORT TYPE	3. DATES COVERED *(From - To)*
01–08–2013	Technical Publication	

4. TITLE AND SUBTITLE

Summary of the 2012 Inductive Pulsed Plasma Thruster Development and Testing Program

5a. CONTRACT NUMBER

5b. GRANT NUMBER

5c. PROGRAM ELEMENT NUMBER

6. AUTHOR(S)

K.A. Polzin, A.K. Martin, R.H. Eskridge, A.C. Kimberlin, B.M. Addona, A.P. Devineni, N.R. Dugal-Whitehead, and A.K. Hallock*

5d. PROJECT NUMBER

5e. TASK NUMBER

5f. WORK UNIT NUMBER

7. PERFORMING ORGANIZATION NAME(S) AND ADDRESS(ES)

George C. Marshall Space Flight Center
Huntsville, AL 35812

8. PERFORMING ORGANIZATION REPORT NUMBER

M–1364

9. SPONSORING/MONITORING AGENCY NAME(S) AND ADDRESS(ES)

National Aeronautics and Space Administration
Washington, DC 20546–0001

10. SPONSORING/MONITOR'S ACRONYM(S)

NASA

11. SPONSORING/MONITORING REPORT NUMBER

NASA/TP—2013–217488

12. DISTRIBUTION/AVAILABILITY STATEMENT

Unclassified-Unlimited
Subject Category 20
Availability: NASA CASI (443–757–5802)

13. SUPPLEMENTARY NOTES

Prepared by the Propulsion Systems Department, Engineering Directorate
* Yetispace, Inc., Huntsville, Alabama

14. ABSTRACT

Inductive pulsed plasma thrusters are spacecraft propulsion devices in which energy is capacitively stored and then discharged through an inductive coil. While these devices have shown promise for operation at high efficiency on a range of propellants, many technical issues remain before they can be used in flight applications. A conical theta-pinch thruster geometry was fabricated and tested to investigate potential improvements in propellant utilization relative to more common, flat-plate planar coil designs. A capacitor charging system is used to permit repetitive discharging of thrusters at multiple cycles per second, with successful testing accomplished at a repetition-rate of 5 Hz at power levels of 0.9, 1.6, and 2.5 kW. The conical theta-pinch thruster geometry was tested at cone angles of 20°, 38°, and 60°, with single-pulse operation at 500 J/pulse and repetition-rate operation with the 38° model quantified through direct thrust measurement using a hanging pendulum thrust stand. A long-lifetime valve was designed and fabricated, and initial testing was performed to measure the valve response and quantify the leak rate at beginning-of-life. Subscale design and testing of a capacitor charging system required for operation on a spacecraft is reported, providing insights into the types of components needed in the circuit topology employed. On a spacecraft, this system would accept as input a lower voltage from the spacecraft DC bus and boost the output to the high voltage required to charge the capacitors of the thruster.

15. SUBJECT TERMS

electric propulsion, pulsed inductive thruster, inductive coupling, inductive plasma acceleration, pulsed gas injection, capacitor charging system

16. SECURITY CLASSIFICATION OF:			17. LIMITATION OF ABSTRACT	18. NUMBER OF PAGES	19a. NAME OF RESPONSIBLE PERSON
a. REPORT	b. ABSTRACT	c. THIS PAGE			STI Help Desk at email: help@sti.nasa.gov
U	U	U	UU	112	19b. TELEPHONE NUMBER *(Include area code)* STI Help Desk at: 443–757–5802

National Aeronautics and
Space Administration
IS20
George C. Marshall Space Flight Center
Huntsville, Alabama 35812